Theoretical Studies on Electronic Excited States of Transition Metal Complexes: Explanation and Understanding Based on Molecular Geometries and Electronic Structures

Ken Saito

2012

Preface

Electronic excited molecule is one of the most attractive research topics in modern chemistry because its chemical reactivity and physical property are much different from those of ground state molecule. In the previous researches, electronic structure calculations have played important roles. One of advantages of the electronic structure calculations is that they can present molecular geometries in the excited states, which are difficult to evaluate by experimental methods. Another advantage is that the calculations can explicitly show assignments of the excited states such as $n\pi^*$, $\pi\pi^*$, and charge transfer states, with quantitatively evaluating mixtures of them.

Though the electronic structure calculation is a powerful tool for the study of the excited molecules, its application must be careful, especially for the excited transition metal complexes. This is because electronic structure of the excited transition metal complex sometimes shows complicated nature such as multiconfiguration nature and near-degeneracy of excited states, which sometimes induces incorrect calculation result. Thus, studies with the electronic structure calculations have been fewer in the field of excited transition metal complexes compared to excited organic molecules. However, the computational studies for the excited states of the transition metal complexes should be actively performed since the electronic structure calculations can investigate fundamental properties of the excited state chemistry such as the molecular geometry and the electronic structure.

In this thesis, the author presents explanation and understanding about the nature and properties of the excited transition metal complexes by the electronic structure theories. This thesis consists of general introduction, chapters 1 to 5, and general conclusion. In chapters 1 and 2, multiple chemical bonds between two transition metals are investigated. Achievements of these chapters become fundamental knowledge of photochemical reactions of transition metal complexes; note that partial formation or dissociation of the metal–metal

multiple bonds often occur in these reactions. In chapter 3, phosphorescence energies of some platinum complexes are investigated. Shifts of the phosphorescence energies by experimental conditions such as solvent and temperature are discussed. In chapter 4, phosphorescence properties of other platinum complexes are studied. Discussion whether the phosphorescence occurs or not is performed based on the relationship between symmetry of electronic structure and spin–orbit interaction. In chapter 5, a new method is proposed to estimate oscillator strength of the Laporte-forbidden d–d absorption. Though this new method does not follow the Hertzberg–Teller approximation, which considers admixture of electronic states by molecular vibrations, it alternatively considers distortion of molecular orbitals. This new method clearly explains the degree of oscillator strength by molecular orbital pictures.

The author believes that achievements of this thesis will evolve the excited state chemistry of the transition metal complexes.

Ken Saito

2012

Acknowledgements

The studies in this thesis were carried out at Department of Molecular Engineering, Graduate School of Engineering, Kyoto University from 2004 to 2010. The author would like to express his gratitude to Professor Shigeyoshi Sakaki for his reliable discussion and helpful suggestions. His various comments based on physical and inorganic chemistries are invaluable for this thesis. The author greatly appreciates to Professor Hirofumi Sato for his considered advices and continuous encouragement. The author also express to his gratitude to Assistant Professor Yoshihide Nakao for his technical comments and scientific suggestions.

The author is also grateful to Professor Keisuke Umakoshi in Department of Applied Chemistry, Faculty of Engineering, Nagasaki University for his collaboration and careful discussion in chapter 4. The author also appreciates to Mr. Yoshinori Eishiro for his valuable suggestions and scientific comments in chapter 5. The author wishes to thank all the members of the research group of Prof. Shigeyoshi Sakaki.

The author thanks to financial support of Research Fellowship of Japan Society for Promotion of Science for Young Scientists.

Finally, the author sincerely thanks to his parents Masahiro Saito and Mutsumi Saito for their understanding, encouragement, and supports.

Ken Saito

2012

Contents

General Introduction

1. Theoretical Study of Electronic Excited Molecule

N. J. Turro, who is one of the most brilliant scientists in the field of photochemistry, said that "the excited molecule is really an *electronic isomer* of the corresponding ground state-molecule." in his book.[1] This means that the electronic excited molecule frequently shows interesting chemical reactivities and physical properties that are not observed in the ground state molecule. Examples of such chemical reactiviteis are photo-addition, photo-dissociation, and photo-isomerization reactions.[2] These photoreactions sometimes produce compounds that cannot be yielded by heat activated reaction. Thus, the photoreactions are attractive in the field of both fundamental and industrial chemistries. Examples of the physical properties are photo-emission[3] and photo–electric conversion.[4] These properties are also attractive to industrial chemists; molecules with these properties are applicable to frontier products such as light-emitting device[3c–e] and photovoltaic cell.[4]

In the history of excited state chemistry, theoretical study based on electronic structure calculation has played an important role. This is because such study provides fundamental properties of the excited state chemistry; one is molecular geometry and another is assignment of electronic structure. The former is difficult to evaluate by experimental methods because life-time of the excited state is generally short. The latter, of course, can be evaluated by experimental spectroscopic methods. An advantage of the calculation method is that it can estimate quantitative degree of state mixture in the excited state;[5] note that many excited states are formed by mixture of some electronic states such as $n\pi^*$, $\pi\pi^*$, and charge transfer (CT) states. In addition, the theoretical studies have presented creative and useful rules for nature and properties of the excited state molecules. One of well-known examples is the Woodward–Hoffman's rules.[6] These rules predict a product of the photo-isomerization reaction. Another example is the El-Sayed's rules.[7] These rules forecast the rate of intersystem crossing and the intensity of phosphorescence in organic molecules.

2. Theoretical Study of Electronic Excited Transition Metal Complex

Though the electronic structure calculation is a powerful tool to research the electronic excited molecules, its application must be careful, especially for transition metal complexes. A popular calculation method such as density functional theory (DFT)[8] sometimes provides incorrect result. Two reasons of this difficulty will be explained, as follows.

2.1. Multiconfiguration Nature

One reason is that the electronic structure of transition metal complex often shows multiconfiguration nature.[9] This means that the electronic structure is difficult to be represented by single electron configuration. For instance, in a molecule with C=C double bond, electronic structure of this C=C bond is represented by single electron configuration as $\sigma^2\pi^2\pi^{*0}\sigma^{*0}$, if this molecule does not have the multiconfiguration nature, where σ and π represent bonding molecular orbitals between two carbon atoms while σ^* and π^* represent antibonding counterparts. On the contrary, if this molecule has the multiconfiguration nature, the representation of the electronic structure needs excited electron configurations $\sigma^2\pi^0\pi^{*2}\sigma^{*0}$, $\sigma^0\pi^2\pi^{*0}\sigma^{*2}$, $\sigma^0\pi^0\pi^{*2}\sigma^{*2}$, etc, in addition to the $\sigma^2\pi^2\pi^{*0}\sigma^{*0}$. Because the σ and π orbitals do not have a node between two carbon atoms while the σ^* and π^* counterparts have it, considering these excited electron configurations makes electron density between two carbon atoms be thin and alternatively makes the density around each carbon atom be thick. Thus, the multiconfigurational representation is suitable for a weak C=C bond while the single-configurational one is appropriate for a strong C=C bond. When the π and π^* orbitals are respectively highest occupied and lowest unoccupied molecular orbitals (HOMO and LUMOs), the weak C=C bond corresponds to small HOMO–LUMO energy gap, whereas the strong C=C bond corresponds to large one. Thus, the multiconfiguration nature often appears when the HOMO–LUMO energy gap is small.

In an electronic structure calculation of a molecule with the multiconfiguration nature, singlereference methods such as DFT, Møller–Plesset perturbation theory (MP),[10] and coupled cluster (CC)[11,12] methods frequently give incorrect results. In order to perform correct calculation, we must use multireference methods such as multiconfigurational

perturbation theory based on the complete active space self-consistent-field wavefunction (CASSCF/CASPT2)[13] and multireference MP perturbation theory based on the CASSCF (CASSCF/MRMP).[14] Of course, the singlereference methods also take into account the excited electron configurations.[15] However, contribution of them is few percent in calculated wavefunctions. In the multireference methods, on the other hand, this contribution is much large.

In the transition metal complexes, d orbitals of metal atoms are localized near the metal centers. Thus, overlap of atomic orbitals between metal atom and another metal or typical atom is often small. This small overlap sometimes induces the small HOMO–LUMO energy gap. In this case, the transition metal complex presents the multiconfiguration nature.

One example of the transition metal complexes with the multiconfiguration nature is $[Re_2Cl_8]^{2-}$. This complex is famous for the first molecule with quadruple chemical bond, which is reported by F. A. Cotton et al in 1964.[16] This quadruple bond is formed by four bonding molecular orbitals between two rhenium nuclei; one σ, two π, and one δ orbitals, as shown in Figure 1. Since two d_{xy} orbitals hardly overlap each other, the energy gap between δ and δ* molecular orbitals is much small. In addition, these molecular orbitals are respectively the HOMO and LUMO. As a result, $[Re_2Cl_8]^{2-}$ has multiconfiguration nature, in other words, the electronic structure of this complex cannot be appropriately represented by one electron configuration as $\sigma^2\pi^4\delta^2\delta^{*0}\pi^{*0}\sigma^{*0}$. Other electron configurations such as $\sigma^2\pi^4\delta^0\delta^{*2}\pi^{*0}\sigma^{*0}$ must be needed. Because of this multiconfiguration nature, electronic structure calculation of $[Re_2Cl_8]^{2-}$ had been difficult. Actually, quantitative theoretical study had not been reported until recently, while qualitative studies had been published.[17] The first quantitative study was reported by L. Gagliardi and B. O. Roos in 2003.[18] They used the CASSCF/CASPT2 method. Their study presented schematic electron configuration of the Re–Re molecular orbitals as $\sigma^{1.92}\pi^{3.74}\delta^{1.54}\delta^{*0.46}\pi^{*0.26}\sigma^{*0.08}$ by summarizing mixture of the ground and excited electron configurations. This quantitative result means that the σ and π bonds are strong but the δ bond is weak.

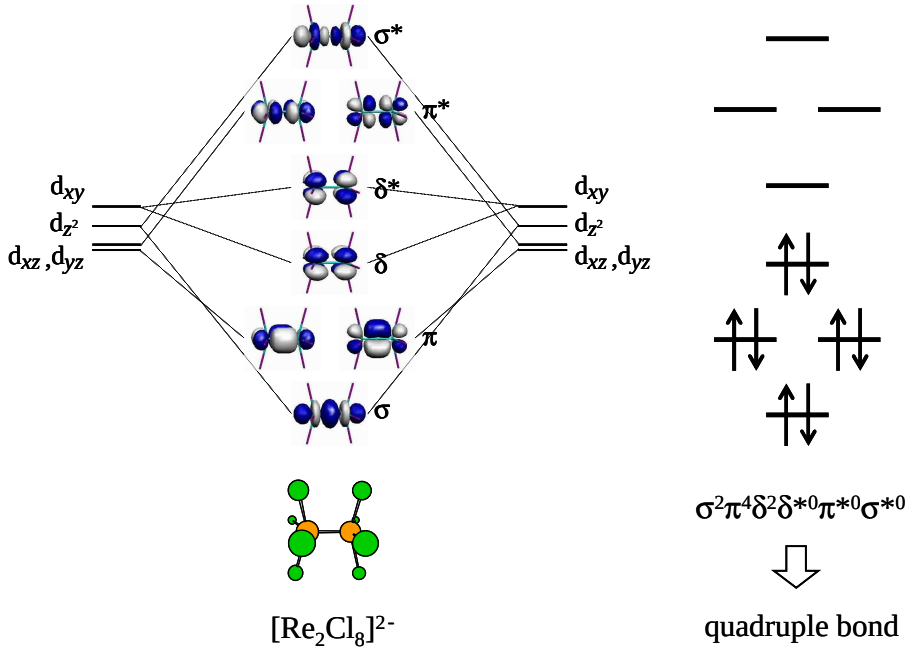

Figure 1. Molecular orbitals between two rhenium nuclei and schematic representation of Re–Re quadruple bond in $[Re_2Cl_8]^{2-}$.

2.2. Near-Degeneracy of Excited States

There are many kinds of electronic excited states in one transition metal complex; one is metal-centered excited state such as d–d state and another is ligand-centered excited state such as intra-ligand charge transfer (ILCT) and ligand centered ππ* states.[19] In addition, metal-to-ligand, ligand-to-mtal, and ligand-to-ligand charge transfer (MLCT, LMCT, and LLCT) excited states are also often observed.[19] Because of the wide variety of excited states, some of them frequently take similar energies one another, in other words, some excited states nearly degenerate to another state. In this case, solution of the electronic structure theory depends a great deal on initial condition and solution algorithm of the numerical calculation. As a result, the calculation sometimes provides an incorrect result; the solution of target excited state is not provided but that of another excited state is presented when the initial condition and solution algorithm are inappropriate for the target state.

Though the near-degeneracy nature is a difficulty of the electronic structure

calculation, this nature introduces an interesting property of the transition metal complexes. The near-degeneracy of the lowest and second-lowest excited states means that they easily alternate each other by environmental condition such as solvent. One example is excited states of $[Pt_2(\mu\text{-}H_2pz)_2(dfppy)_2]$ (H_2pz = pyrazolate and dfppy = 2-(2,4-difluorophenyl)pyridine) reported by M. E. Thompson et al.[20] The lowest energy triplet (T_1) excited state was experimentally assigned as mixture of ligand-centered $\pi\pi^*$ and MLCT states in polystyrene at room temperature (RT). However, the assignment of the T_1 state changes to metal–metal to ligand charge transfer (MMLCT) state when observed in 2-methyltetrahydrofulan (2-MeTHF) at RT. In addition, the phosphorescence energy is also changed by experimental condition; it is observed at 2.50 and 2.66 eV in the former condition but 1.93 eV in the latter one. Detailed discussion of these interesting phosphoresce properties will be presented in chapter 3 of this thesis.

3. Aims of This Thesis

Because of above mentioned difficulties, theoretical studies of the excited state chemistry have been fewer published in the field of transition metal complexes than in the field of organic molecules. Although many experimental studies have presented interesting nature and properties of the transition metal complexes so far, their fundamental explanations and understandings by the electronic structure theory are still very limited. Because the theoretical study can present the fundamental properties of the excited state chemistry such as the molecular geometry and the electronic structure, achievements of this study are very attractive for all chemists. Thus, the theoretical study should be actively subjected for the future. In this thesis, the author wishes to perform theoretical studies on electronic excited states of transition metal complexes, overcoming above mentioned difficulties.

In chapter 1, multiple chemical bonds between two transition metals are studied. The knowledge of multiple bond is important and necessary in discussion of the photochemical reactions since partial formation or dissociation frequently occurs in these reactions.[2] However, knowledge of metal–metal multiple bond is hard to study because the transition

metal complexes with the metal–metal multiple bond often show the multiconfiguration nature; note that one example is above mentioned Re–Re quadruple bond in $[Re_2Cl_8]^{2-}$. In this chapter, the author uses the multireference methods, the CASSCF/MRMP method and multiconfigurational quasi-degenerate perturbation theory based on state-averaged CASSCF wavefunction (SA-CASSCF/MCQDPT),[21] to appropriately investigate the metal–metal multiple bonds. Four rhenium dinuclear complexes, $[Re_2Cl_8]^{2-}$, $[Re_2(\mu\text{-}Cl)_3Cl_6]^{2-}$, $[Re_2(\mu\text{-}Cl)_3Cl_6]^{-}$, and $[Re_2(\mu\text{-}Cl)_2Cl_8]^{2-}$ are investigated, where each complex take different molecular geometry, as shown in Figrue 2; $[Re_2Cl_8]^{2-}$ takes non-bridged geometry,[16] $[Re_2(\mu\text{-}Cl)_3Cl_6]^{2-}$ and $[Re_2(\mu\text{-}Cl)_3Cl_6]^{-}$ take face-sharing bioctahedral bridged one,[22–24] and $[Re_2(\mu\text{-}Cl)_2Cl_8]^{2-}$ takes edged-sharing one.[25] Although the $[Re_2Cl_8]^{2-}$ was studied in the previous work,[18] as mentioned above, the other complexes have not been theoretically investigated by the multireference methods. Purpose of this chapter is to clarify electronic structures and strengths of bonding interactions of the Re–Re multiple bonds. Also, comparisons of these properties among the four rhenium complexes are presented.

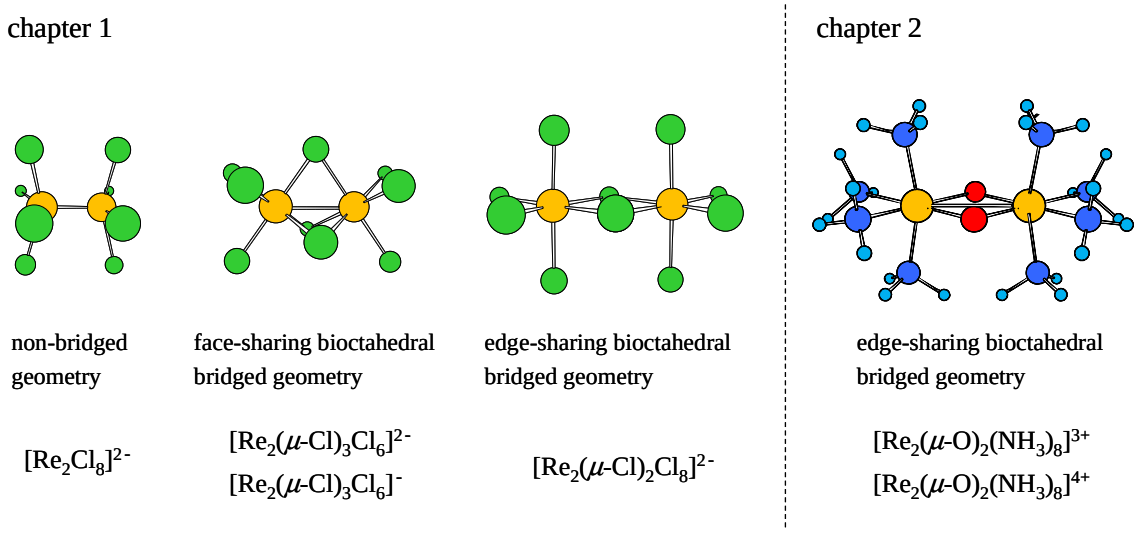

Figure 2. Molecular geometries of $[Re_2Cl_8]^{2-}$, $[Re_2(\mu\text{-}Cl)_3Cl_6]^{2-}$, $[Re_2(\mu\text{-}Cl)_3Cl_6]^{-}$, $[Re_2(\mu\text{-}Cl)_2Cl_8]^{2-}$, $[Re_2(\mu\text{-}O)_2(NH_3)_6]^{3+}$, and $[Re_2(\mu\text{-}O)_2(NH_3)_6]^{4+}$. The former four and the latter two complexes are respectively studied in chapters 1 and 2.

In chapter 2, multiple bonds in two rhenium dinuclear complexes, $[Re_2(\mu\text{-}O)_2(NH_3)_8]^{3+}$ (Re(III)–Re(IV) complex) and $[Re_2(\mu\text{-}O)_2(NH_3)_8]^{4+}$ (Re(IV)–Re(IV) complex), are investigated, where these complexes are model of $[Re_2(\mu\text{-}O)_2(Metpa)_2]^{3+}$, $[Re_2(\mu\text{-}O)_2(Metpa)_2]^{4+}$, and $[Re_2(\mu\text{-}O)_2(Me_2tpa)_2]^{4+}$ {Metpa = ((6-methyl-2-pyridyl)-methyl) bis(2-pyridylmethyl)amine and Me_2tpa = bis((6-methyl-2-pyridyl)methyl)(2-pyridylmethyl) amine}.[26] Both investigated complexes take the edge-sharing bioctahedral bridged geometry, as shown in Figure 2, like $[Re_2(\mu\text{-}Cl)_2Cl_8]^{2-}$ (Re(IV)–Re(IV) complex) in the previous chapter. Molecular orbitals between two rhenium nuclei are complicated in this chapter, as follows: In the previous chapter, the σ, π, and δ bonding Re–Re orbitals and their antibonding counterparts mostly consist of atomic orbitals of rhenium nuclei but hardly include those of chlorine ligands. However, in this chapter, the σ, π, δ, and σ* orbitals are formed by atomic orbitals of both rhenium nuclei and oxygen ligands, while the π* and δ* orbitals mostly consist of those of only rhenium atoms. Because of these complicated Re–Re molecular orbitals, the multiple bonds in $[Re_2(\mu\text{-}O)_2(NH_3)_8]^{3+}$ and $[Re_2(\mu\text{-}O)_2(NH_3)_8]^{4+}$ are untypical. Purpose of this chapter is to elucidate electronic structures and strengths of bonding interactions of such complicated Re–Re multiple bonds by the multireference theoretical methods. Also, assignments of absorption spectra of these complexes are presented.

In chapter 3, phosphorescence properties of four dinuclear platinum complexes, $[Pt_2(\mu\text{-}R_2pz)_2(dfppy)_2]$ {dfppy = 2-(2,4-difluorophenyl)pyridine; R_2pz = pyrazolate (H_2pz), 3,5-dimethylpyrazolate (Me_2pz), 3-methyl-5-*tert*-butylpyrazolate (Me^tBupz), and 3,5-bis(*tert*-butyl)pyrazolate ($^tBu_2pz$)} (Table 1), are researched. Their phosphorescence energies are much affected by experimental conditions such as solvent and temperature, as shown in Table 1,[20] note that the phosphorescence energies of the μ-H_2pz complex have already been mentioned above. Not only the μ-H_2pz complex but also the other three complexes emit lower-energy phosphorescence in 2-MeTHF at RT than in 2-MeTHF at 77 K and polystyrene at RT; for example, the phosphorescence energies of the μ-Me^tBupz complex are 1.95eV in the former condition but 2.49 and 2.27 eV in the latter two conditions. In addition, these differences of phosphorescence energies are large in the μ-H_2pz and

μ-Me_2pz complexes but small in the μ-MetBu and μ-$^t Bu_2$ complexes. Purpose of this chapter is to reveal mechanism of these interesting phosphorescence properties, based on electronic structure and molecular geometry in the excited state. The former factor was experimentally assigned in the previous work[20] but the latter was not investigated.

Table 1. Phosphorescence energies (in eV) of four platinum dinuclear complexes reported in ref 20.

complex		2-MeTHF at 77 K	polystylene at RT	2-MeTHF at RT
μ-H_2pz	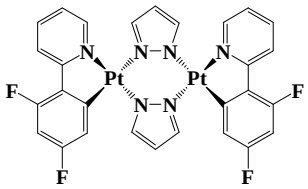	2.71, 2.52	2.66, 2.50	1.93
μ-Me_2pz	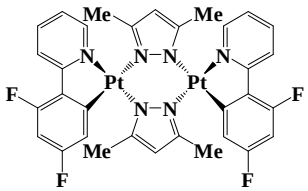	2.68, 2.49	2.63, 2.46	1.98
μ-Me^{t}Bupz	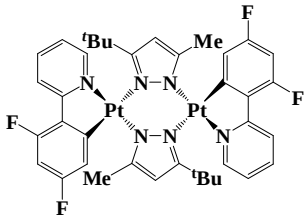	2.49	2.27	1.95
μ-$^t Bu_2pz$	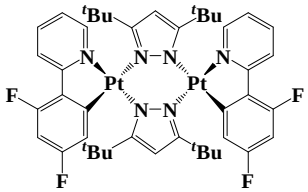	2.18	1.96	1.80

In chapter 4, intersystem crossing from singlet to triplet excited states is studied. This is one of the determinant factors whether the phosphorescence strongly occurs or not since the phosphorescence occurs after the intersystem crossing. This intersystem crossing is induced by spin−orbit interaction between the singlet and triplet excited states, thus, discussion of the spin−orbit interaction is indispensable for understanding and predicting the phosphorescence intensity.

The discussion of the spin−orbit interaction had been actively performed for the organic molecules by M. A. El-Sayed.[7] He estimated strength of the spin−orbit interaction by matrix element $<^1\Psi|H_{so}|^3\Psi>$, where the $^1\Psi$ and $^3\Psi$ are wavefunctions of the singlet and triplet excited states and the H_{so} is spin−orbit Hamiltonian. It is noted that the $^1\Psi$ and $^3\Psi$ have unique symmetries; for example, in pyrazine molecule, the wavefunction of $n\pi^*$ excited state possesses B_{3u} symmetry while that of $\pi\pi^*$ one possesses B_{1u}.[7a] In addition, the H_{so} also has symmetry since this Hamiltonian includes angular momentum operator $\boldsymbol{l}$.[7c] Thus, degree of the spin−orbit matrix element $<^1\Psi|H_{so}|^3\Psi>$ can be estimated by symmetries of the $^1\Psi$ and $^3\Psi$, in other words, strength of the spin−orbit interaction is determined by symmetries of the singlet and triplet excited states. El-Syaed had deeply studied these matrix elements for many kinds of excited states of organic molecules. He had presented a lot of useful conclusions; for instance, in nitrogen heterocyclic molecule, the spin−orbit interaction between $^1n\pi^*$ and $^3\pi\pi^*$ states is larger than that between $^1n\pi^*$ and $^3n\pi^*$ states, where the superscript 1 and 3 respectively mean singlet and triplet excited states. Nowadays, his conclusions are called as the El-Sayed's rules.

The discussions by El-Sayed can also apply to the spin−orbit interaction and the intersystem crossing of the transition metal complex. Thus, purpose of chapter 4 is to discuss whether the phosphorescence occurs or not in some transition metal complexes, based on symmetries of their excited states. In particular, phosphorescence properties of two platinum dinuclear complexes, $[Pt_2(\mu\text{-pz})_2(bpym)_2]^{2+}$ and $[Pt_2(\mu\text{-pyt})_2(ppy)_2]$ (Figure 3), are researched. The former complex emits phosphorescence in solid state at RT but does not in 2-MeTHF at RT[27] while the latter one does in both conditions.[28] This difference is discussed in this chapter.

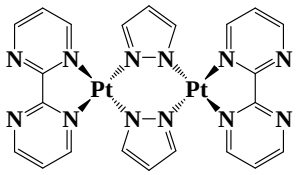

Phosphorescence at RT is observed in solid state but not observed in 2-MeTHF.

$[Pt_2(\mu\text{-pz})_2(bpym)_2]^{2+}$

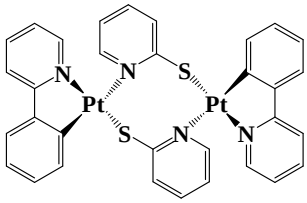

Phosphorescence at RT is observed in both solid state and 2-MeTHF.

$[Pt_2(\mu\text{-pyt})_2(ppy)_2]$

Figure 3. Geometries and phosphorescence properties of $[Pt_2(\mu\text{-pz})_2(bpym)_2]^{2+}$ (ref 27) and $[Pt_2(\mu\text{-pyt})_2(ppy)_2]$ (ref 28).

In chapter 5, Laporte-forbidden d–d absorptions of transition metal complexes bearing octahedral geometries are studied. In the octahedral complex, five d orbitals of metal center are split into three t_{2g} and two e_g orbitals,[29] as shown in Figure 4. One electron excitation from the t_{2g} to the e_g orbitals is assigned as the d–d absorption. This excitation corresponds to $^1A_{1g} \rightarrow {}^1T_{1g}$ and $^1A_{1g} \rightarrow {}^1T_{2g}$ absorptions. Because the $^1A_{1g}$, $^1T_{1g}$, and $^1T_{1g}$ states possess gerade symmetry but the dipole moment operator $\boldsymbol{er}$ possesses ungerade one, transition dipole moments $\langle\Psi(^1A_{1g})|\boldsymbol{er}|\Psi(^1T_{1g})\rangle$ and $\langle\Psi(^1A_{1g})|\boldsymbol{er}|\Psi(^1T_{2g})\rangle$ are completely zero, where the $\Psi(^1A_{1g})$, $\Psi(^1T_{1g})$, and $\Psi(^1T_{2g})$ represent wavefunctions of these states. As a result, both $^1A_{1g} \rightarrow {}^1T_{1g}$ and $^1A_{1g} \rightarrow {}^1T_{2g}$ absorptions are assumed as inactive under the transition dipole approximation.[29] However, in a real complex, both absorptions are observed though intensities of them are small. This is because symmetries of the $^1A_{1g}$, $^1T_{1g}$, and $^1T_{2g}$ states are broken by molecular vibrations, in other words, these states have no longer the gerade symmetries.[29]

In modern theoretical chemistry, time-dependent (TD) DFT[30] is one of the most useful methods to evaluate absorption spectrum. Actually, this method can quantitatively estimate the transition energies of the d–d absorption in many systems.[31] However, the oscillator strength of the d–d absorption cannot be evaluated. This is because the TD-DFT method calculates the oscillator strength by the transition dipole approximation.

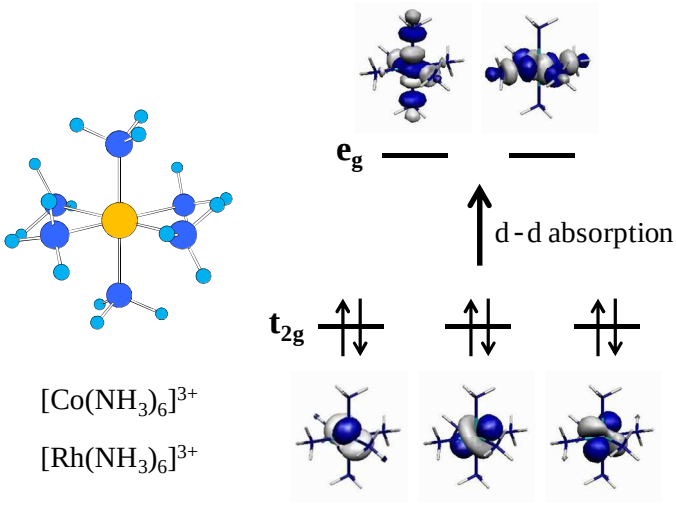

Figure 4. Schematic representation of d–d absorptions of $[Co(NH_3)_6]^{3+}$ and $[Rh(NH_3)_6]^{3+}$.

One method to estimate the oscillator strength is related to the Hertzberg–Teller approximation.[32] This approximation considers mixtures of electronic excited states by molecular vibrations. For instance, this approximation considers that the $^1T_{1g}$ state mixes with other excited states bearing ungerade symmetries such as the $^1A_{1u}$, $^1T_{1u}$, and $^1T_{2u}$ states, though degree of this mixing is small. As a result, this mixed $^1T_{1g}$ state has also ungerade symmery, which enables the $^1A_{1g} \rightarrow {}^1T_{1g}$ absorption.

Although the Hertzberg–Teller approximation is useful and popular method to evaluate the oscillator strength of the Laporte-forbidden d–d absorption, this approximation might not be suitable for an intuitive understanding. Since molecular orbital picture gives an intuitive understanding in all fields of chemistry, another method based on this picture would be suitable for the understanding of the d–d absorption. Thus, the author proposes a new method based on molecular orbital picture to evaluate the oscillator strength of the d–d absorption.

Purposes of chapter 5 are to propose a new calculation method and to present understandings of the d–d absorptions base on molecular orbital pictures. This new method does not consider mixture of the excited states but alternatively considers distortion of the t_{2g}

and e_g orbitals by molecular vibrations. Because the distorted e_g and t_{2g} ortbitals are no longer the gerade symmetry, the $t_{2g} \rightarrow e_g$ excitation is no longer the Laporte-forbidden. Thus, the oscillator strength can be evaluated by the transition dipole approximation within the TD-DFT method. This new method applies to the $^1A_{1g} \rightarrow {}^1T_{1g}$ and $^1A_{1g} \rightarrow {}^1T_{2g}$ absorptions of $[Co(NH_3)_6]^{3+}$ and $[Rh(NH_3)_6]^{3+}$ (Figure 4)[33,34]. Discussion about their oscillator strengths is performed based on the molecular orbital picture of t_{2g} and e_g ortbitals.

Through studies of chapters 1 to 5, the author presents explanation and understanding about the nature and properties of the excited transition metal complexes. The author believes that achievements of all chapters will evolve the excited state chemistry of the transition metal complexes.

References

(1) Turro, N. J. *Chapter 1. OrganicPhotochemisry–An Overview* In *Modern Molecular Photochemistry*; University Science Books, 1991.

(2) (a)Svoboda, J.; Köing, B. *Chem. Rev.* **2006**, *106*, 5413. (b) Hoffmann, N. *Chem. Rev.* **2008**, *108*, 1052.

(3) (a) Valeur, B. *Molecular Fluorescence: Principle and Applications*; Wiley, 2001. (b) McGlynn, S. P.; Azumi, T.; Kinoshita, M. *Molecular Spectroscopy of The Triplet State*; Prentice-Hall, Inc., 1969. (c) Baldo, M. A.; O'Brien, D. F.; You, Y.; Shoustikov, A.; Sibley, S.; Thompson, M. E.; Forrest, S. R. *Nature*, **1998**, *395*, 151. (d) Baldo, M. A.; Lamansky, S.; Burrows, P. E.; Thompson, M. E.; Forrest, S. R. *Appl. Phys. Lett.* **1999**, *75*, 4. (e) Yersin, H., Eds. *Highly Efficient OLEDs with Phosphorescent Materials*; Wiley, 2007.

(4) (a) Lique, A.; Hegedus, S. Eds. *Status, Trends, Challenges and the Bright Future of Solar Electricity from Photovoltaics* In *Handbook of Photovoltaic Science and Engineering*; Wiley, 2003. (b) Nojik, A. J.; Miller, J. Eds. *Solar Photon Conversion (Special Issue)* In *Chem. Rev.* **2010**, *110*, 6443–6936. (Issue 11).

(5) (a) Hay, P. J. *J. Phys. Chem. A* **2002**, *106*, 1634. (b) Liu, T.; Xia, B.-H.; Zhou, X.; Zhang, H.-X.; Pan, Q.-J.; Gao, J.-S. *Organometallics*, **2007**, *26*, 143.

(6) (a)Woodward, R. B.; Hoffman, R. *J. Am. Chem. Soc.*, **1965**, *87*, 395. (b) Woodward, R. B.; Hoffman, R. *J. Am. Chem. Soc.*, **1965**, *87*, 2056. (c)Woodward, R. B.; Hoffman, R. *J. Am. Chem. Soc.*, **1965**, *87*, 2511.

(7) (a) El-Sayed, M. A. *J. Chem. Phys.* **1962**, *36*, 573. (b) El-Sayed, M. A. *J. Chem. Phys.* **1963**, *38*, 2834. (c) El-Sayed, M. A. *J. Chem. Phys.* **1964**, *41*, 2462.

(8) (a) Hohenberg, P.; Kohn, W. *Phys. Rev. B* **1964**, *136*, 864. (b) Kohn, W.; Sham, J. *Phys. Rev. A* **1965**, *140*, 1133. (c) Parr, R. G.; Yang, W. *Density Functional Theory*; Oxford University Press, 1989. (d) Koch, W.; Holthausen, M. C. *A Chemist's Guide to Density Functional Thoery*; Wiley, 2000.

(9) Roos, B. O. *Ab Initio Methods in Quantum Chemistry-II* In *Advances in Chemical Physics*; Wiley, 1987.

(10) Møller, C.; Plesset, M. S. *Phys. Rev.* **1934**, *46*, 618.

(11) (a) Coester, F.; Kümmel, H. *Nucl. Phys.* **1960**, *17*, 477.

(12) (a) Čížek, J. *J. Chem. Phys.* **1966**, *45*, 4256. (b) Čížek, J. *Adv. Chem. Phys.* **1969**, *14*, 35.

(13) (a) Andesrson, K.; Malmqvist, P.-Å, Roos, B. O.; Sadlej, A. J.; Wolinski, K. *J. Phys. Chem.* **1990**, *54*, 5483. (b) Andersson, K.; Malmqvist, P.-Å, Roos, B. O. *J. Chem. Phys.* **1992**, *96*, 1218. (c) Roos, B. O.; Andersson, K.; Fülscher, M. P.; malmqvist, P.-Å.; S.-Andrés, L.; Perloot, K.; Merchán, M. In *Advances in Chemical Physics: New Methods in Computational Chemistry Quanttum Mechanistics, Vol. XCIII*; Prigogine, I.; Rices, S. A., Eds.; Wiley, 1996.

(14) (a) Hirao, K. *Chem. Phys. Lett.* **1992**, *190*, 374. (b) Hirao, K. *Chem. Phys. Lett.* **1992**, *196*, 397. (c) Hirao, K. *Int. J. Quantum. Chem.* **1992**, *S26*, 517.

(15) Jensen, F. *Chapter 4. Electron Correlation Methods* In *Introduction to Computational Chemistry. 2nd Edition*; Wiley, 2007.

(16) (a) Cotton, F. A.; Curtis, N. F.; Harris, C. B.; Johnson, B. F. G.; Lippard, S. J.; Mague, J. T.; Robinson, W. R.; Wood, J. S. *Science* **1964**, *145*, 1306. (b) Cotton, F. A.; Harris, C. B. *Inorg. Chem.* **1965**, *4*, 330. (c)Cotton, F. A. *Inorg. Chem.* **1965**, *4*, 334.

(17) (a)Bursten, B. E.; Cotton, F. A.; Fanwick, P. E.; Stanley, G. G.; Walton, R. A. *J. Am. Chem. Soc.* **1983**, *105*, 2606. (b) Hay, P. J. *J. Am. Chem. Soc.* **1982**, *104*, 7007. (c) Blaudeau, J.-P.; Ross, R. B.; Pitzer, R. M. *J. Phys. Chem.* **1994**, *98*, 7123.

(18) Gagliardi, L.; Roos, B. O. *Inorg. Chem.* **2003**, *42*, 1599.

(19) Crosby, G. A. *Acc. Chem. Res.* **1975**, *8*, 231.

(20) Ma, B.; Li, J.; Djurovich, P. I.; Yousufuddin, M.; Bau, R.; Thompson, M. E. *J. Am. Chem. Soc.* **2005**, *127*, 28.

(21) (a) Nakano, H. *J. Chem. Phys.* **1993**, *99*, 7983. (b) Nakano, H. *Chem. Phys. Lett.* **1993**, *207*, 372.

(22) Heath, G. A.; McGrady, J. E.; Raptis, R. G.; Willis, A. C. *Inorg. Chem.* **1996**, *35*, 6838.

(23) Hauck, H. G.; Klingelhöfer, P.; Müller, U.; Dehnicke, K. *Z. Anorg. Allg. Chem.* **1984**, *510*, 180.

(24) Baranov, A. I.; Khvorykh, G. V.; Troyanov, S. I. *Z. Anorg. Allg. Chem.* **1999**, *625*, 1240.

(25) Beck, J.; K.-Buschbaum, M.; Wolf, F. *Z. Anorg. Allg. Chem.* **1999**, *625*, 975.

(26) Sugimoto, H.; Kamei, M.; Umakoshi, K.; Sasaki, Y.; Suzuki, M.; *Inorg. Chem.* **1996**, *35*, 7082.

(27) Umakoshi, K.; Kimura, K.; Kim, Y. H.; Arikawa, Y.; Ohnishi, M.; Ishizaka, S.; Kitamura, N. *Bull. Chem. Soc. Jpn.*, **2010**, *83*, 1054.

(28) Koshiyama, T.; Omura, A.; Kato, M. *Chem. Lett.* **2004**, *33*, 1386.

(29) (a) Figgs, B. N.; Hitchman, M. A. *Ligand-Field Theory and its Applications*; Wiley, 2000. (b) Sugano, S.; Tanabe, Y.; Kamimura, H. *Multiplets of Transitionmetal Ions in Crystals*; Academic Press Inc., 1970.

(30) Bauernschmitt, R.; Ahlrichs, R. *Chem. Phys. Lett.* **1996**, *256*, 454.

(31) Grimm, S. *Rev. Comput. Chem.* **2004**, *20*, 153.

(32) Hertzberg, G.; Teller, E. *Z. Phys. Chem., Abt. B* **1933**, *21*, 410.

(33) Kofod, P. *Inorg. Chem.* **1995**, *34*, 2768.

(34) Peterson, J. D.; Ford, P. C. *J. Phys. Chem.* **1974**, *78*, 1144.

Chapter 1

Theoretical Study of Rhenium Dinuclear Complexes: Re–Re Bonding Nature and Electronic Structure

1.1. Introduction

$[Re_2Cl_8]^{2-}$ (d^4–d^4) (**1**; see Scheme 1) is one of the most interesting dinuclear transition metal complexes, because this complex possesses a unique Re–Re quadruple bond in a formal sense, as reported by Cotton and his collaborators.[1] In this complex, the $d_{x^2-y^2}$ orbital of each Re center interacts with Cl ligands and the other four d orbitals participate in the Re–Re bonding and antibonding molecular orbitals, as follows: Two d_{z^2} orbitals interact with each other to form $\sigma(a_{1g})$ and $\sigma^*(a_{2u})$ molecular orbitals, as shown in Scheme 2. The d_{xz} and d_{yz} orbitals of one Re center interact with those of the other Re center to form $\pi(e_u)$ and $\pi^*(e_g)$ molecular orbitals. The dxy orbital of one Re center interacts with that of the other Re center to form $\delta(b_{2g})$ and $\delta^*(b_{1u})$ molecular orbitals. The quadruple Re–Re bond arises from the $\sigma^2\pi^4\delta^2$ electron configuration.[1] The eclipsed structure with D_{4h} symmetry of this complex is one of the evidences of the presence of the δ bonding interaction; if this bonding interaction was absent, the eclipsed structure became less stable

Scheme 1.

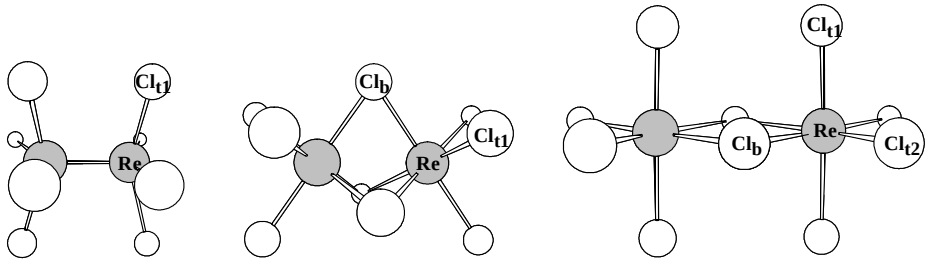

$[Re_2Cl_8]^{2-}$ (**1**)

$[Re_2(\mu\text{-}Cl)_3Cl_6]^{2-}$ (**2a**)

$[Re_2(\mu\text{-}Cl)_3Cl_6]^{-}$ (**2b**)

$[Re_2(\mu\text{-}Cl)_2Cl_8]^{2-}$ (**3**)

than the staggered one because of the larger static repulsion between Cl ligands.[1] Similar complexes such as $[Mo_2Cl_8]^{4-}$, $[Tc_2Cl_8]^{2-}$, and $[Tc_2Cl_8]^{3-}$ have been reported so far.[2–4] Their metal–metal bonding nature is discussed in the same way.

Several rhenium dinuclear complexes taking different structures from that of **1** have been reported so far. Some of them are $[Re_2(\mu\text{-}Cl)_3Cl_6]^{2-}$ (d^3–d^4) (**2a**) and $[Re_2(\mu\text{-}Cl)_3Cl_6]^{-}$ (d^3–d^3) (**2b**), which take a face-sharing bioctahedral structure with D_{3h} symmetry,[5–7] as shown in Scheme 1. In these complexes, five d orbitals of each Re center split into e_g- and t_{2g}-like orbitals. The former orbitals are unoccupied in a formal sense because they are at much higher energy than the latter orbitals by the antibonding interaction with Cl ligands. The latter orbitals form $\sigma(a_1')$, $\delta(e')$, $\delta^*(e'')$, and $\sigma^*(a_2'')$ molecular orbitals between two Re centers, as shown in Scheme 3. This means that these complexes contain a Re–Re multiple bond in a formal sense. Similar complexes such as $[Ti_2(\mu\text{-}Cl)_3Cl_6]^{-}$, $[Cr_2(\mu\text{-}Cl)_3Cl_6]^{3-}$, $[Mo_2(\mu\text{-}Cl)_3Cl_6]^{3-}$, and $[W_2(\mu\text{-}Cl)_3Cl_6]^{3-}$ have been reported, too.[8–11] Another example is $[Re_2(\mu\text{-}Cl)_2Cl_8]^{2-}$ (d^3–d^3) (**3**), which takes an edge-sharing bioctahedral structure with D_{2h} symmetry, as shown in Scheme 1.[12] Like **2a** and **2b**, five d orbitals of each Re center split into e_g- and t_{2g}-like orbitals. The former orbitals are unoccupied like those in **2a** and **2b**. The latter orbitals form $\sigma(a_g)$, $\pi(b_{2u})$, $\delta(b_{1g})$, $\delta^*(a_u)$, $\pi^*(b_{3g})$, and $\sigma^*(b_{1u})$ molecular orbitals between two Re centers, as shown in Scheme 4. $[Ti_2(\mu\text{-}Cl)_2Cl_8]^{2-}$, $[Mo_2(\mu\text{-}Cl)_2Cl_8]^{2-}$, and $[Re_2(\mu\text{-}Cl)_2Cl_8]$ also take a similar edge-sharing bioctahedral structure.[8,13,14]

Many theoretical studies of **1** have been carried out to clarify its interesting electronic structure and its Re–Re bonding nature.[15–18] However, the $^1A_{1g} \rightarrow {}^1A_{2u}$ ($\delta \rightarrow \delta^*$) excitation energy was not correctly calculated previously; for instance, the self-consistent-field Xα scattered-wave (SCF-Xα-SW) method presented a much smaller excitation energy (0.87 eV)[15] than the experimental value (1.82 eV).[19] On the other hand, the general valence bond method with the configuration interaction (GVB-CI) and the complete active space self-consistent-field (CASSCF) method presented large excitation energies, 3.2016 and

3.384 eV,[17] respectively. Recently, its excitation energy was correctly evaluated to be 1.97 eV by the second-order perturbation theory based on the CASSCF reference state (CASPT2).[18] This result suggests that incorporation of dynamical electron correlation based on the multireference wavefunction is indispensable to investigate this complex.

Various kinds of face- and edge-sharing dinuclear metal complexes including **2a**, **2b**, and **3** were also theoretically investigated with the broken-symmetry density functional theory (BS-DFT) by Stranger and his collaborators,[20] in which metal–metal bonding nature was discussed. However, the relative energies of several important electronic states have not been studied yet, although they deeply relate to the metal-metal bonding nature. It is worthwhile to evaluate the relative energies of the ground and several low-energy excited states of these dinuclear rhenium complexes and to shed clear light on the Re–Re bonding nature.

Scheme 2.

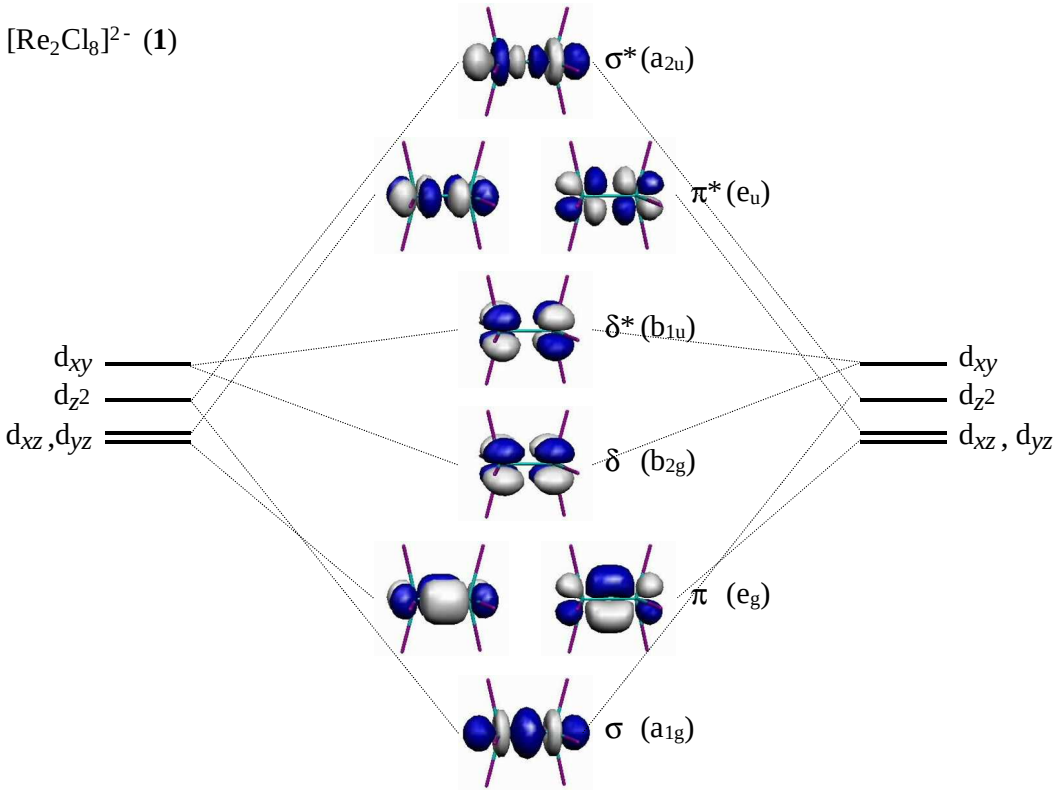

Scheme 3. Re–Re bonding and antibonding orbitals of $[Re_2(\mu\text{-}Cl)_3Cl_6]^{2-}$ (**2a**) and $[Re_2(\mu\text{-}Cl)_3Cl_6]^{-}$ (**2b**).

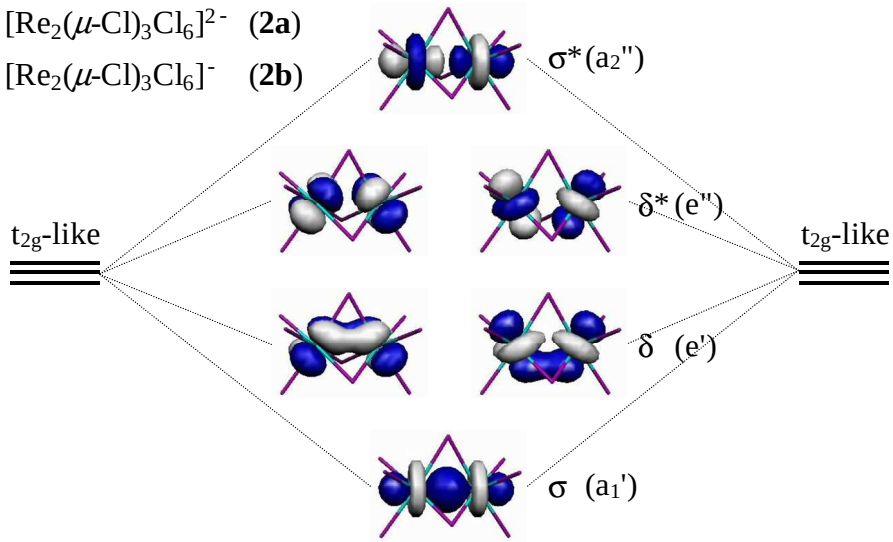

Scheme 4. Re–Re bonding and antibonding orbitals of $[Re_2(\mu\text{-}Cl)_2Cl_8]^{2-}$ (**3**).

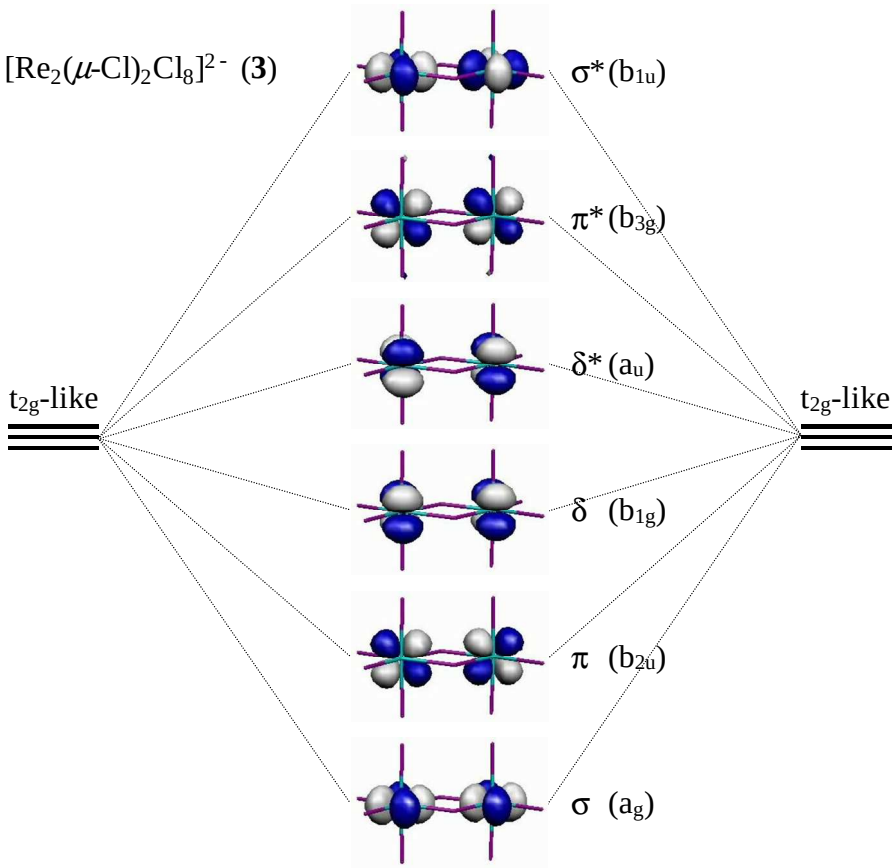

In this work, we theoretically investigated **1**, **2a**, **2b**, and **3** with the multireference second-order Møller–Plesset perturbation theory (MRMP2)[21] and the multiconfigurational quasidegenerate second-order perturbation theory (MCQDPT).[22] Our purposes here are to show clearly what is the ground state, to evaluate relative energies of several important low-energy excited states and to clarify electronic structures and Re–Re bonding nature of these complexes. The DFT(B3LYP),[23,24] coupled cluster singles and doubles with perturbative triples (CCSD(T)), BS-DFT(B3LYP), and BS-CCSD(T) methods were also applied to **1** and **2b** to examine reliabilities of these methods for theoretical investigation of these dinuclear rhenium complexes.

1.2. Computational Details

Geometries of these complexes were taken from X-ray analyses (see Table A1 in Appendix).[1,5,12] Only in **1** was geometry optimization performed with the CASSCF and MRMP2 methods, where the Re–Re and Re–Cl_{t1} bond distances and the Re–Re–Cl_{t1} bond angle were optimized under D_{4h} symmetry. Potential energy curve (PEC) of **1** was evaluated with the MRMP2 method, where the only Re–Re bond distance was changed but the Re–Cl_{t1} bond distance and Re–Re–Cl_{t1} bond angle were fixed to the corresponding experimental values, respectively.

We employed two basis set systems (basis-I and II) in this study. In basis-I, core electrons of Re were replaced with the small relativistic effective core potentials (ECPs) reported by Hay and Wadt[25] and valence electrons were represented by (541/541/111/1) basis set.[25–27] The cc-pVDZ basis set was used for Cl.[28] In basis-II, valence electrons of Re were represented by (4311/4311/111/1) basis set,[25–27] whereas the same ECPs as those of basis-I were used to replace core electrons. For Cl, the aug-cc-pVDZ basis set[28] was used.

The CASSCF and MRMP2 methods were applied to **1**, **2b**, and **3** to investigate their nondegenerate electronic states, and the state-averaged CASSCF (SA-CASSCF) and

MCQDPT methods were applied to **2a** to investigate its degenerate electronic states. In the CASSCF calculation of **1**, one σ, two π, and one δ molecular orbitals and their antibonding counterparts were taken as the active space (see Scheme 2), in which eight electrons were involved. Molecular orbitals that consist mainly of the $d_{x^2-y^2}$ orbital were excluded from the active space because they are at much different energies from the active orbitals. In the SA-CASSCF calculation of **2a** and the CASSCF calculation of **2b**, one σ and two δ molecular orbitals and their antibonding counterparts were taken as the active space (Scheme 3).[29] Seven and six electrons were involved in the active spaces of **2a** and **2b**, respectively. In the CASSCF calculation of **3**, one σ, one π, and one δ molecular orbitals and their antibonding counterparts were taken as the active space (Scheme 4), in which six electrons were involved. Molecular orbitals that consist mainly of the e_g-like d orbitals were excluded from the active space of **2a**, **2b**, and **3** because they are at much different energies from the active orbitals. The MRMP2 and MCQDPT calculations were carried out with the reference wave function from the CASSCF and SA-CASSCF calculations, respectively. In these calculations, the 1s, 2s, and 2p orbitals of Cl ligand were kept to be frozen.

The CASSCF and SA-CASSCF calculations were performed with the GAMESS program package.[30] The MRMP2 and MCQDPT calculations were carried out with the MR2D program[31] implemented in the GAMESS package. The DFT-(B3LYP), CCSD, CCSD(T), BS-DFT(B3LYP), BS-CCSD, and BS-CCSD(T) calculations were performed with the Gaussian 03 (rev. C.02) program package.[32] Molecular orbitals were drawn by the MOLEKEL (ver. 4.3) program.[33]

1.3. Results and Discussions

1.3.1. $[Re_2Cl_8]^{2-}$ (1) with a Re–Re Direct Bond

The geometry of **1** in the $^1A_{1g}$ ground state was optimized with the CASSCF and MRMP2 methods, as shown in Table 1. At the CASSCF level of theory with both basis-I

and basis-II, the optimized Re–Re distance and Re–Re–Cl_{t1} angle are in good agreement with the experimental values, whereas the optimized Re–Cl_{t1} distance is somewhat longer than the experimental value. All these geometrical parameters are improved at the MRMP2 level of theory; the Re–Re distance and the Re–Re–Cl_{t1} angle are almost the same as their experimental values and the Re–Cl_{t1} distance considerably approaches its experimental value. Thus, the MRMP2 method reproduces well the geometry of **1** like the CASPT2 method.[18]

Relative energies and natural orbital populations of several important electronic states were evaluated by the CASSCF/basis-II and MRMP2/basis-II methods with the experimental geometry, as shown in Table 2. In the $^1A_{1g}$ ground state, the population of the δ orbital (1.52) is much smaller than the usual value (2.0) of a doubly occupied orbital and that of the δ* orbital (0.48) is much larger than the usual value (0.0) of an unoccupied orbital. These results suggest that the δ bonding interaction is very weak. Therefore, the multireference theoretical method should be applied to this complex. Actually, the weights of the main configuration ($\sigma^2\pi^4\delta^2$) and the second leading one ($\sigma^2\pi^4\delta^{*2}$) are evaluated to be 67 and 18 %, respectively, by the CASSCF method.

Table 1. Optimized Re–Re and Re–Cl_{t1} bond distances (in Å) and Re–Re–Cl_{t1} bond angle (in degree) of $[Re_2Cl_8]^{2-}$ (**1**)

method	*r*(Re–Re)	*r*(Re–Cl_{t1})	*a*(Re–Re–Cl_{t1})	
CASSCF	2.259	2.382	104.7	this work (basis-I)
	2.260	2.381	104.6	this work (basis-II)
MRMP2	2.236	2.342	103.8	this work (basis-I)
	2.250	2.341	103.1	this work (basis-II)
CASPT2	2.259	2.304	103.44	ref 18
expt	2.24	2.29	103.7	ref 1

Table 2. Relative energies (in eV) and natural orbital populations[a,b] of several important states of $[Re_2Cl_8]^{2-}$ (**1**), $[Re_2(\mu\text{-}Cl)_3Cl_6]^{2-}$ (**2a**), $[Re_2(\mu\text{-}Cl)_3Cl_6]^{-}$ (**2b**), and $[Re_2(\mu\text{-}Cl)_2Cl_8]^{2-}$ (**3**)

		relative energy			natural orbital population					
complex	state	CASSCF	MRMP2	expt	σ	σ*	π	π*	δ	δ*
1	$^1A_{1g}$	0.00	0.00		1.92	0.08	3.74	0.26	1.52	0.48
	$^3A_{2u}$	0.45	0.52		1.92	0.08	3.75	0.25	1.01	0.99
	$^7A_{2u}$	5.97	6.29		1.90	0.10	2.02	1.98	1.00	1.00
	$^9A_{1g}$	9.68	10.65		1.00	1.00	2.00	2.00	1.00	1.00
	$^1A_{2u}$	3.14	1.95	1.82[c]	1.92	0.08	3.70	0.30	1.04	0.96
2a	$^2E''$	0.00	0.00		1.87	0.13			3.47	1.53
	$^4E'$	0.34	0.36		1.87	0.13			2.93	2.07
2b	$^1A_1'$	0.00	0.00		1.62	0.38			2.18	1.82
	$^3A_2''$	0.08	0.07		1.62	0.38			2.12	1.88
	$^5A_1'$	0.26	0.21		1.62	0.38			2.01	1.99
	$^7A_2''$	1.09	1.94		1.00	1.00			2.00	2.00
3	^1A_g	0.02	0.03		1.00	1.00	0.99	1.01	0.97	1.03
	$^3B_{1u}$	0.02	0.02		1.00	1.00	0.99	1.01	0.97	1.03
	^5A_g	0.01	0.02		1.00	1.00	0.99	1.01	0.98	1.02
	$^7B_{1u}$	0.00	0.00		1.00	1.00	1.00	1.00	1.00	1.00

(a) Basis-II was employed. (b) Relative energies and natural orbital populations of **1**, **2b**, and **3** were evaluated by the CASSCF and MRMP2 method and those of **2a** were evaluated by the SA-CASSCF and MCQDPT method. (c) ref 19.

The natural orbital populations of the σ, π, and δ bonding orbitals are much larger than those of their antibonding counterparts, respectively, in the $^1A_{1g}$ ground state, as shown in Table 2. This result suggests that all σ, π, and δ bonding interactions contribute to the Re–Re bond. From these natural orbital populations, the Re–Re bond order[34] is evaluated to be 3.18 in the $^1A_{1g}$ ground state, which is much smaller than 4.0. This value is almost the same as the previous value (3.20) evaluated by the CASPT2 method.[18] In the $^3A_{2u}$ excited state, on the other hand, the population of the δ orbital is almost the same as that of the δ* orbital, whereas the populations of the σ, σ*, π, and π* orbitals in the $^3A_{2u}$ state are almost the same as those in the $^1A_{1g}$ state, respectively. This means that the δ bonding interaction disappears upon going to the $^3A_{2u}$ state from the $^1A_{1g}$ state, and that the energy difference between these two states corresponds to the approximate stabilization energy by the δ bonding interaction.[35,36] This energy difference is estimated to be 0.52 eV by the MRMP2 method. In the $^7A_{2u}$ state,[37] the population of the σ orbital is larger than that of the σ* orbital and the populations of the π and δ orbitals are almost the same as those of the π* and δ* orbitals, respectively, as shown in Table 2. This means that only one σ bonding interaction remains but the π and δ bonding interactions disappear in the $^7A_{2u}$ state. Thus, the energy difference between the $^7A_{2u}$ and $^3A_{2u}$ states is the approximate stabilization energy by the two components of degenerate π bonding interactions. This energy difference is evaluated to be 5.77 eV by the MRMP2 method.[36] In the $^9A_{1g}$ state,[37] the populations of the σ, σ*, π, π*, δ, and δ* orbitals are 1.00, which means that all Re–Re bonding interactions disappear. The energy difference between the $^7A_{2u}$ and $^9A_{1g}$ states corresponds to the approximate stabilization energy by the σ bonding interaction. This energy difference is evaluated to be 4.36 eV by the MRMP2 method.[36] These results are summarized, as follows: The σ, π, and δ bonding interactions yield the approximate stabilization energies 4.36, 2.89 (= 5.77/2), and 0.52 eV, respectively; note that two π bonds exist. The δ bonding interaction is much weaker than the π bonding interaction and the π

bonding interaction is much weaker than the σ bonding interaction, as expected. Although this result is not surprising, this is the first semiquantitative estimation of relative strengths of the σ, π, and δ bonding interactions of **1**.

The $^1A_{1g} \rightarrow {}^1A_{2u}$ (δ → δ*) excitation energy is evaluated to be 3.14 and 1.95 eV by the CASSCF and MRMP2 method, respectively. It is noted that although the CASSCF-calculated value is much larger than the experimental value (1.82 eV)[19] like the previous CASSCF-evaluated value,[17] the MRMP2-calculated value agrees well with the experimental value like the CASPT2-calculated value.[18] This result indicates that incorporation of dynamical electron correlation based on the multireference wave function is indispensable, as reported.[18]

The PECs of the $^1A_{1g}$, $^3A_{2u}$, $^7A_{2u}$, and $^9A_{1g}$ states were calculated by the MRMP2/basis-II method, as shown in Figure 1. The Re–Re distance at the energy minimum relates to the strength of the Re–Re bonding interaction. The energy minimum of the $^3A_{2u}$ state is at a slightly longer Re–Re distance (2.3 Å) than that of the $^1A_{1g}$ state (2.2 Å). Also, the shapes of the PECs of these two states resemble each other. These results arise from the fact that the weak δ bonding interaction disappears upon going to the $^3A_{2u}$ state from the $^1A_{1g}$ state. In contrast, the energy minimum of the $^7A_{2u}$ state is at a much longer Re–Re distance (2.8 Å) than that of the $^3A_{2u}$ state (2.3 Å). Also, it is noted that the PEC of the $^7A_{2u}$ state is very shallow, unlike those of the $^1A_{1g}$ and $^3A_{2u}$ states. These results are interpreted in terms that the stronger π bonding interaction disappears upon going to the $^7A_{2u}$ state from the $^3A_{1g}$ state. The PEC of the $^9A_{1g}$ state is completely repulsive because all Re–Re bonding interactions are absent in this state.

Natural orbital populations of the σ, π, δ, δ*, π*, and σ* orbitals evaluated by the CASSCF/basis-II method are presented as a function of the Re–Re distance in Figures 2a–c. In the $^1A_{1g}$ state, the population of the δ orbital becomes almost the same as that of the δ* orbital at *r*(Re–Re) = 3.6 Å, as shown in Figure 2a; in other words, the δ bonding interaction

disappears at this distance. On the other hand, the populations of the σ and π bonding orbitals are still larger than those of their antibonding counterparts, respectively, even when the Re–Re distance is longer than 3.6 Å. This result indicates that the σ and π bonding interactions still remain in this region. They disappear at *r*(Re–Re) = 4.6 and 6.0 Å, respectively. These results are useful to discuss what type of interaction contributes to the metal–metal bond in dinuclear metal complexes.

Energy differences between the $^1A_{1g}$ and $^3A_{2u}$ states and between the $^1A_{1g}$ and $^1A_{2u}$ states were also investigated by the DFT(B3LYP), CCSD, CCSD(T), BS-DFT(B3LYP), BS-CCSD, and BS-CCSD(T) methods, as shown in Table 3. The $^3A_{2u}$ state is calculated to be more stable than the $^1A_{1g}$ state by the DFT-(B3LYP) and CCSD methods. This result is completely different from the relative stability calculated by the MRMP2 method.[38] On the other hand, the CCSD(T) and all BS methods present the correct stability order of these three states. These results indicate that the BS-DFT(B3LYP), BS-CCSD, and BS-CCSD-(T) methods are useful to discuss bonding nature and the electronic state of the ground state in this complex, as reported previously.[20]

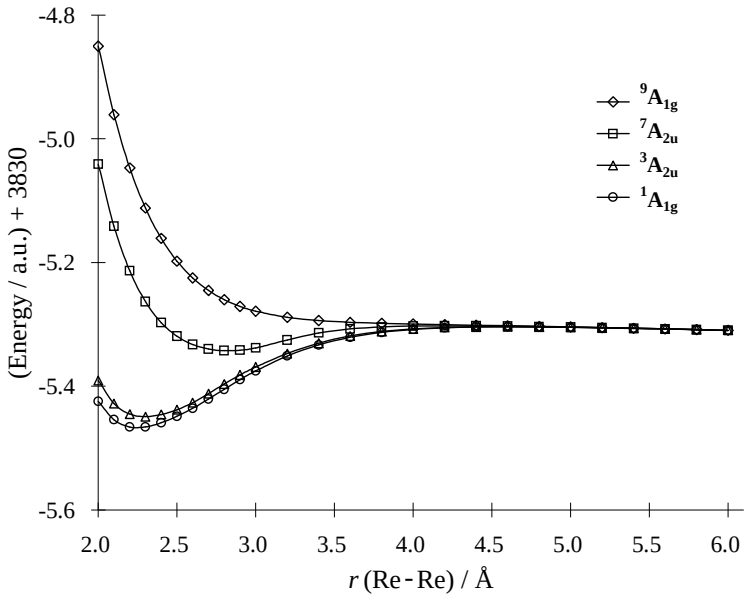

Figure 1. Potential energy curves of the $^1A_{1g}$, $^3A_{2u}$, $^7A_{2u}$, and $^9A_{1g}$ states of $[Re_2Cl_8]^{2-}$ (**1**). Basis-II was employed.

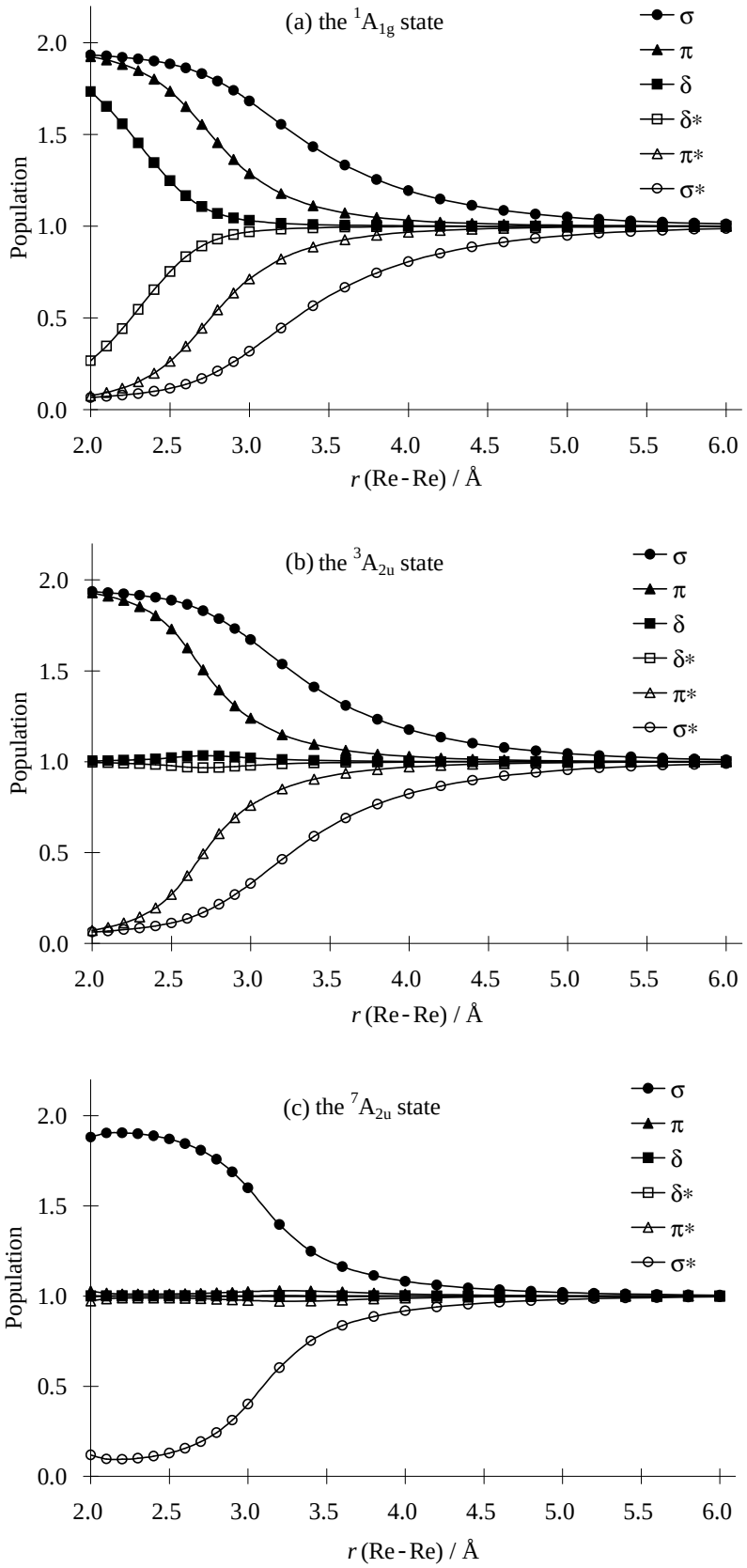

Figure 2. Natural orbital populations of the σ, π, δ, δ*, π*, and σ* orbitals in the $^1A_{1g}$, $^3A_{2u}$, and $^7A_{2u}$ states of $[Re_2Cl_8]^{2-}$ (**1**). Basis-II was employed.

Table 3. Comparisons of DFT(B3LYP), CCSD, CCSD(T), BS-DFT(B3LYP), BS-CCSD, and BS-CCSD(T) methods in Calculating Relative Energies of the $^1A_{1g}$, $^3A_{2u}$, and $^1A_{2u}$ states of $[Re_2Cl_8]^{2-}$ (**1**) and those of $^1A_1'$ and $^5A_1'$ states of $[Re_2(\mu\text{-}Cl)_3Cl_6]^-$ (**2b**)

complex	state	B3LYP	CCSD	CCSD(T)	BS-B3LYP	BS-CCSD	BS-CCSD(T)	expt[19]
basis-I								
1	$^1A_{1g}$	0.00	0.00	0.00	0.00	0.00	0.00	0.00
	$^3A_{2u}$	–0.30	–0.51	0.10	0.18	0.32	0.20	
	$^1A_{2u}$	0.70	0.80	0.69	1.18	1.61	0.62	1.82
2b	$^1A_1'$	0.00	0.00	0.00	0.00	0.00	0.00	
	$^5A_1'$	–1.83	–2.48	–2.25	0.14	–0.84	–0.66	
basis-II								
1	$^1A_{1g}$	0.00	0.00	0.00	0.00			0.00
	$^3A_{2u}$	–0.27	–0.49	0.15	0.19			
	$^1A_{2u}$	0.73	0.83	0.72	1.18			1.82
2b	$^1A_1'$	0.00	0.00	0.00	0.00			
	$^5A_1'$	–1.79	–2.49	–2.25	0.15			

1.3.2. Face-Sharing Complexes $[Re_2(\mu\text{-}Cl)_3Cl_6]^{2-}$ (2a) and $[Re_2(\mu\text{-}Cl)_3Cl_6]^-$ (2b)

In **2a**, the $^2E''$ and $^4E'$ states were investigated by the SA-CASSCF and MCQDPT methods because both states are degenerate. The $^2E''$ state is the ground state and the $^4E'$ excited state is calculated to be 0.36 eV above the $^2E''$ state by the MCQDPT/basis-II method, as shown in Table 2. In the $^2E''$ state, the natural orbital populations of the δ and δ* orbitals are 3.47 and 1.53, respectively. These values are much different from formal values (4.0 and 1.0 for the δ and δ* orbitals, respectively) in the pure $\sigma^2\delta^4\delta^{*1}$ configuration. This result suggests that the electronic structure of **2a** cannot be described well by one $\sigma^2\delta^4\delta^{*1}$ configuration. Actually, the weights of this configuration and the second leading one

($\sigma^2\delta^2\delta^{*3}$) are evaluated to be 72 and 12 %, respectively, by the SA-CASSCF method. Consistent with these results, the Re–Re bond order is only 1.84, which is much smaller than the formal value (2.5) in the pure $\sigma^2\delta^4\delta^{*1}$ configuration.

In the ^{4}E' excited state, the populations of the δ and δ* orbitals are 2.93 and 2.07, respectively; note the δ and δ* orbitals are doubly degenerate (see Scheme 3). Because the difference between these two populations (0.86) is much smaller than that in the ^{2}E" state (1.94) by about 1, the δ bonding interaction in the ^{4}E' state is much weaker than that in the ^{2}E" state. The populations of the σ and σ* orbitals are little different between these two states. Thus, the energy difference (0.36 eV) between these two states corresponds to the approximate stabilization energy by the two components of degenerate δ bonding interactions. These δ bonding interactions are much weaker than that of **1**. Its reason is easily understood in terms of the Re–Re distance and the Re oxidation state. In **2a**, the Re–Re distance is much longer than that of **1** because of the face-sharing bioctahedral geometry. Also, **2a** consists of Re(III) and Re(IV) centers, and **1** consists of two Re(III) centers. Because the d orbital of Re(IV) expands less than that of Re(III), the d_δ–d_δ overlap of **2a** is smaller than that in **1**. Because of these two factors, the δ bonding interaction is weaker in **2a** than in **1**.

Relative energies and natural orbital populations of the other face-sharing rhenium complex (**2b**) were investigated by the CASSCF/basis-II and MRMP2/basis-II methods, as shown in Table 2. The $^1A_1$' state is the ground state and the $^3A_2$" and $^5A_1$' excited states are evaluated to be at slightly higher energies than the ground state with the MRMP2 method by 0.07 and 0.21 eV, respectively (see Table 2). The $^7A_2$" excited state is at much higher energy than the $^5A_1$' state by 1.73 eV.

In the $^1A_1$' ground state, the populations of the δ and δ* orbitals are 2.18 and 1.82, respectively (see Table 2), which clearly shows that the δ bonding interaction is very weak because both populations are close to each other. This means that a multireference method

such as MRMP2 or CASPT2 should be employed to investigate **2b** like **1** and **2a**. Actually, the weight of the main configuration ($\sigma^2\delta^4$) is evaluated to be very small (18 %) by the CASSCF method.[39] Consistent with the very small weight of the $\sigma^2\delta^4$ configuration, the Re–Re bond order is only 0.80. In the $^5A_1'$ excited state, the populations of the δ and δ* orbitals are 2.01 and 1.99, respectively. This means that the δ bonding interaction is negligibly small in this state. The energy difference between the $^1A_1'$ and $^5A_1'$ states is evaluated to be 0.21 eV by the MRMP2 method, which corresponds to the approximate stabilization energy by the two components of degenerate δ bonding interactions.

The strength of the σ bonding interaction in **2b** is also worthy of investigation. The populations of the σ and σ* orbitals are 1.62 and 0.38, respectively, in both the $^1A_1'$ and $^5A_1'$ states, as shown in Table 2. These values suggest that the σ bonding interaction is not strong very much unlike those of **1** and **2a**. In the $^5A_1'$ state, the weights of the $\sigma^2\delta^2\sigma^{*2}$ and $\delta^2\delta^{*2}\sigma^{*2}$ configurations are evaluated to be 73 and 11 %, respectively, by the CASSCF method. In the $^7A_2''$ state, the population of the σ orbital is the same as that of the σ* orbital, which indicate that even the σ bonding interaction disappears in this state. Thus, the energy difference between the $^5A_1'$ and $^7A_2''$ states (1.73 eV) corresponds to the approximate stabilization energy by the σ bonding interaction, which is much smaller than that (4.36 eV) of **1**. The σ bond order in the $^1A_1'$ state of **2b** (0.62) is also considerably smaller than those in the $^1A_{1g}$ state of **1** (0.92) and the $^2E''$ state of **2a** (0.87). This weak σ bond of **2b** is interpreted, as follows: One factor is the long Re–Re distance; because the Re–Re distance of **2b** (2.704 Å) is much longer than that of **1** (2.24 Å), the d_σ–d_σ overlap between two Re centers is much smaller in **2b** than in **1**. The other factor is the oxidation state of the Re center. In **1**, the populations of the σ and σ* orbitals are 1.83 and 0.17, respectively, when the Re–Re distance is taken to be the same as the experimental distance (2.704 Å) of **2b**, as shown in Figure 2a. Thus, the σ bond order of **1** with this Re–Re distance is 0.83, which is considerably larger than that of **2b** (0.62), even though the Re–Re

distance is the same. This result clearly shows that not only the Re–Re distance but also the other factor are responsible for the weaker σ bond of **2b** than that of **1**. Such a factor is the oxidation state of the Re center. As discussed above, **1** consists of two Re(III) atoms, but **2b** consists of two Re(IV) atoms. The less-expanding d orbital of Re(IV) than that of Re(III) leads to smaller d_σ–d_σ overlap of **2b** than that of **1**. These two factors are responsible to the weaker σ bonding interaction of **2b** than that of **1**.

It is of considerable interest to make a comparison between **2a** and **2b**, because the electronic structure is much different despite the similar geometry and similar d electron number; both complexes take the face-sharing structure and **2b** has fewer d electrons than **2a** by only one. In **2a**, the main configuration is $\sigma^2\delta^4\delta^{*1}$. It is expected that one d electron is lost from the δ* orbital upon going to **2b** from **2a** and the Re–Re bond of **2b** is stronger than that of **2a**. However, natural orbital population of the δ orbital extremely decreases and that of the δ* orbital rather increases in **2b**, as shown in Table 2, against the above expectation. These population changes suggest that one d electron is lost not from the δ* orbital but from the δ orbital. Thus, the electronic structure of **2b** cannot be understood in terms of a usual orbital picture. Also, it is noted that the Re–Re bond distance becomes longer in **2b** than in **2a**, as shown in Table A1 (Appendix). One plausible reason of the longer Re–Re distance in **2b** is that one electron loss occurs in the δ orbital upon going to **2b** from **2a**. This induces weakening of the δ bonding interaction. It is worthwhile to discuss the reason that one electron loss occurs not in the δ* orbital but in the δ orbital in **2a**. It is likely that the electron repulsion of the d-shell is larger in **2b** than in **2a** because the d orbital of the Re(IV)–Re(IV) core is more compact than that of the Re(III)–Re(IV) core. Also, Coulomb repulsion in the d-shell is larger in the $\sigma^2\delta^4$ configuration than in the $\sigma^2\delta^3\delta^{*1}$ configuration. If the energy separation between the δ and δ* orbitals is sufficiently large, one δ* electron loss occurs in the $\sigma^2\delta^4\delta^{*1}$ configuration to afford the $\sigma^2\delta^4$ configuration upon going to **2b** from **2a**. In these complexes, however, the δ–δ* energy separation is small. Thus, one δ

electron loss occurs in the $\sigma^2\delta^4\delta^{*1}$ configuration to afford the $\sigma^2\delta^3\delta^{*1}$ configuration, so as to decrease Coulomb repulsion in the d-shell.

The DFT(B3LYP), CCSD, CCSD(T), BS-DFT(B3LYP), BS-CCSD, and BS-CCSD(T) methods were also applied to **2b**, as shown in Table 3. The $^5A_1'$ state is evaluated to be more stable than the $^1A_1'$ state by the methods other than BS-DFT(B3LYP). These results are different from the results by the MRMP2 calculations.[38] On the other hand, the DFT(B3LYP) method presents a similar result by the MRMP2 calculation, which indicates that the DFT(B3LYP) method is useful to present correctly the ground state of **2b**.

1.3.3. Edge-Sharing Complex $[Re_2(\mu\text{-}Cl)_2Cl_8]^{2-}$ (3)

Relative energies and natural orbital populations of the ^1A_g, $^3B_{1u}$, ^5A_g, and $^7B_{1u}$ states were calculated by the CASSCF/basis-II and MRMP2/basis-II methods, as shown in Table 2. In all these states, the populations of the σ, π, and δ bonding orbitals are almost the same as those of their antibonding counterparts, respectively. This means that the σ, π, and δ bonding interactions do not contribute to the Re–Re bond in these four states. The weights of several important electron configurations are evaluated to be very small by the CASSCF method; 6 % for both the $\sigma^2\pi^2\delta^2$ and $\sigma^2\pi^2\delta^{*2}$ configurations in the ^1A_g state, 7 % for both the $\sigma^2\pi^2\delta^1\delta^{*1}$ and $\sigma^2\delta^1\delta^{*1}\pi^{*2}$ configurations in the $^3B_{1u}$ state, and 16 % for both the $\sigma^2\pi^1\delta^1\delta^{*1}\pi^{*1}$ and $\pi^1\delta^1\delta^{*1}\pi^{*1}\sigma^{*2}$ configurations in the ^5A_g state. As a result, these four states are in almost the same energy (within 0.03 eV). In other words, the low spin state is not stabilized by the Re–Re bonding interaction unlike **1**, **2a**, and **2b**. These results are consistent with the experimental report that **3** is not diamagnetic but paramagnetic.[12]

The absence of the Re–Re bonding interaction arises from the long Re–Re distance (3.691 Å) due to the edge-sharing geometry. The oxidation state of Re(IV) center is also responsible for the absence of the Re–Re bonding interaction, as follows: Because the d orbital of Re(IV) expands less than that of Re(III), the σ, π, and δ bonding interactions in **3**

are weaker than those in **1**. For instance, the population of the σ orbital is almost the same as that of the σ* orbital in those four states of **3**, as shown in Table 2, whereas the population of the σ orbital (1.30) is considerably larger than that of the σ* orbital in the $^1A_{1g}$ state of **1** at the same Re–Re distance (3.691 Å) (see Figure 2a). These results clearly show that the σ bonding interaction disappears in **3** but still remains in **1** at *r*(Re–Re) = 3.691 Å.

Three d electrons are localized in three d orbitals of each Re center because the Re–Re interaction is absent. As a result, the four states, ^1A_g, $^3B_{1u}$, ^5A_g, and $^7B_{1u}$, emerge from the electron configurations in which six electrons occupy the σ, π, δ, δ*, π*, and σ* orbitals in D_{2h} symmetry. The other states are at much higher energy than these four states by over 1.0 eV (see Table A2 in Appendix) because those states consist mainly of the high-energy excited configurations.

1.4. Conclusions

Four dinuclear rhenium complexes, $[Re_2Cl_8]^{2-}$ (**1**), $[Re_2(\mu\text{-}Cl)_3Cl_6]^{2-}$ (**2a**), $[Re_2(\mu\text{-}Cl)_3Cl_6]^{-}$ (**2b**), and $[Re_2(\mu\text{-}Cl)_2Cl_8]^{2-}$ (**3**), were theoretically investigated by the CASSCF, MRMP2, SACASSCF, and MCQDPT methods. In the $^1A_{1g}$ ground state of **1**, the weights of the $\sigma^2\pi^4\delta^2$ and $\sigma^2\pi^4\delta^{*2}$ configurations are 67 and 18 %, respectively, where weights evaluated by either the CASSCF/basis-II or the SA-CASSCF/basis-II method are presented hereafter. The energy difference between the $^1A_{1g}$ and $^3A_{2u}$ states, which corresponds to the approximate stabilization energy by the δ bonding interaction, is evaluated to be 0.52 eV by the MRMP2/basis-II method. The $^7A_{2u}$ state is much less stable than the $^3A_{2u}$ state by 5.77 eV. This is because the bonding interactions of the two π orbitals disappear upon going to the $^7A_{2u}$ state from the $^3A_{2u}$ state. The $^9A_{1g}$ state is further less stable than the $^7A_{2u}$ state by 4.36 eV because the σ bonding interaction disappears upon going to the $^9A_{1g}$ state from the $^7A_{2u}$ state. Thus, the σ, π, and δ bonding interactions yield the approximate stabilization energies of 4.36, 2.89 (= 5.77/2), and 0.52 eV, respectively.

In the $^1A_{1g}$ state, the δ bonding interaction completely disappears at *r*(Re–Re) = 3.6 Å, whereas the π and σ bonding interactions completely disappear at *r*(Re–Re) = 4.6 and 6.0 Å, respectively.

In the $^2E''$ ground state of **2a**, the weights of the $\sigma^2\delta^4\delta^{*1}$ and $\sigma^2\delta^3\delta^{*2}$ configurations are 72 and 12 %, respectively. The natural orbital populations clearly show that the δ bonding interaction in the $^4E'$ state is much weaker than that in the $^2E''$ state. As a result, the former state is evaluated to be 0.36 eV less stable than the latter one. These results indicate that the δ bonding interaction is weaker in **2a** than in **1**. In the $^1A_1'$ ground state of **2b**, the weight of the $\sigma^2\delta^4$ configuration is evaluated to be 18 %. The energy difference between the $^1A_1'$ and $^5A_1'$ states is evaluated to be 0.21 eV by the MRMP2/basis-II method, which corresponds to the approximate stabilization energy by the two components of degenerate δ bonding interactions. The σ bonding interaction is also weak in this complex, as follows: In the $^5A_1'$ state, the weights of the $\sigma^2\delta^2\delta^{*2}$ and $\delta^2\delta^{*2}\sigma^{*2}$ configurations are 73 and 11 %, respectively. The energy difference between the $^5A_1'$ and $^7A_2''$ states is evaluated to be 1.73 eV by the MRMP2/basis-II method, which corresponds to the approximate stabilization energy by the σ bonding interaction. This approximate stabilization energy is much smaller than that of **1**. The bonding nature and the electronic structure of **2b** are much different from the expectation based on a usual orbital picture that one d electron is lost from the δ* orbital upon going to **2b** from **2a** and the δ bonding interaction becomes stronger in **2b**. However, our theoretical calculation presents completely different results from the above expectation; the natural orbital population of the δ orbital decreases by 1.29 and that of the δ* orbital increases by 0.29, which indicates that one electron loss occurs not in the δ* orbital but in the δ orbital upon going to **2b** from **2a**. These unexpected results are interpreted in terms that one electron loss occurs in the δ orbital so as to decrease Coulomb repulsion in the d-shell because the δ–δ* energy separation is very small.

In **3**, the σ, π, and δ bonding interactions do not contribute to the Re–Re bond. As a

result, the low spin ^1A_g state is not stabilized by these bonding interactions unlike **1**, **2a**, and **2b**. Four states, ^1A_g, $^3B_{1u}$, ^5A_g, and $^7B_{1u}$, are in almost the same energy within 0.03 eV. This result is consistent with the experimental report that **3** is paramagnetic.[12]

The above mentioned energy difference between the ground and low-energy excited states lead to the conclusion that the Re–Re bonding interactions in the order **1** > **2a** > **2b** >> **3**, which is interpreted in terms of the Re–Re distance and the Re oxidation state.

1.5. Appendix

Scheme A1.

$[Re_2(\mu\text{-}Cl)_3Cl_6]^{2-}$ (**2a**) and $[Re_2(\mu\text{-}Cl)_3Cl_6]^{-}$ (**2b**)

(A) d_{eg} - d_{eg} orbitals including Re - Cl bonding interactions

a b c d

(B) Re - Re interaction orbitals

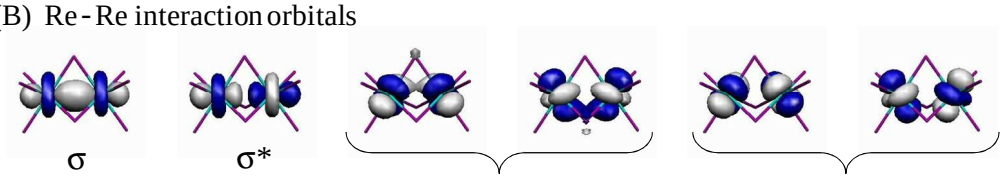

σ σ* δ δ*

(C) d_{eg} - d_{eg} orbitals including Re - Cl antibonding interactions

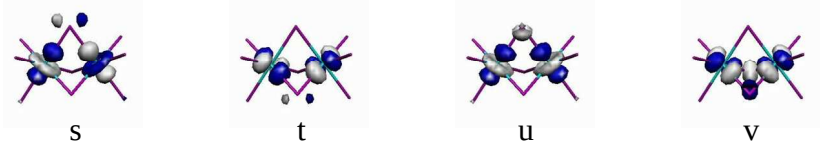

s t u v

Scheme A2. Several important molecular orbitals of $[Re_2(\mu\text{-}Cl)_2Cl_8]^{2-}$ (**3**)

$[Re_2(\mu\text{-}Cl)_2Cl_8]^{2-}$ (**3**)

(A) d_{eg} - d_{eg} orbitals including Re - Cl bonding interactions

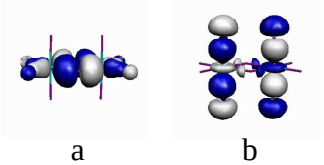

a b

(B) Re - Re interaction orbitals

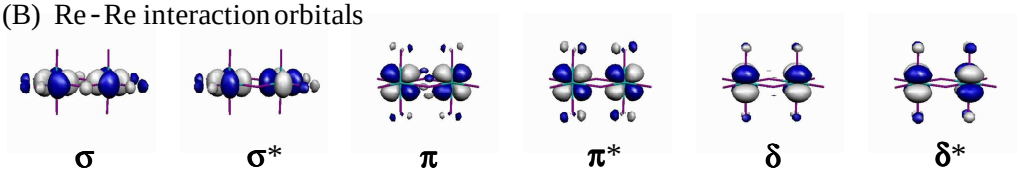

σ **σ*** **π** **π*** **δ** **δ***

(C) d_{eg} - d_{eg} orbitals including Re - Cl antibonding interactions

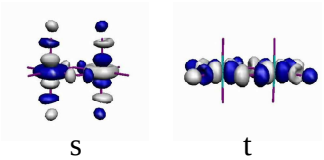

s t

Table A1. Experimental bond distances (in angstrom) and bond angles (in degree) of $[Re_2Cl_8]^{2-}$ (**1**), $[Re_2(\mu\text{-}Cl)_3Cl_6]^{2-}$ (**2a**), $[Re_2(\mu\text{-}Cl)_3Cl_6]^{-}$ (**2b**), and $[Re_2(\mu\text{-}Cl)_2Cl_8]^{2-}$ (**3**) from X-ray analyses[1,5,12]

		bond distance				bond angle				
complex	symmetry	Re–Re	Re–Cl_b	Re–Cl_{t1}	Re–Cl_{t2}	Re–Re–Cl_{t1}	Cl_b–Re–Cl_b	Cl_{t1}–Re–Cl_{t1}	Cl_{t2}–Re–Clt_2	ref
1	D_{4h}	2.24		2.29		103.7				1
2a	D_{3h}	2.473	2.424	2.322			96.3	90.6		5
2b	D_{3h}	2.704	2.407	2.283			91.5	91.4		5
3	D_{2h}	3.691	2.451	2.330	2.304		82.31	177.74	95.53	12

Table A2. Relative Energies (in eV) and Natural Orbital Populations of $[Re_2(\mu\text{-}Cl)_2Cl_8]^{2-}$ (**3**) by the CASSCF/Basis-II and MRMP2/Basis-II Methods

		relative energy		natural orbital population					
complex	state	CASSCF	MRMP2	σ	σ*	π	π*	δ	δ*
3	^1A_g	0.02	0.03	1.00	1.00	0.99	1.01	0.97	1.03
	$^1B_{1g}$	3.41	2.04	1.27	1.29	0.61	0.63	1.09	1.12
	$^1B_{2g}$	3.38	2.00	1.59	1.58	0.72	0.71	0.69	0.72
	$^1B_{3g}$	3.40	2.15	1.28	1.29	0.71	0.73	0.94	1.06
	^1A_u	3.42	2.04	1.28	1.27	0.62	0.63	1.09	1.11
	$^1B_{1u}$	3.51	2.21	1.00	1.00	1.00	1.00	1.00	1.00
	$^1B_{2u}$	3.40	2.14	1.28	1.27	0.72	0.73	0.94	1.06
	$^1B_{3u}$	3.39	2.01	1.58	1.57	0.70	0.73	0.69	0.73
	^3A_g	1.76	1.13	1.00	1.00	1.00	1.00	0.96	1.04
	$^3B_{1g}$	1.71	1.10	1.28	1.26	0.98	1.02	0.71	0.75
	$^3B_{2g}$	1.79	1.10	1.00	1.00	1.00	1.02	0.98	1.01
	$^3B_{3g}$	1.70	1.08	1.26	1.26	0.73	0.74	0.96	1.04
	^3A_u	1.71	1.10	1.27	1.27	0.98	1.02	0.72	0.74
	$^3B_{1u}$	0.02	0.02	1.00	1.00	0.99	1.01	0.97	1.03
	$^3B_{2u}$	1.69	1.08	1.27	1.26	0.73	0.74	0.96	1.04
	$^3B_{3u}$	1.79	1.10	1.00	1.00	1.01	1.01	0.98	1.01
	^5A_g	0.01	0.02	1.00	1.00	0.99	1.01	0.98	1.02
	$^5B_{1g}$	1.71	1.10	1.26	1.27	1.00	1.00	0.73	0.74
	$^5B_{2g}$	1.78	1.07	1.00	1.00	1.02	0.99	0.98	1.01
	$^5B_{3g}$	1.69	1.08	1.27	1.26	0.73	0.74	1.00	1.00
	^5A_u	1.71	1.08	1.29	1.25	1.00	1.00	0.71	0.75
	$^5B_{1u}$	1.75	1.13	1.00	1.00	1.00	1.00	1.00	1.00
	$^5B_{2u}$	1.70	1.09	1.26	1.27	0.73	0.74	1.00	1.00
	$^5B_{3u}$	1.78	1.07	1.00	1.00	0.98	1.03	0.97	1.02
	$^7B_{1u}$	0.00	0.00	1.00	1.00	1.00	1.00	1.00	1.00

Table A3. Natural orbital populations of $[Re_2(\mu\text{-}Cl)_3Cl_9]^{2-}$ (**2a**), $[Re_2(\mu\text{-}Cl)_3Cl_9]^{-}$ (**2b**), and $[Re_2(\mu\text{-}Cl)_2Cl_8]^{2-}$ (**3**) by the CAS-CI method

		natural orbital[a]													
	state	a	b	c	d	σ	σ*	π	π*	δ	δ*	s	t	u	v
2a	$^2E''$	2.00	2.00	1.99	1.99	1.87	0.13			3.46	1.53	0.01	0.01	0.00	0.00
	$^4E'$	2.00	2.00	1.99	1.99	1.87	0.13			2.94	2.06	0.01	0.01	0.00	0.00
2b	$^1A_1'$	2.00	2.00	1.99	1.99	1.66	0.34			2.20	1.80	0.00	0.00	0.00	0.00
	$^3A_2''$	2.00	2.00	1.99	1.99	1.66	0.34			2.14	1.86	0.00	0.00	0.00	0.00
	$^5A_1'$	2.00	2.00	1.99	1.99	1.66	0.34			2.02	1.98	0.00	0.00	0.00	0.00
	$^7A_2''$	2.00	2.00	2.00	2.00	1.00	1.00			2.00	2.00	0.00	0.00	0.00	0.00
3	^1A_g	2.00	2.00			1.00	1.00	0.99	1.01	0.97	1.03	0.00	0.00		
	$^3B_{1u}$	2.00	2.00			1.00	1.00	0.99	1.01	0.97	1.03	0.00	0.00		
	^5A_g	2.00	2.00			1.00	1.00	0.99	1.01	0.98	1.02	0.00	0.00		
	$^7B_{1u}$	2.00	2.00			1.00	1.00	1.00	1.00	1.00	1.00	0.00	0.00		

(a) see Schemes A1 and A2

References and Notes

(1) (a) Cotton, F. A.; Harris, C. B. *Inorg. Chem.* **1965**, *4*, 330. (b) Cotton, F. A. *Inorg. Chem.* **1965**, *4*, 334.

(2) Brencic, J. V.; Cotton, F. A. *Inorg. Chem.* **1969**, *8*, 7.

(3) Cotton, F. A.; Daniels, L.; Davison, A.; Orvig, C. *Inorg. Chem.* **1981**, *20*, 3051.

(4) Cotton, F. A.; Bratton, W. K. *J. Am. Chem. Soc.* **1965**, *87*, 921.

(5) Heath, G. A.; McGrady, J. E.; Raptis, R. G.; Willis, A. C. *Inorg. Chem.* **1996**, *35*, 6838.

(6) Hauck, H. G.; Klingelhöfer, P.; Müller, U.; Dehnicke, K. *Z. Anorg. Allg. Chem.* **1984**, *510*, 180.

(7) Baranov, A. I.; Khvorykh, G. V.; Troyanov, S. I. *Z. Anorg. Allg. Chem.* **1999**, *625*, 1240.

(8) Kistenmacher, T. J.; Stucky, G. D. *Inorg. Chem.* **1971**, *10*, 122.

(9) Wessel, G. J.; Ijdo, D. J. W. *Acta Crystallogr.* **1957**, *10*, 466.

(10) Saillant, R.; Jackson, R. B.; Streib, W. E.; Folting, K.; Wentworth, R. A. D. *Inorg. Chem.* **1971**, *10*, 1453.

(11) Watson, W. H., Jr.; Waser, J. *Acta Crystallogr.* **1958**, *11*, 689.

(12) Beck, J.; K.-Buschbaum, M.; Wolf, F. *Z. Anorg. Allg. Chem.* **1999**, *625*, 975.

(13) Khvorykh, G. V.; Troyanov, S. I.; Baranov, A. I.; Serov, A. A. *Z. Anorg. Allg. Chem.* **1998**, *624*, 1026.

(14) Mucker, K.; Smith, G. S.; Johnson, Q. *Acta Crystallogr.* **1968**, *B24*, 874.

(15) Bursten, B. E.; Cotton, F. A.; Fanwick, P. E.; Stanley, G. G.; Walton, R. A. *J. Am. Chem. Soc.* **1983**, *105*, 2606.

(16) Hay, P. J. *J. Am. Chem. Soc.* **1982**, *104*, 7007.

(17) Blaudeau, J.-P.; Ross, R. B.; Pitzer, R. M. *J. Phys. Chem.* **1994**, *98*, 7123.

(18) Gagliardi, L.; Roos, B. O. *Inorg. Chem.* **2003**, *42*, 1599.

(19) (a) Cowman, C. D.; Gray, H. B. *J. Am. Chem. Soc.* **1973**, *95*, 8177. (b) Trogler, W. C.; Gray, H. B. *Acc. Chem. Res.* **1978**, *11*, 232.

(20) (a) McGrady, J. E.; Stranger, R.; Lovell, T. *J. Phys. Chem. A* **1997**, *101*, 6265. (b) McGrady, J. E.; Lovell, T.; Stranger, R. *Inorg. Chem.* **1997**, *36*, 3242. (c) McGrady, J. E.; Stranger, R.; Lovell, T. *Inorg. Chem.* **1998**, *37*, 3802. (d) Stranger, R.; Lovell, T. McGrady, J. E. *Inorg. Chem.* **1999**, *38*, 5510. (e) Stranger, R.; Turner, A.; Delfs, C. D. *Inorg. Chem.* **2001**, *40*, 4093. (f) Cavigliasso, G.; Stranger, R. *Inorg. Chem.* **2004**, *43*, 2368. (g) Petrie, S.; Stranger, R. *Inorg. Chem.* **2004**, *43*, 2597. (h) Cavigliasso, G.; Comba, P.; Stranger, R. *Inorg. Chem.* **2004**, *43*, 6734. (i) Cavigliasso, G.; Stranger, R. *Inorg. Chem.* **2005**, *44*, 5081.

(21) (a) Hirao, K. *Chem. Phys. Lett.* **1992**, *190*, 374. (b) Hirao, K. *Chem. Phys. Lett.* **1992**, *196*, 397. (c) Hirao, K. *Int. J. Quantum Chem.* **1992**, *S26*, 517.

(22) (a) Nakano, H. *J. Chem. Phys.* **1993**, *99*, 7983. (b) Nakano, H. *Chem. Phys. Lett.* **1993**, *207*, 372.

(23) (a) Becke, A. D. *Phys. Rev. A* **1988**, *38*, 3098. (b) Becke, A. D. *J. Chem.Phys.* **1993**, *98*, 5648.

(24) Lee, C.; Yang, W.; Parr, R. G. *Phys. Rev. B* **1988**, *37*, 785.

(25) Hay, P. J.; Wadt, W. R. *J. Chem. Phys.* **1985**, *82*, 299.

(26) Couty, M.; Hall, M. B. *J. Comput. Chem.* **1996**, *17*, 1359.

(27) Ehlers, A. W.; Böhme, M.; Dapprich, S.; Gobbi, A.; Höllwarth, A.; Jonas, V.; Köhler, K. F.; Stegmann, R.; Veldkamp, A.; G. Frenking. *Chem. Phys. Lett.* **1993**, *208*, 111.

(28) Woon, D. E.; Dunning, T. H., Jr. *J. Chem. Phys.* **1993**, *98*, 1358.

(29) Complexes **2a**, **2b**, and **3** were also investigated by the CAS-CI calculations here. These calculations present almost the same natural orbital populations as those of either CASSCF or SA-CASSCF calculation, indicating that the active spaces adapted here are reasonable; see Table A3 and Schemes A1 and A2 in Appendix.

(30) Schmidt, M. W.; Baldridge, K. K.; Boatz, J. A.; Albert, S. T.; Gordon, M. S.; Jensen, J. J.; Koseki, S.; Matsunaga, N.; Nguyen, K. A.; Su, S.; Windus, T. L.; Dupuis, M.; Montgomery, J. A. *J. Comput. Chem.* **1993**, *14*, 1347.

(31) Nakano, H. *MR2D*, version 2.0; University of Tokyo: Tokyo, Japan, 1995.

(32) Frisch, M. J.; Trucks, G. W.; Schlegel, H. B.; Scuseria, G. E.; Robb, M. A.; Cheeseman, J. R.; Montgomery, J. A., Jr.; Vreven, T.; Kudin, K. N.; Burant, J. C.; Millam, J. M.; Iyengar, S. S.; Tomasi, J.; Barone, V.; Mennucci, B.; Cossi, M.; Scalmani, G.; Rega, N.; Petersson, G. A.; Nakatsuji, H.; Hada, M.; Ehara, M.; Toyota, K.; Fukuda, R.; Hasegawa, J.; Ishida, M.; Nakajima, T.; Honda, Y.; Kitao, O.; Nakai, H.; Klene, M.; Li, X.; Knox, J. E.; Hratchian, H. P.; Cross, J. B.; Bakken, V.; Adamo, C.; Jaramillo, J.; Gomperts, R.; Stratmann, R. E.; Yazyev, O.; Austin, A. J.; Cammi, R.; Pomelli, C.; Ochterski, J. W.; Ayala, P. Y.; Morokuma, K.; Voth, G. A.; Salvador, P.; Dannenberg, J. J.; Zakrzewski, V. G.; Dapprich, S.; Daniels, A. D.; Strain, M. C.; Farkas, O.; Malick, D. K.; Rabuck, A. D.; Raghavachari, K.; Foresman, J. B.; Ortiz, J. V.; Cui, Q.; Baboul, A. G.; Clifford, S.; Cioslowski, J.; Stefanov, B. B.; Liu, G.; Liashenko, A.; Piskorz, P.; Komaromi, I.; Martin, R. L.; Fox, D. J.; Keith, T.; Al-Laham, M. A.; Peng, C. Y.; Nanayakkara, A.; Challacombe, M.; Gill, P. M. W.; Johnson, B.; Chen, W.; Wong, M. W.; Gonzalez, C.; Pople, J. A. *Gaussian 03*, revision C.02; Gaussian, Inc.: Wallingford, CT, 2004.

(33) (a) Flükiger, P.; Lüthi, H. P.; Portmann, S.; Weber, J. *MOLEKEL*, version 4.3; Scientific Computing: Manno, Switzerland, 2000–2002. (b) Portmann, S.; Lüthi, H. P. *CHIMIA* **2000**, 54, 766.

(34) The bond order is defined in usual way: Bond order = {(sum of the natural orbital populations of bonding orbitals) – (sum of the natural orbital populations of antibonding orbitals)}/2.

(35) The stabilization energy by the δ bonding interaction corresponds to the energy difference between the $^1A_{1g}$ and $^3A_{2u}$ states when orbital relaxation is negligibly small. Because this relaxation occurs more or less, the energy difference is not exactly the same as the stabilization energy by the δ bonding interaction. However, it is likely that the energy difference approximately corresponds to the stabilization energy by the δ bonding interaction, because the orbital relaxation is not large, as suggested by almost the same populations of σ, σ*, π, and π* orbitals between the $^1A_{1g}$ and $^3A_{2u}$ states.

(36) Incorporation of spin−orbit coupling interaction is necessary for highly quantitative discussion, as reported by Gagliardi and Roos.[18] It is likely that semiquantitatively reliable discussion is presented here about the stabilization energies by the σ, π, and δ bonding interactions, at least, because the spin−orbit coupling is mainly one-center interaction.

(37) The $^{7}A_{2u}$ and $^{9}A_{1g}$ states were calculated here to evaluate the strengths of the σ, π, and δ bonding interactions from the energy differences among the $^{1}A_{1g}$, $^{3}A_{2u}$, $^{7}A_{2u}$, and $^{9}A_{1g}$ states.

(38) This is probably because the multiconfigurational nature is strong in this complex. The BS methods should be carefully applied to estimation of energy difference between the ground and low-energy excited states when they exhibit multiconfigurational nature.

(39) We ascertained that the weights of the other electron configurations are smaller than 14 %.

Chapter 2

Theoretical Investigation of μ-O-Bridged Dinuclear Re Complexes: Electronic Structure, Bonding Nature, and Absorption Spectra

2.1. Introduction

Sulfur-bridged,[1] halogen-bridged,[2–6] and oxo-bridged[7–11] dinuclear complexes are very interesting because the metal centers take various oxidation states and various coordination numbers in these compounds. Especially, oxobridged rhenium, tungsten, and molybdenum complexes have attracted a lot of interests because their metal–metal distances are much shorter than those of other complexes, i.e., they should have strong metal–metal bond interaction.[7–11] Also, they exhibit characteristic adsorption bands in visible region. However, the details of electronic structures, metal–metal bonding interactions, and origin of absorption spectra have not been clarified yet.

These dinuclear transition metal complexes are one of the most challenging research subjects in theoretical chemistry because they have a lot of low-lying excited states in general. For such systems, a multiconfigurational self consistent-field (MCSCF) method[12] should be applied to present even qualitatively correct results. Furthermore, the dynamical electron correlation effects should be taken into consideration by ab initio multireference theory. Several multireference methods such as multireference singles and doubles configuration interaction method (MR-SDCI), multireference second-order Møller–Plesset perturbation theory (MRMP2),[13] and multiconfigurational second-order quasi degenerate perturbation theory (MCQDPT)[14] have been proposed as such methods. Although they all require much more computational efforts than the conventional DFT method, they were applied to π-conjugated[15] and transition metal systems[16,17] quite successfully.

Stranger and coworkers theoretically investigated various dinuclear complexes of rhenium, technetium, tungsten, and molybdenum with the broken symmetry (BS) DFT

method to clarify the nature of the ground state and some low-lying excited states.[18] Also, detailed knowledge including low-lying excited states of $[Re_2Cl_8]^{2-}$, $[Re_2Cl_9]^{-}$, $[Re_2Cl_9]^{2-}$, and $[Re_2Cl_{10}]^{2-}$ were presented by ab initio multireference theories recently.[19,20]

$[Re^{III}Re^{IV}(\mu\text{-}O)_2(Metpa)_2]^{3+}$, $[Re^{IV}{}_2(\mu\text{-}O)_2(Metpa)_2]^{4+}$, and $[Re^{IV}{}_2(\mu\text{-}O)_2(Me_2tpa)_2]^{4+}$ (Metpa = ((6-methyl-2-pyridyl)-methyl)bis(2-pyridylmethyl)-amine, Me_2tpa = bis((6-methyl-2-pyridyl)methyl)(2-pyridylmethyl)amine) synthesized by Umakoshi et al. exhibit characteristic absorption bands in visible region and these absorptions were on the basis of the metal–metal bonding and antibonding orbitals.[10] It is also noted that the Re–Re bond length (2.426 Å) of $[Re^{III}Re^{IV}(\mu\text{-}O)_2(Metpa)_2]^{3+}$ is considerably longer than that (2.368 Å) of $[Re_2{}^{IV}(\mu\text{-}O)_2(Metpa)_2]^{4+}$. This result was experimentally interpreted in terms that $[Re^{III}Re^{IV}(\mu\text{-}O)_2(Metpa)_2]^{3+}$ and $[Re^{IV}{}_2(\mu\text{-}O)_2(Metpa)_2]^{4+}$ which take the electron configurations of $\sigma^2\pi^2\delta^2\delta^{*1}$ and $\sigma^2\pi^2\delta^2$, respectively, and the occupation of the δ^* orbital leads to the longer Re–Re distance of $[Re^{III}Re^{IV}(\mu\text{-}O)_2(Metpa)_2]^{3+}$ than that of $[Re^{IV}{}_2(\mu\text{-}O)_2(Metpa)_2]^{4+}$.

In this article, we theoretically studied $[Re^{III}Re^{IV}(\mu\text{-}O)_2(Metpa)_2]^{3+}$, $[Re^{IV}{}_2(\mu\text{-}O)_2(Metpa)_2]^{4+}$, and $[Re^{IV}{}_2(\mu\text{-}O)_2(Me_2tpa)_2]^{4+}$, using an ab initio multireference-based MRMP2 method and the B3LYP method[27,28] to clarify their electronic structures and bonding nature of the ground and some low-lying excited states. Because these complexes are too large to calculate real molecules by the MRMP2 method, we modeled them as $[Re^{IV}{}_2(\mu\text{-}O)_2(NH_3)_8]^{4+}$ (**1**; See Scheme 1) and $[Re^{III}Re^{IV}(\mu\text{-}O)_2(NH_3)_8]^{3+}$ (**2**), by replacing Metpa and Me_2tpa with eight NH_3 ligands.

Scheme 1.

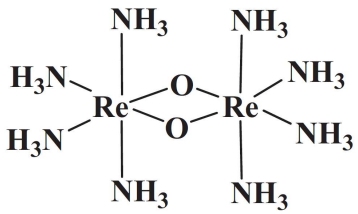

2.2. Computational Methods

For hydrogen, nitrogen, and oxygen atoms, Dunning's cc-pVDZ basis sets[21] were used. In rhenium atom, the Kr core, 4d, and 4f electrons were replaced with effective core potentials, whereas the 5s, 5p, and valence electrons were represented by (5s6p3d/3s3p2d) Gaussian basis set.[22]

In **1**, the geometries of singlet to septet states were optimized by the B3LYP method. As this complex has a lot of low-lying excited states, the MRMP2 method was employed here, which state-specific CASSCF wavefunctions were used as reference functions. The σ, σ^*, π, π^*, δ, and δ^* orbitals involving six electrons were taken as active space in the CASSCF calculations, where these orbitals mainly consist of $5d_{x^2-y^2}$, $5d_{yz}$, and $5d_{xz}$ orbitals of each rhenium center (see Scheme 1 for coordinate system). In the MRMP2 calculations, the CASSCF active space was employed as the reference space, whereas the N 1s and O 1s orbitals were always kept to be doubly occupied. The transition energies of low-lying excited states up to about 3.0 eV were calculated by the state-averaged CASSCF (SA-CASSCF) and MRMP2 methods, in which five state-averaged CASSCF wavefunctions for each irreducible representation were taken as reference functions. Oscillator strengths were estimated with the SA-CASSCF wavefunctions. In **2**, geometries of doublet to sextet states were optimized by the B3LYP method. The transition energies of low-lying excited states were evaluated by the SA-CASSCF and MRMP2 methods, in which nine state-averaged CASSCF wavefunctions were taken as reference functions for each irreducible representation. The time-dependent (TD) B3LYP method was also used to evaluate transition energies and oscillator strengths.

The B3LYP and CASSCF calculations were carried out with the Gaussian 03[23] and GAMESS[24] packages, respectively. The MRMP2 calculations were performed with the MR2D[25] program implemented in the GAMESS package. To draw the 3D plots of molecular orbitals, the MOLEKEL (ver. 4.3) program package[26] was used.

2.3. Results and Discussion

2.3.1. Optimized Geometries and Electron Configurations for Each Spin Multiplicity

Optimized geometries of **1** and **2** have C_2 symmetry in all spin multiplicities. Table 1 shows selected bond lengths and bond angles optimized for all spin multiplicities of these two complexes. The Re–Re bond length of **1** is 2.379, 2.570, 2.617, and 3.066 Å for the ^{1}A, ^{3}B, ^{5}A, and ^{7}B states, respectively. As the spin multiplicity increases, the Re–Re bond length becomes longer due to the occupation of antibonding orbitals. As shown in Figure 1, the molecular orbitals of the ^{1}A state calculated by the B3LYP method rise in energy in the order $\sigma < \delta^* < \pi < \pi^* < \delta < \sigma^*$, which is different from the order $\sigma < \pi < \delta < \delta^* < \pi^* < \sigma^*$, expected usually and proposed experimentally.[10] As a result, the σ, δ^*, and π orbitals are doubly occupied and the π^*, δ, and σ^* orbitals are unoccupied in the ^{1}A state against our expectation and experimental proposal. It is interesting to clarify the reason that the π and δ

Table 1. Bond lengths (in Å) and bond angles (in degree) of $[Re^{IV}_2(\mu\text{-}O)_2(NH_3)_8]^{4+}$ (**1**) and $[Re^{III}Re^{IV}(\mu\text{-}O)_2(NH_3)_8]^{3+}$ (**2**) optimized by the B3LYP method.

	$[Re^{IV}_2(\mu\text{-}O)_2(NH_3)_8]^{4+}$ (**1**)				$[Re^{III}Re^{IV}(\mu\text{-}O)_2(NH_3)_8]^{3+}$ (**2**)		
	^{1}A	^{3}B	^{5}A	^{7}B	^{2}B	^{4}A	^{6}B
r(Re–Re)	2.379	2.570	2.617	3.066	2.461	2.569	3.023
r(Re–O)	1.951	1.948	1.993, 1.963	1.980	1.963	1.955, 2.016	1.977
r(Re–N_1)	2.269	2.251	2.246	2.268	2.269	2.249	2.274
r(Re–N_2)	2.269	2.251	2.257	2.268	2.269	2.270	2.274
r(Re–N_3)	2.203	2.221	2.220	2.207	2.224	2.220	2.218
r(Re–N_4)	2.203	2.221	2.216	2.208	2.224	2.227	2.218
a(Re–O–Re)	75.1	82.6	82.8	101.5	77.6	80.6	99.7
a(Re–Re–N_1)	135.1	135.6	134.6	132.9	135.0	136.0	131.3
a(Re–Re–N_2)	135.1	135.6	136.2	132.9	135.0	133.8	131.3
a(Re–Re–N_3)	100.2	98.1	96.3	95.5	96.1	96.3	94.2
a(Re–Re–N_4)	100.2	98.1	98.8	95.5	96.1	96.3	94.2

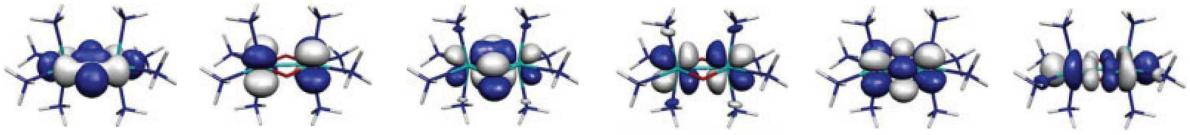

Figure 1. The σ, δ*, π, π*, δ, and σ* molecular orbitals and orbital energies (in eV) of $[Re^{IV}_2(\mu\text{-}O)_2(NH_3)_8]^{4+}$ (**1**) calculated by the B3LYP method.

orbitals are calculated to be at higher energy than the δ* orbitals. This unexpected order of orbital energies are easily interpreted in terms of the Re–O interaction, as follows: As the d_π–d_π and d_δ–d_δ bonding orbitals of **1** form strongly antibonding interactions with doubly occupied p orbitals of O atoms, these orbitals are pushed up in energy by these antibonding interactions. Actually, these antibonding interactions are clearly observed in the 61st and 63rd orbitals (see Figure 1). Although the d_δ–d_δ antibonding orbital does not involve antibonding overlap with the doubly occupied p orbitals of O atoms is involved; in other words, the δ* orbital is essentially the same as nonbonding d orbital. Therefore, it is at lower energy than δ, π, and π* orbitals, and the orbital order calculated by the B3LYP method is reasonable. Also, the ^{3}B, ^{5}A, and ^{7}B states mainly consist of $\sigma^2\delta^{*2}\pi^1\pi^{*1}$, $\sigma^2\delta^{*1}\pi^1\pi^{*1}\delta^1$, and $\sigma^1\delta^{*1}\pi^1\pi^{*1}\delta^1\sigma^{*1}$ configurations, respectively, where those occupations are consistent with the order of orbital energies in the ^{1}A state.

The Re–Re bond length of **2** was optimized by the B3LYP method to be 2.461, 2.569, and 3.023 Å in the ^{2}B, ^{4}A, and ^{6}B states, respectively. It is noted that the Re–Re distance of **2** in the ^{2}B state is considerably longer than that of **1** in the ^{1}A state as reported experimentally, while the Re–Re distances of **2** in the other ^{4}A and ^{6}B states are little different from those of **1** in the ^{3}B and ^{7}B states, respectively. These results suggest that the ground state is the ^{2}B state, as will be discussed later in more detail. This difference in bond length between **1** in the ^{1}A state and **2** in the ^{2}B state is easily interpreted in terms of

electron configuration, as follows: Complex **2** takes $\sigma^2\delta^{*2}\pi^2\pi^{*1}$ electron configuration in the ^{2}B state. Because **2** has one more d electron than does **1**, the π^* orbital becomes halfoccupied in **2** with the ^{2}B state, but it is unoccupied in **1** with the ^{1}A state. As a result, the Re–Re bond is weaker in **2** with the ^{2}B state than in **1** with the ^{1}A state.

2.3.2. Relative Energies of Each Spin Multiplicity and Electronic State of Ground State

Relative energies were estimated by the B3LYP, CASSCF, and MRMP2 methods, as shown in Table 2. The electronic states become higher in energy in the order ^{7}B < ^{3}B < ^{5}A < ^{1}A in **1** and in the order ^{6}B < ^{2}B < ^{4}A in **2**, and the ^{7}B and ^{6}B states were calculated to be the most stable in **1** and **2**, respectively, by the B3LYP method. The CASSCF method presents the same order as that of the B3LYP method. In the MRMP2 calculations, however, the low spin state is the most stable, and these electronic states become in the order ^{1}A < ^{3}B < ^{7}B < ^{5}A in **1** and in the order ^{2}B < ^{6}B < ^{4}A in **2**. As shown in Table 3, the decreasing order of the natural orbital occupation by the CASSCF method is almost the same

Table 2. Relative energies (in eV) of $[Re^{IV}(\mu\text{-}O)_2(NH_3)_8]^{4+}$ (**1**) and $[Re^{III}Re^{IV}(\mu\text{-}O)_2(NH_3)_8]^{3+}$ (**2**) calculated by the B3LYP, CASSCF, and MRMP2 methods, relative to the ^{1}A and ^{2}B state, respectively.

		^{1}A	^{3}B	^{5}A	^{7}B
$[Re^{IV}(\mu\text{-}O)_2(NH_3)_8]^{4+}$ (**1**)	B3LYP	0.00	–0.16	–0.14	–0.78
	CASSCF	0.00	–0.50	–0.24	–2.36
	MRMP2	0.00	0.42	0.88	0.87

		^{2}B	^{4}A	^{6}B
$[Re^{III}Re^{IV}(\mu\text{-}O)_2(NH_3)_8]^{3+}$ (**2**)	B3LYP	0.00	0.04	–0.20
	CASSCF	0.00	0.37	–1.19
	MRMP2	0.00	0.93	0.42

Table 3. Natural orbital populations of $[Re^{IV}_2(\mu\text{-}O)_2(NH_3)_8]^{4+}$ (**1**) and $[Re^{III}Re^{IV}(\mu\text{-}O)_2(NH_3)_8]^{3+}$ (**2**) calculated by the CASSCF method.

		σ	δ*	π	π*	δ	σ*
$[Re^{IV}_2(\mu\text{-}O)_2(NH_3)_8]^{4+}$ (**1**)	^{1}A	1.86	1.59	1.66	0.34	0.41	0.14
	^{3}B	1.67	1.33	1.06	0.94	0.67	0.33
	^{5}A	1.63	1.02	1.00	1.00	0.98	0.37
	^{7}B	1.00	1.00	1.00	1.00	1.00	1.00
$[Re^{III}Re^{IV}(\mu\text{-}O)_2(NH_3)_8]^{3+}$ (**2**)	^{2}B	1.86	0.35	1.90	1.10	1.65	0.14
	^{4}A	1.84	0.99	1.92	1.08	1.01	0.17
	^{6}B	1.00	1.00	1.00	1.00	2.00	1.00

as the increasing order of Kohn−Sham orbital calculated by the B3LYP method in each state. It is noted that the natural orbital populations considerably differ from the usual values for unoccupied, half-occupied, and doubly occupied orbitals; for instance, the occupation numbers of the δ* and π natural orbitals are not 2.0 but about 1.6 in the ^{1}A state. Thus, the multireference-based methods such as the MRMP2 and CASPT2 methods must be applied to these complexes. From these results, it is concluded that the ^{1}A and ^{2}B states are the ground states of **1** and **2**, respectively, which will be discussed later based on a different support.

2.3.3. Comparison between Experimental and Optimized Geometries

The optimized Re−Re and Re−O bond lengths are 2.379 and 1.951 Å, respectively, in **1** with the ^{1}A state, as shown in Table 1. These values are in good agreement with experimental values, *r*(Re−Re) = 2.368 Å and *r*(Re−O) = 1.952 and 1.932 Å for $[Re^{IV}_2(\mu\text{-}O)_2(Metpa)_2]^{4+}$ and *r*(Re−Re) = 2.383 Å and *r*(Re−O) = 1.946 and 1.915 Å for

$[Re^{IV}_2(\mu\text{-}O)_2(Me_2tpa)_2]^{4+}$. In the other ^3B, ^5A, and ^7B state these optimized geometrical parameters considerably differ from the experimental values. For instance, the experimental Re–Re distance is much shorter than the Re–Re distances optimized in these states; it is 2.570 Å in the ^3B state and 2.617 Å in the ^5A state. In **2** with the ^2B state, the optimized Re–Re and Re–O bond distances are 2.461 and 1.963 Å, respectively. These values are in good agreement with experimental values, *r*(Re–Re) = 2.426 Å and *r*(Re–O) = 1.965 and 1.934 Å for $[Re^{III}Re^{IV}(\mu\text{-}O)_2(Metpa)_2]^{3+}$. The good agreement of the optimized Re–Re distance in the ^2B state provides reliable support that the ground state of **2** is the ^2B state, which is consistent with the computational results by the MRMP2 method.

The longer Re–Re bond length of $[Re^{III}Re^{IV}(\mu\text{-}O)_2(Metpa)_2]^{3+}$ than those of $[Re^{IV}_2(\mu\text{-}O)_2(Metpa)_2]^{4+}$ and $[Re^{IV}_2(\mu\text{-}O)_2(Me_2tpa)_2]^{4+}$ was experimentally interpreted in terms of the occupation of the δ* orbital in the former complex. Although the B3LYP-calculated electron configuration ($\sigma^2\delta^{*2}\pi^2\pi^{*1}$) of the ^2B state is different from the experimentally proposed one ($\sigma^2\pi^2\delta^2\delta^{*1}$), the present electron configuration provides reasonable explanation of the longer Re–Re distance in **2** with the ^2B state as follows: Because the antibonding π* orbital becomes singly occupied on going from **1** with the ^1A state to **2** with the ^2B state, the Re–Re bond length is longer in **2** with the ^2B state than **1** with the ^1A state.

2.3.4. Various Low-Lying Excites States in Geometries of Singlet to Septet States

Figure 2 shows the MRMP2-calculated relative energies of the ^1A, ^1B, ^3A, ^3B, ^5A, ^5B, and ^7B states with geometries optimized for each spin multiplicity by the B3LYP method. The ^1A, ^3B, and ^5A states are considerably more stable than the ^1B, ^3A, and ^5B states in all the geometries of singlet to septet states. Although the ^1A and ^3B states are most stable in the optimized geometries of singlet and triplet states, respectively, the ^5A and ^7B states become considerably stable at the septet-optimized geometry. These results show that

B3LYP-optimized geometries are expected to be similar to MRMP2-optimized geometries and the optimization by the B3LYP method is reasonable. Figure 3 shows occupation numbers of σ, π, δ, δ*, π*, and σ* natural orbitals of ^{1}A, ^{3}B, ^{5}A, and ^{7}B states with geometries optimized for each spin multiplicity. As the occupation numbers of the σ bonding orbital in the ^{1}A, ^{3}B, and ^{5}A states considerably diminish between quintet and septet geometries, the σ bonding interaction does not exist at the septet geometry, r(Re–Re) = 3.066 Å. Also, the occupation numbers of the π bonding orbital in the ^{1}A and ^{3}B states considerably diminish between singlet and triplet geometries. Therefore, the π bonding interaction does not exist in the triplet geometry, *r*(Re–Re) = 2.570 Å. As the occupation numbers of these orbitals are almost 1.0 in all states taking the geometry, *r*(Re–Re) = 3.066 Å, no metal–metal bonding interaction exists in this geometry. Also, the occupation numbers are almost 1.0 in the ^{7}B state, indicating that all these orbitals are singly occupied; in the other words, the Re–Re bonding interaction does not exist at all in this state.

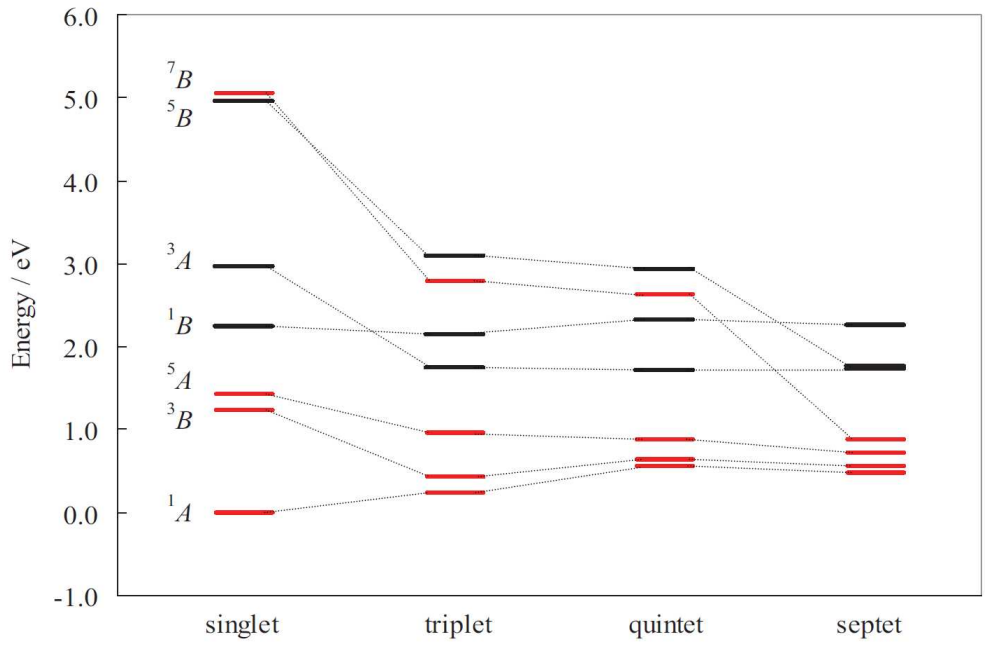

Figure 2. Relative energies (in eV) of ground and low-lying excited states for $[Re^{IV}_2(\mu\text{-}O)_2(NH_3)_8]^{4+}$ (**1**) calculated by the MRMP2 method. Geometries were optimized with the B3LYP method for each spin multiplicity.

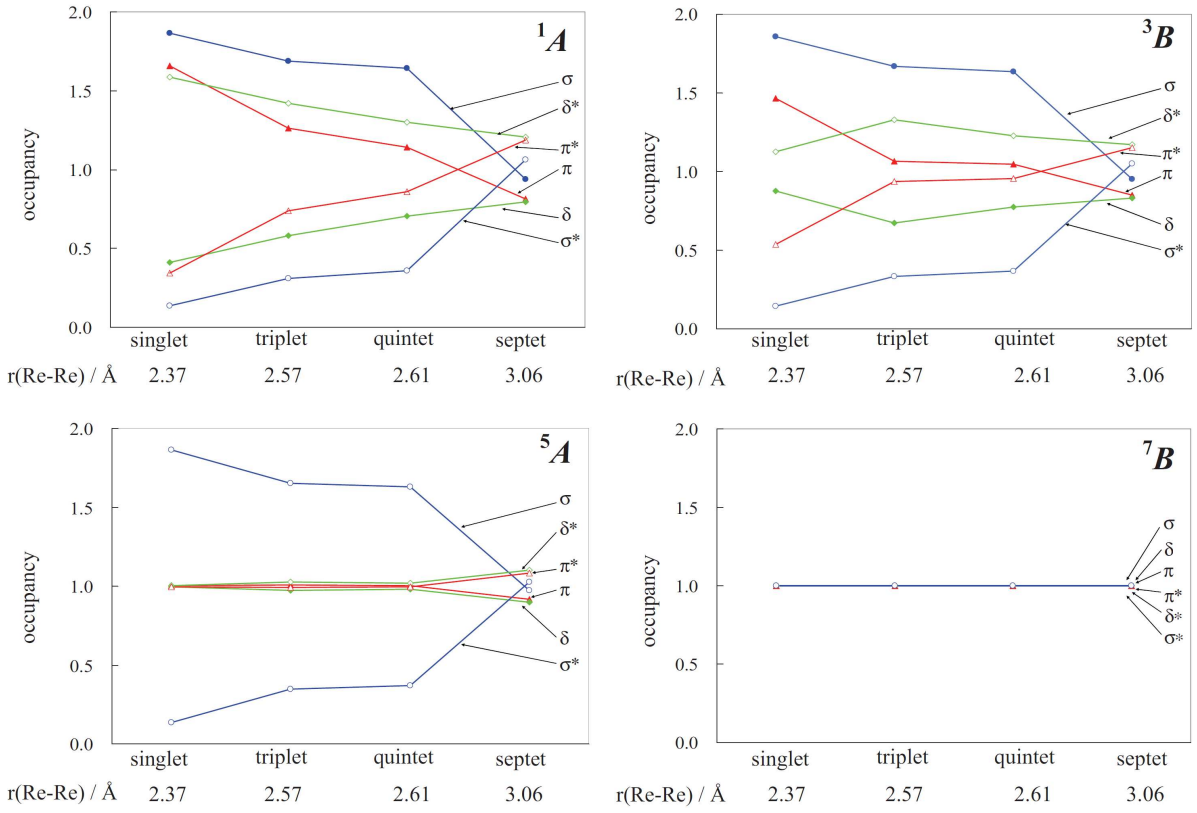

Figure 3. Occupation numbers of natural orbital for $[Re^{IV}_2(\mu\text{-}O)_2(NH_3)_8]^{4+}$ (**1**) estimated by the CASSCF method. The *r*(Re–Re) distances at the singlet (^{1}A), triplet (^{3}B), quintet (^{5}A), septet (^{7}B) states are 2.379, 2.570, 2.617, and 3.066 Å, respectively.

2.3.5. Excitation Energies and Oscillator Strengths

$[Re^{IV}_2(\mu\text{-}O)_2(tpa)_2]^{4+}$, $[Re^{IV}_2(\mu\text{-}O)_2(Metpa)_2]^{4+}$, and $[Re^{IV}_2(\mu\text{-}O)_2(Me_2tpa)_2]^{4+}$ exhibit two strong absorption bands at 2.19, 2.13, and 2.13 eV, respectively, and at 2.60, 2.57, and 2.56 eV, respectively as shown in Table 4. The molar extinction coefficient of the second band is about four times as large as that of the first one. The SA-CASSCF method was employed to determine the wavefunctions of excited states, in which five states and nine states were employed for each irreducible representation in **1** and **2**, respectively. In **1**, the first excitation is calculated at 2.49 eV by the CASSCF method and 2.12 eV by the MRMP2 method. The second excitation is calculated at 2.37 eV by the CASSCF method and 2.59 eV by the MRMP2 method. The oscillator strengths of the first and the second excitations

Table 4. Excitation energies (in eV) and oscillator strengths of $[Re^{IV}_2(\mu\text{-}O)_2(NH_3)_8]^{4+}$ (**1**) and $[Re^{III}Re^{IV}_2(\mu\text{-}O)_2(NH_3)_8]^{3+}$ (**2**) calculated by the MRMP2 ,method, relative to the ground state ^{1}A and ^{2}B, respectively.

	CASSCF	MRMP2	*f*	transition	expt[a]	
$[Re^{IV}_2(\mu\text{-}O)_2(NH_3)_8]^{4+}$						
1^1B	2.49	2.12	0.002860	$\delta^* \rightarrow \pi^*$	2.19 (2400),[b] 2.13 (1800)[d]	2.13 (2100),[c]
2^1B	3.37	2.59	0.000176	$\pi \rightarrow \pi^*$, $\delta^* \rightarrow \delta$	2.60 (9200),[b] 2.56 (8700)[d]	2.57 (11200),[c]
1^1A	2.99	3.08	0.000000	$\pi\delta^* \rightarrow \pi^*\delta$		
3^1B	3.91	3.11	0.010271	$\pi \rightarrow \delta$		
4^1B	4.04	3.27	0.002902	$\sigma \rightarrow \pi^*$		
5^1B	4.17	3.55	0.000101	$\sigma \rightarrow \delta$		
$[Re^{III}Re^{IV}(\mu\text{-}O)_2(NH_3)_8]^{3+}$						
1^2B	0.48	0.52	0.000003	$\pi^* \rightarrow \delta$		
1^2A	0.94	0.91	0.006461	$\pi^* \rightarrow \delta$, $\pi \rightarrow \pi^*$		
2^2A	1.46	1.31	0.001773	$\delta^*\pi^* \rightarrow \delta^2$, $\pi \rightarrow \delta$	1.38 (2000),[e] 1.30 (1100)[g]	1.34 (2100),[f]
3^2A	1.76	1.39	0.000389	$\delta^* \rightarrow \pi^*$		
4^2A	1.85	1.66	0.002284	$\pi \rightarrow \pi^*$, $\delta^* \rightarrow \delta$	1.85 (4700)[f]	
2^2B	2.02	1.97	0.000027	$\pi^* \rightarrow \sigma^*$		
5^2A	2.43	2.39	0.001541	$\delta^*\pi^* \rightarrow \delta^2$, $\pi \rightarrow \delta$	2.17 (11900),[e] 2.23 (7200)[g]	2.18 (11500),[f]
6^2A	2.78	2.65	0.000097	$\sigma \rightarrow \pi^*$		
7^2A	2.77	2.66	0.012656	$\pi\pi^* \rightarrow \delta^2$	2.60 (8700),[e]	2.60 (8300)[f]
3^2B	2.96	2.79	0.000000	$\delta^{*2} \rightarrow \pi^*\delta$		
8^2A	2.89	2.87	0.000005	$\delta^*\pi^* \rightarrow \delta\sigma^*$, $\pi \rightarrow \sigma^*$		

(a) In parentheses are molar extinction coefficients (in $dm^3mol^{-1}cm^{-1}$). (b) $[Re^{IV}_2(\mu\text{-}O)_2(tpa)_2]^{4+}$ in ref 9. (c) $[Re^{IV}_2(\mu\text{-}O)_2(Metpa)_2]^{4+}$ in ref 9. (d) $[Re^{IV}_2(\mu\text{-}O)_2(Me_2tpa)_2]^{4+}$ in ref 9. (e) $[Re^{III}Re^{IV}(\mu\text{-}O)_2(tpa)_2]^{3+}$ in ref 9. (f) $[Re^{III}Re^{IV}(\mu\text{-}O)_2(Metpa)_2]^{3+}$ in ref 9. (g) $[Re^{III}Re^{IV}(\mu\text{-}O)_2(Me_2tpa)_2]^{3+}$ in ref 9.

are calculated to be 0.002860 and 0.000176 at the SA-CASSCF level. The MRMP2-evaluated excitation energies agree well with the experimental values and the CASSCF-calculated excitation energies moderately agree with the experimental values, whereas oscillator strengths are somewhat different from the experimental values. Thus, the first excitation is assigned as 1^1B state, which mainly consists of the $\delta^* \rightarrow \pi^*$ excitation. The second excitation is assigned as 2^1B state, which mainly consists of the $\pi \rightarrow \pi^*$ and $\delta^* \rightarrow \delta$ excitations.

Also, the TD-B3LYP method was applied to evaluate the transition energies of **1**. The excitation energies to the 1^1B and 2^1B states were calculated to be 1.91 and 2.57 eV, respectively. Oscillator strengths were 0.0019 and 0.0343, respectively. Although these two states estimated by the TD-B3LYP method are not the first and second excited states but the third ($\pi \rightarrow \delta$ and $\delta^* \rightarrow \pi^*$) and the fifth ($\delta^* \rightarrow \delta$) ones; the first ($\delta^* \rightarrow \pi^*$), the second ($\pi \rightarrow \pi^*$), and the fourth ($\pi \rightarrow \sigma^*$) excited states which are calculated at 1.09, 1.32, and 2.54 eV, respectively, have negligible small oscillator strengths. Thus, the TD-B3LYP calculated excitation energies in **1** agree well with the experimental results.

$[Re^{III}Re^{IV}(\mu\text{-}O)_2(tpa)_2]^{3+}$, $[Re^{III}Re^{IV}(\mu\text{-}O)_2(Metpa)_2]^{3+}$, and $[Re^{III}Re^{IV}(\mu\text{-}O)_2(Me_2tpa)_2]^{3+}$ exhibit a lot of absorption bands, whereas $[Re^{IV}{}_2(\mu\text{-}O)_2(tpa)_2]^{4+}$, $[Re^{IV}{}_2(\mu\text{-}O)_2(Metpa)_2]^{4+}$, and $[Re^{IV}{}_2(\mu\text{-}O)_2(Me_2tpa)_2]^{4+}$ which exhibit two strong ones. For example, two weak absorption bands are observed at 1.34 and 1.85 eV, and two strong bands are observed at 2.18 and 2.60 eV in $[Re^{III}Re^{IV}(\mu\text{-}O)_2(Metpa)_2]^{3+}$. In **2**, the excitation energies with large oscillator strengths are calculated to be 0.91, 1.31, 1.66, 2.39, and 2.66 eV by the MRMP2 method and assigned as the 1^2A, 2^2A, 4^2A, 5^2A, and 7^2A states, respectively. Two weak absorption bands are the 2^2Aand 4^2Astates and two strong bands are the 5^2Aand 7^2A states. Excitation energies and oscillator strengths agree well with experimental values except for the oscillator strength of the $^2B \rightarrow 5^2A$ excitation. Both the $^2B \rightarrow 2^2A$ and $^2B \rightarrow 5^2A$ excitations mainly consists of the $\delta^*\pi^* \rightarrow \delta^2$ and $\pi \rightarrow \delta$ excitations

and the $^2B \rightarrow 4^2A$ excitation mainly consists of the $\pi \rightarrow \pi^*$ and $\delta^* \rightarrow \delta$ excitations. The $^2B \rightarrow 7^2A$ excitation mainly consists of the $\pi\pi^* \rightarrow \delta^2$ excitation. In other words, δ^*, π, π^*, and δ orbitals participate in these absorptions.

In the TD-B3LYP calculations, the excited state with the largest oscillator strength is the ^2B state. The excitation energy of 2.40 eV agrees well with the experimental values. However, the assignments are different between the MRMP2 and TD-B3LYP calculations; all the excited states with large oscillator strength by the SA-CASSCF method are belonging to the ^2A states. Although the TD-B3LYPcalculated excitation energies in **1** agree well with the experimental values, the TD-B3LYP-calculated results in **2** do not agree with the experimental values. As much more low-lying excited states exist in **2** than in **1**, the multiconfigurational nature of wavefunction is very strong in the excited state of **2**.

2.4. Conclusions

We theoretically studied $[Re^{IV}_2(\mu\text{-}O)_2(NH_3)_8]^{4+}$ (**1**) and $[Re^{III}Re^{IV}(\mu\text{-}O)_2(NH_3)_8]^{3+}$ (**2**), which are the model of $[Re^{III}Re^{IV}(\mu\text{-}O)_2(Metpa)_2]^{3+}$, $[Re^{IV}_2(\mu\text{-}O)_2(Metpa)_2]^{4+}$, and $[Re^{IV}_2(\mu\text{-}O)_2(Me_2tpa)_2]^{4+}$, using the MRMP2 and B3LYP method to clarify their electronic structures and bonding nature of the ground and some low-lying excited states. In the B3LYP calculations of the ^1A state of **1**, important molecular orbitals rise in energy in the order $\sigma < \delta^* < \pi < \pi^* < \delta < \sigma^*$, which is different from the order $\sigma < \pi < \delta < \delta^* < \pi^* < \sigma^*$, experimentally proposed. However, the computational results are reasonable, as follow: The π and δ bonding orbitals of **1** form antibonding interactions with doubly occupied p orbitals of O atoms but the δ^* antibonding orbital does not, the π and δ orbitals become higher in energy than the δ^* orbital.

The ground states of **1** and **2** were assigned to be the ^7B and ^6B states, respectively, by the B3LYP and CASSCF methods, but to be the ^1A and ^2B states, respectively, by the MRMP2 method. Although the B3LYP-optimized Re–Re distances of the ^7B and ^6B states

differ much from the experimental values of similar complexes such as $[Re^{IV}_2(\mu\text{-}O)_2(tpa)_2]^{4+}$, $[Re^{IV}_2(\mu\text{-}O)_2(Metpa)_2]^{4+}$, and $[Re^{IV}_2(\mu\text{-}O)_2(Me_2tpa)_2]^{4+}$, those of the ^1A and ^2B states are in good agreement with the experimental ones. These results indicate that the ground states are the ^1A and ^2B states, respectively, as evaluated by the MRMP2 method. Also, these three complexes exhibit two large absorption bands at about 2.1 and 2.6 eV, which are assigned to be the $^1A \rightarrow 1^1B$ and $^1A \rightarrow 2^1B$ excitations by the MRMP2 method. These excitation energies are calculated to be 2.12 and 2.59 eV by the MRMP2 method, which are in good agreement with the experimental values of three similar complexes. The $^1A \rightarrow 1^1B$ excitation mainly consists of the $\delta^* \rightarrow \pi^*$ excitation, and the $^1A \rightarrow 2^1B$ excitation consists of the $\pi \rightarrow \pi^*$ and $\delta^* \rightarrow \delta$ excitations. $[Re^{III}Re^{IV}(\mu\text{-}O)_2(Metpa)_2]^{3+}$ exhibits two strong absorptions at 2.18 and 2.59 eV and two weak ones at 1.34 and 1.85 eV, which are assigned to be the $^2B \rightarrow 5^2A$ and $^2B \rightarrow 7^2A$ excitations and the $^2B \rightarrow 2^2A$ and $^2B \rightarrow 4^2A$ excitations, respectively, by the MRMP2 method. The $^2B \rightarrow 2^2A$ and $^2B \rightarrow 5^2A$ excitations mainly consists of the $\delta^*\pi^* \rightarrow \delta^2$ and $\pi \rightarrow \delta$ excitations and the $^2B \rightarrow 4^2A$ excitation mainly consists of the $\pi \rightarrow \pi^*$ and $\delta^* \rightarrow \delta$ excitations. The $^2B \rightarrow 7^2A$ excitation mainly consists of the $\pi\pi^* \rightarrow \delta^2$ excitation.

References

(1) Cotton, F. A.; Diebold, M. P.; O'Connor, C. J.; Powell, G. L. *J. Am. Chem. Soc.* **1985**, *107*, 7438.

(2) Agaskar, P. A.; Cotton, F. A.; Dunbar, K. R.; Falvello, L. R.; O'Connor, C. *J. Inorg. Chem.* **1987**, *26*, 4051.

(3) Cotton, F. A.; Daniels, L. M.; Dunbar, K. R.; Falvello, L. R.; O'Connor, C. J.; Price, A. C. *Inorg. Chem.* **1991**, *30*, 2509.

(4) Cotton, F. A.; Eglin, J. L.; James, C. A.; Luck, R. L. *Inorg. Chem.* **1992**, *31*, 5308.

(5) Shaik, S.; Hoffmann, R.; Fisel, C. R.; Summerville, R. H. *J. Am. Chem. Soc.* **1980**, *102*, 4555.

(6) Cotton, F. A.; Eglin, J. L.; Hong, B.; James, C. A. *J. Am. Chem. Soc.* **1992**, *114*, 4915.

(7) Brgi, H. B.; Anderegg, G.; Bluenstein, P. *Inorg. Chem.* **1981**, *20*, 3829.

(8) Ikari, S.; Ito, T.; McFarlane, W.; Nasreldin, M.; Ooi, B.-L.; Sasaki, Y.; Sykes, A. G. *J. Chem. Soc. Dalton Trans.* **1993**, 2621.

(9) Sugimoto, H.; Kamei, M.; Umakoshi, K.; Sasaki, Y.; Suzuki, M. *Inorg. Chem.* **1996**, *35*, 7082.

(10) Umakoshi, K.; Misasa, N.; Ohtsu, C.; Kojima, T.; Sokolov, M.; Wakeshima, M.; Hinatsu, Y.; Onishi, M. *Angew. Chem. Int. Ed.* **2005**, *44*, 720.

(11) Böhm, G.; Wieghardt, K.; Nuber, B.; Weiss, J. *Inorg. Chem.* **1991**, *30*, 3464.

(12) (a) Siegbahn, P. E.; Heiberg, A.; Roos, B. O.; Levy, B. *Phys. Scr.* **1980**, *21*, 323. (b) Roos, B. O.; Taylor, P. R.; Siegbahn, P. E. *Chem. Phys.* **1980**, *48*, 157. (c) Roos, B. O. *Int. J. Quantum. Chem* **1980**, *S14*, 175.

(13) (a) Hirao, K. *Chem. Phys. Lett.* **1992**, *190*, 374. (b) Hirao, K. *Chem. Phys. Lett.* **1992**, *196*, 397. (c) Hirao, K. *Chem. Phys. Lett.* **1993**, *201*, 59. (d) Hirao, K. *Int. J. Quantum. Chem.* **1992**, *S26*, 517.

(14) (a) Nakano, H. *J. Chem. Phys.* **1993**, *99*, 7983. (b) Nakano, H. *Chem. Phys. Lett.* **1993**, *207*, 372.

(15) (a) Nakano, H.; Tsuneda, T.; Hashimoto, T.; Hirao, K. *J. Chem. Phys.* **1996**, *104*, 2312. (b) Hashimoto, T.; Nakano, H.; Hirao, K. *J. Chem. Phys.* **1996**, *104*, 6244. (c) Kawashima, Y.; Nakayama, K.; Nakano, H.; Hirao, K. *Chem. Phys. Lett.* **1997**, *267*, 82. (d) Nakano, H.; Nakayama, K.; Hirao, K.; Dupuis, M. *J. Chem. Phys.* **1997**, *106*, 4912. (e) Hashimoto, T.; Nakano, H.; Hirao, K. *J. Mol. Struct. (Theochem)* **1998**, *451*, 25. (f) Nakayama, K.; Nakano, H.; Hirao, K. *Int. J. Quantum. Chem.* **1997**, *66*, 157. (g) Kawashima, Y.; Hashimoto, T.; Nakano, H.; Hirao, K. *Theoret. Chem. Acc.* **1999**, *102*, 49. (h) Kurashige, Y.; Nakano, H.; Nakao, Y.; Hirao, K. *Chem. Phys. Lett.* **2004**, *400*, 425.

(16) (a) Choe, Y.-K.; Hashimoto, T.; Nakano, H.; Hirao, K. *Chem. Phys. Lett.* **1998**, *295*, 380. (b) Hashimoto, T.; Choe, Y.-K.; Nakano, H.; Hirao, K. *J. Phys. Chem. A* **1999**, *103*, 1894. (c) Choe, Y.-K.; Nakajima, T.; Hirao, K.; Lindh, R. *J. Chem. Phys.* **1999**, *111*, 3837.

(17) (a) Nakao, Y.; Taketsugu, T.; Hirao, K. *J. Chem. Phys.* **1999**, *110*, 10863. (b) Nakao, Y.; Hirao, K.; Taketsugu, T. *J. Chem. Phys.* **2001**, *114*, 5216. (c) Nakao, Y.; Hirao, K.; Taketsugu, T. *J. Chem. Phys.* **2001**, *114*, 7935.

(18) (a) McGrady, J. E.; Stranger, R.; Lovell, T. *J. Phys. Chem. A* **1997**, *101*, 6265. (b) McGrady, J. E.; Lovell, T.; Stranger, R. *Inorg. Chem.* **1997**, *36*, 3242. (c) McGrady, J. E.; Stranger, R.; Lovell, T. *Inorg. Chem.* **1998**, *37*, 3802. (d) Stranger, R.; Lovell, T.; McGrady, J. E. *Inorg. Chem.* **1999**, *38*, 5510. (e) Stranger, R.; Turner, A.; Delfs, C. D. *Inorg. Chem.* **2001**, *40*, 4093. (f) Cavigliasso, G.; Stranger, R. *Inorg. Chem.* **2004**, *43*, 2368. (g) Cavigliasso, G.; Comba, P.; Stranger, R. *Inorg. Chem.* **2004**, *43*, 6734.

(19) Gagliardi, L.; Roos, B. O. *Inorg. Chem.* **2003**, *42*, 1599.

(20) Saito, K.; Nakao, Y.; Sato, H.; Sakaki, S. *J. Phys. Chem. A* **2006**, *110*, 9710.

(21) (a) Dunning, T. H., Jr. *J. Chem. Phys.* **1989**, *90*, 1007. (b) Woon, D. E.; Dunning, T. H., Jr. *J. Chem. Phys.* **1993**, *98*, 1358.

(22) Hay, P. J.; Wadt, W. R. *J. Chem. Phys.* **1985**, *82*, 299.

(23) Frisch, M. J.; Trucks, G. W.; Schlegel, H. B.; Scuseria, G. E.; Robb, M. A.; Cheeseman, J. R.; Montgomery, J. A., Jr.; Vreven, T.; Kudin, K. N.; Burant, J. C.; Millam, J. M.; Iyengar, S. S.; Tomasi, J.; Barone, V.; Mennucci, B.; Cossi, M.; Scalmani, G.; Rega, N.; Petersson, G. A.; Nakatsuji, H.; Hada, M.; Ehara, M.; Toyota, K.; Fukuda, R.; Hasegawa, J.; Ishida, M.; Nakajima, T.; Honda, Y.; Kitao, O.; Nakai, H.; Klene, M.; Li, X.; Knox, J. E.; Hratchian, H. P.; Cross, J. B.; Bakken, V.; Adamo, C.; Jaramillo, J.; Gomperts, R.; Stratmann, R. E.; Yazyev, O.; Austin, A. J.; Cammi, R.; Pomelli, C.; Ochterski, J. W.; Ayala, P. Y.; Morokuma, K.; Voth, G. A.; Salvador, P.; Dannenberg, J. J.; Zakrzewski, V. G.; Dapprich, S.; Daniels, A. D.; Strain, M. C.; Farkas, O.; Malick, D. K.; Rabuck, A. D.; Raghavachari, K.; Foresman, J. B.; Ortiz, J. V.; Cui, Q.; Baboul, A. G.; Clifford, S.; Cioslowski, J.; Stefanov, B. B.; Liu, G.; Liashenko, A.; Piskorz, P.; Komaromi, I.; Martin, R. L.; Fox, D. J.; Keith, T.; Al-Laham, M. A.; Peng, C. Y.; Nanayakkara, A.; Challacombe, M.; Gill, P. M. W.; Johnson, B.; Chen, W.; Wong, M. W.; Gonzalez, C.; Pople, J. A. *Gaussian 03*, revision C.02; Gaussian, Inc.: Wallingford, CT, 2004.

(24) Schmidt, M. W.; Baldridge, K. K.; Boatz, J. A.; Elbert, S. T.; Gordon, M. S.; Jensen, J. H.; Koseki, S.; Matsunaga, N.; Nguyen, K. A.; Su, S.; Windus, T. L.; Dupuis, M.; Montgomery, J. A. *J. Comput. Chem.* **1993**, *14*, 1347.

(25) Nakano, H. *MR2D*, version 2.0; University of Tokyo: Tokyo, Japan, 1995.

(26) (a) Flükiger, P.; Lüthi, H. P.; Portmann, S.; Weber, J. *MOLEKEL*, version 4.3; Scientific Computing, Manno, Switzerland, 2000−2002. (b) Portmann, S.; Lüthi, H. P. *CHIMIA* **2000**, *54*, 766.

(27) (a) Becke, A. D. *J. Chem. Phys.* **1992**, *96*, 2155. (b) Becke, A. D. *J. Chem. Phys.* **1993**, *98*, 5648.

(28) Lee, C.; Yang, W.; Parr, R. G. *Phys. Rev. B* **1988**, *37*, 785.

Chapter 3

Theoretical Study of Pyrazolate-Bridged Dinuclear Platinum(II) Complexes: Interesting Potential Energy Curve of the Lowest Energy Triplet Excited State and Phosphorescence Spectra

3.1. Introduction

Luminescence spectra of transition metal complexes have been investigated well so far in both fundamental chemistry and applied chemistry because luminescence spectra provide valuable knowledge of the excited state and also emissive compounds are useful as optical materials such as light-emitting devices, photochemical sensors, and biological labeling probes.[1–3] In particular, the 5d transition metal complexes such as iridium[2] and platinum complexes[2a,3–6] have drawn considerable interest because most of them exhibit strong phosphorescence spectra.

Recently, new characteristic phosphorescence spectra were reported in multinuclear platinum complexes.[1c,2a,3–5] Interestingly, those spectra are much different from those of mononuclear complexes. For instance, phosphorescence spectra of pyrazolate-bridged dinuclear platinum(II) complexes, $[Pt_2(\mu\text{-}R_2pz)_2(dfppy)_2]$ (dfppy = 2-(2,4-difluorophenyl)pyridine; R_2pz = pyrazolate in **1**, 3,5-dimethylpyrazolate in **2**, 3-methyl-5-*tert*-butylpyrazolate in **3**, and 3,5-bis(*tert*-butyl)pyrazolate in **4**; Scheme 1), which were reported by Thompson and his collaborators,[5] are interesting for the reasons that follow: (1) The energies of phosphorescence of **1** and **2** are almost the same in both polystyrene at room temperature (RT) and 2-methyltetrahydrofuran (2-MeTHF) at 77 K, while the energies of phosphorescence of **3** and **4** are moderately lower in the former solution than in the latter one. (2) The energy of phosphorescence of **3** is much lower in fluid 2-MeTHF at RT than in frozen 2-MeTHF at 77 K, while the energy of phosphorescence of **4** is moderately lower in the former solution than in the latter one. These interesting

features were discussed in terms of the geometries and the electronic structures of the singlet ground state (S_0) and the lowest energy triplet excited state (T_1).[5] Thus, it is worth theoretically investigating the geometries and the electronic structures of the ground and excited states of these complexes.

In this study, we theoretically investigated the pz-bridged dinuclear platinum(II) complexes **1**–**4**. Our purposes here are to present theoretical knowledge of the geometries, the electronic structures, and the potential energy curves (PECs) of the S_0 and T_1 states of these complexes and to clarify the reason why their phosphorescence spectra depend considerably on the substituents on pz and the measurement conditions.

Scheme 1.

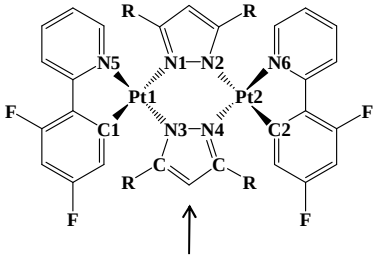

1 (R = H), **2** (R = Me), **4** (R = *t*-Bu)

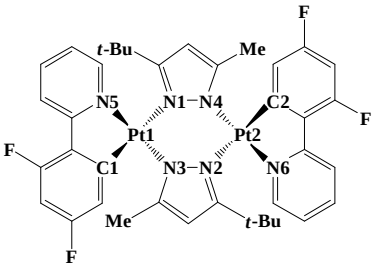

3

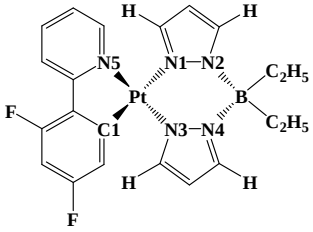

5

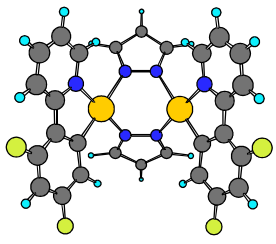

top view of **1**

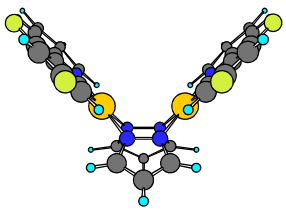

front view of **1**

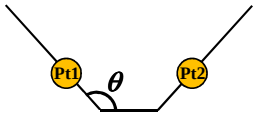

3.2. Computational Details

We employed two basis set systems (basis-I and II) in this study. In basis-I, core electrons (up to 4f) of Pt were replaced with the relativistic effective core potentials (ECPs) proposed by Hay and Wadt,[7] and its valence electrons were represented by (541/541/111/1) basis set.[8,9] The 6-31G* basis sets[10] were used for H, C, N, and F. In basis-II, valence electrons of Pt were represented by (5311/5311/111/1) basis set[8,9] with the same ECPs as those of basis-I. The cc-pVDZ basis sets[11] were used for H, C, N, and F.

The geometries of **1**–**5** were optimized by the DFT(B3PW91)/basis-I method[12,13] in both the S_0 and the T_1 states. We ascertained that each optimized geometry exhibited no imaginary frequency. The PECs of **1**–**4** were evaluated as a function of the Pt–Pt distance in the S_0 and T_1 states, where all geometrical parameters were optimized with the DFT(B3PW91)/basis-I method at each Pt–Pt distance. The energy of phosphorescence was defined as the energy difference between the S_0 and the T_1 states at either the T_1-global or the T_1-local minimum geometry. This energy difference was calculated by the DFT(B3PW91)/basis-II method.

The solvent effect of fluid 2-MeTHF was taken into consideration by the polarized continuum model (PCM),[14] where THF was employed as a model of 2-MeTHF as in previous theoretical study.[15] All calculations were performed with the Gaussian 03 (revision C.02) program package.[16] Molecular orbitals were drawn by the MOLEKEL (version 4.3) program.[17]

3.3. Results and Discussion

3.3.1. Geometry and Electronic Structure of the S_0 State

The optimized geometries of **1**–**4** in the S_0 state are named **1S$_0$**–**4S$_0$**, respectively, hereafter. As shown in Table 1 and Figure 1, the optimized geometrical parameters including the Pt–Pt distance of **1S$_0$**, **2S$_0$**, and **3S$_0$** agree well with those of the experimental

ones, while the optimized Pt–Pt distance of **4S$_0$** is moderately longer than that of the experimental one. The geometry of the Pt–dfppy moiety is almost the same in **1S$_0$**–**4S$_0$** (see Table 1 for the Pt1–N5 length, the N5–Pt1–C1 angle, etc.). Interestingly, the Pt–Pt distance becomes shorter in the order **1** > **2** > **3** > **4**, and the θ angle between the Pt–dfppy moiety and the N1–N2–N3–N4 plane decreases in the same order in both the experimental and the calculated geometries, where the N1, N2, N3, and N4 are on one plane[18] and the θ angle is defined in Scheme 1. These experimental results are explained in terms of the steric repulsion between dfppy and the substituents on pz, as follows: In **1S$_0$**, the H atoms on pz slightly push the dfppy plane away, leading to the large θ angle and the long Pt–Pt distance, as shown in Figure 1. In **2S$_0$**, the four methyl groups on pz moderately push the dfppy plane away to moderately decrease the Pt–Pt distance and the θ angle (see Figure A1 in Appendix). In **3S$_0$**, the two methyl and two *tert*-butyl groups considerably push the dfppy plane away to considerably decrease the Pt–Pt distance and the θ angle. In **4S$_0$**, the four *tert*-butyl groups on pz strongly push the dfppy plane away to greatly decrease the Pt–Pt distance and the θ angle.

The highest occupied molecular orbitals (HOMOs) of **1S$_0$**–**4S$_0$** mainly consist of the dσ–dσ antibonding overlap between two Pt nuclei, and their lowest unoccupied molecular orbitals (LUMOs) mainly consist of the π* orbital of dfppy, as shown in Figures 2 and S2 (Appendix). The HOMO is named the dσ*(Pt–Pt) orbital hereafter because the dσ orbital of one Pt atom overlaps with the dσ orbital of the other Pt atom in an antibonding way. The π orbital of dfppy is at moderately lower energy than the HOMO. As the Pt–Pt distance becomes shorter, the dσ–dσ antibonding overlap increases. As a result, the dσ*(Pt–Pt) orbital energy becomes higher with a decrease in the Pt–Pt distance, as clearly shown in Figure 3, in which the dσ*(Pt–Pt) orbital energies are plotted against the Pt–Pt distance. On the other hand, the π and π* orbital energies of dfppy (Figure 2) slightly depend on the Pt–Pt distance, as expected. In addition, these orbital energies are almost the same as those

of the mononuclear Pt(II) complex [Pt(μ-pz)$_2$(dfppy)B(C_2H_5)$_2$] (**5**), as shown in Table 1.

These features observed in the S_0 geometry, the HOMO, and the LUMO deeply relate to the phosphorescence spectra of those complexes, as will be discussed below.

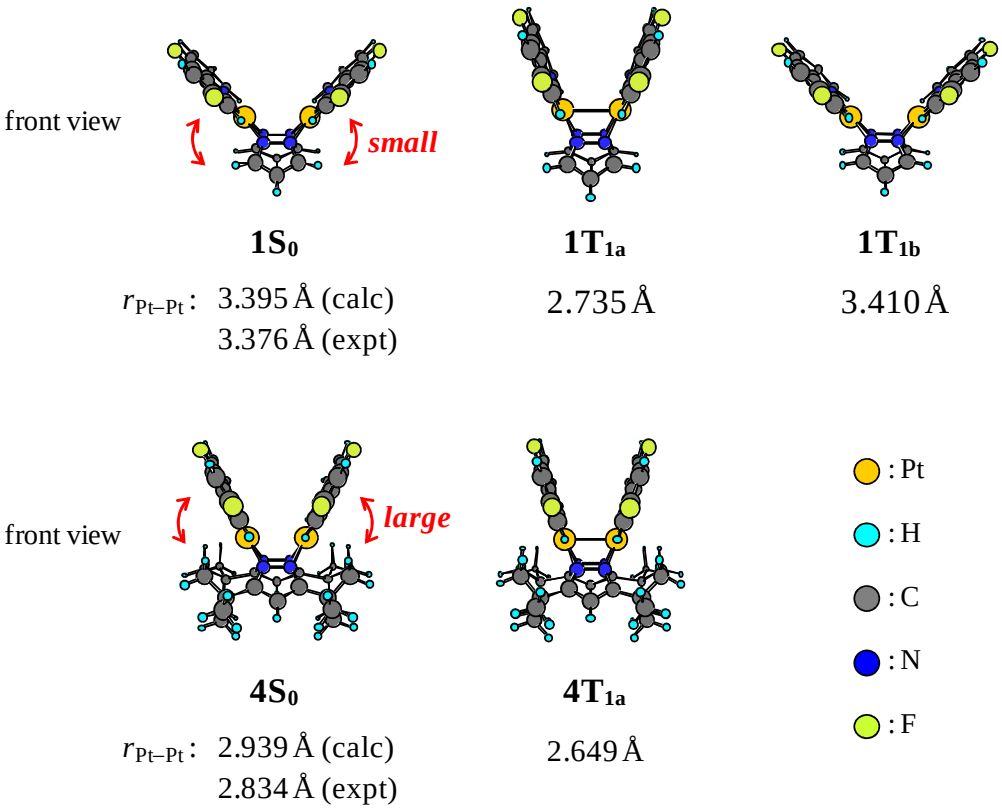

Figure 1. S_0- and T_1-optimized geometries of **1** and **4**. Red arrows schematically represent the steric repulsion between dfppy and substituents (H atoms in **1** and *tert*-butyl groups in **4**). Experimental Pt–Pt distances were reported in ref 5.

Table 1. Several important optimized bond lengths (in Å), bond angles (in degree), dihedral angles (in degree)[a] and energies of π*(dfppy), dσ*(Pt–Pt), and π(dfppy) orbitals (in eV)[b] of **1** to **5**

	1				**2**			
	expt[c]	**1S$_0$**	**1T$_{1a}$**	**1T$_{1b}$**	expt[c]	**2S$_0$**	**2T$_{1a}$**	**2T$_{1b}$**
r(Pt1–Pt2)	3.376	3.395	2.735	3.410	3.191	3.239	2.724	3.252
r(Pt1–N1)	2.082	2.117	2.140	2.119	2.057	2.124	2.138	2.124
r(Pt1–N3)	2.009	1.988	2.032	2.027	2.020	2.017	2.030	2.018
r(Pt1–N5)	2.013	2.027	2.010	1.996	2.007	2.028	2.014	2.027
r(Pt1–C1)	1.996	1.988	1.989	1.962	2.001	1.987	1.990	1.987
a(N1–Pt1–N3)	85.5	85.1	85.0	85.1	86.4	84.6	85.1	84.6
a(N5–Pt1–C1)	81.5	81.1	81.6	82.4	80.8	81.0	81.5	81.0
d(Pt1–N1–N3–N4)[d]	132.6	132.3	116.9	132.6	128.3	128.0	116.6	128.4
ε(π*(dfppy))		–2.04	–2.25	–2.24		–1.99	–2.18	–2.18
ε(dσ*(Pt–Pt))[e]		–5.85	–4.96	–5.93		–5.60	–4.85	–5.65
ε(π(dfppy))		–6.50	–6.23	–6.51		–6.45	–6.59	–6.52

	3			**4**			**5**		
	expt[c]	**3S$_0$**	**3T$_{1a}$**	expt[c]	**4S$_0$**	**4T$_{1a}$**	expt[c]	**5S$_0$**	**5T$_1$**
r(Pt1–Pt2)	3.046	3.044	2.686	2.834	2.939	2.649			
r(Pt1–N1)	2.096	2.155	2.167	2.121	2.161	2.166	2.074	2.118	2.118
r(Pt1–N3)	2.031	2.020	2.027	2.054	2.043	2.052	2.010	2.020	2.029
r(Pt1–N5)	2.004	2.031	2.023	2.015	2.029	2.017	2.006	2.028	1.998
r(Pt1–C1)	1.979	1.984	1.986	1.987	1.985	1.995	1.981	2.020	1.968
a(N1–Pt1–N3)	85.2	84.8	85.2	86.0	85.9	86.4	84.7	84.3	84.7
a(N5–Pt1–C1)	81.2	80.9	81.3	81.1	80.9	81.3	80.6	80.7	81.9
d(Pt1–N1–N3–N2)[d]	130.3	128.2	120.7						
d(Pt1–N1–N3–N4)[d]				118.4	120.7	114.8	140.9	144.8	145.9
ε(π*(dfppy))		–2.00	–2.16		–2.04	–2.25		–2.12	–2.37
ε(dσ*(Pt–Pt))[e]		–5.38	–4.81		–5.07	–4.58			
ε(π(dfppy))		–6.49	–6.48		–6.49	–6.34		–6.14	–5.99

(a) Geometries were optimized with the DFT(B3PW91)/basis-I method. (b) Orbital energies were calculated in the S_0 state with the DFT(B3PW91)/basis-II method, where the **S$_0$**-, **T$_{1a}$**-, and **T$_{1b}$**-optimized geometries were employed for the S_0, T_{1a}, and T_{1b} states, respectively. (c) Ref 5. Averaged values for C_s symmetry in **1**, **2**, and **4** and C_2 symmetry in **3**. For instance, *r*(Pt1–N1) in this table corresponds to the average value of *r*(Pt1–N1) and *r*(Pt2–N2) reported experimentally. (d) The dihedral angle corresponds to θ in Scheme 1. (e) The HOMO of the S_0 state.

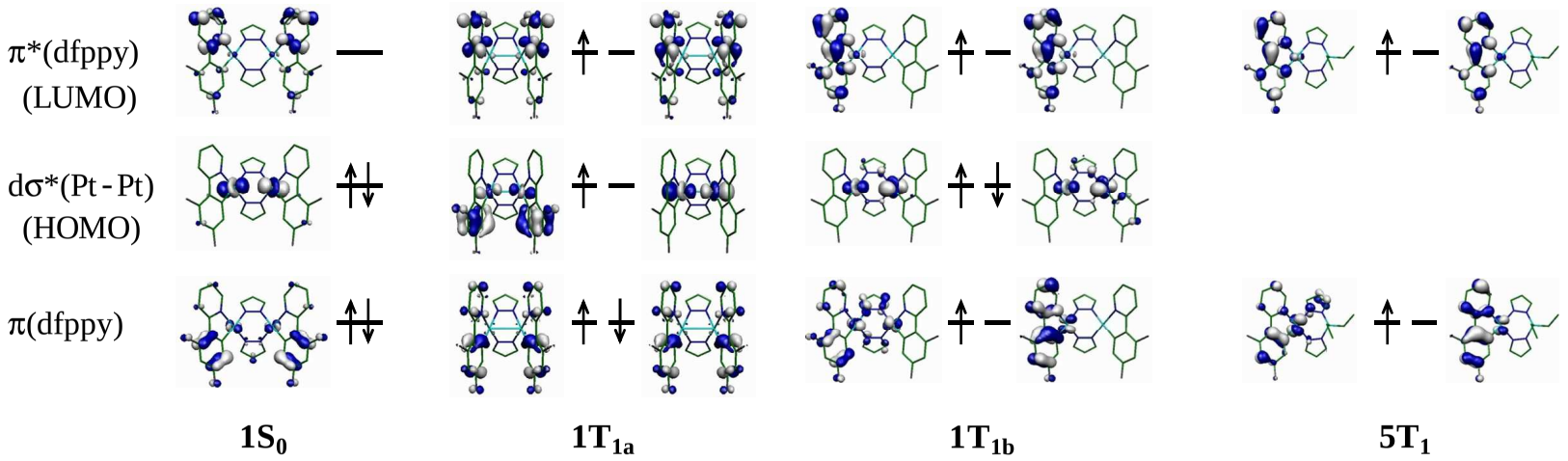

Figure 2. Several important molecular orbitals $\mathbf{1S_0}$, $\mathbf{1T_{1a}}$, $\mathbf{1T_{1b}}$, and $\mathbf{5T_1}$. H atoms are omitted brevity.

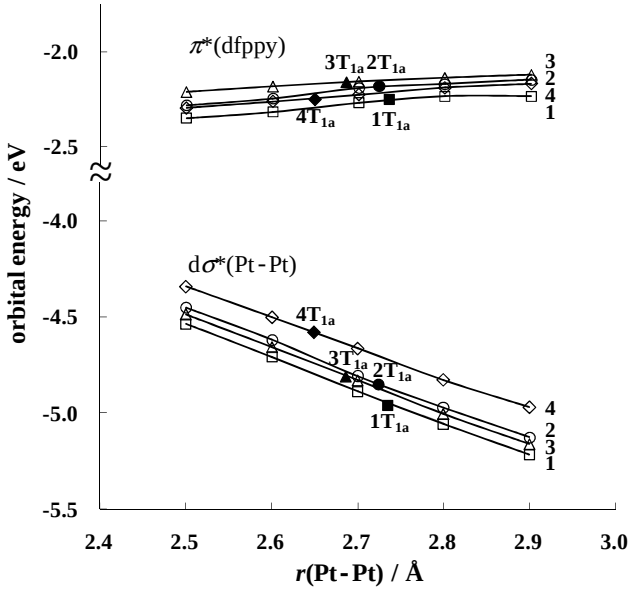

Figure 3. Energies of the dσ*(Pt–Pt) orbital (HOMO of the S_0 state) and the π*(dfppy) orbital (LUMO of the S_0 state) of **1** to **4** vs. the Pt–Pt distance. These orbital energies were calculated in the S_0 state with the DFT(B3PW91)/basis-II method. The geometries were optimized in the T_1 state at each Pt–Pt distance with the DFT(B3PW91)/basis-I method.

3.3.2. Geometry and Electronic Structure of the T_1 State

There are two possible lowest energy triplet excited states, as shown in Figure 2. In one (**$1T_{1a}$**), one-electron excitation occurs from the dσ*(Pt–Pt) orbital to the π* orbital of dfppy. In the other (**$1T_{1b}$**), one-electron excitation occurs from the π orbital to the π* orbital in dfppy. The former is named metal–metal-to-ligand charge transfer (MMLCT) excitation and the latter is the π–π* excitation. First, we optimized the geometry of the former excited state, which corresponds to the T_1-global minimum (**$1T_{1a}$**–**$4T_{1a}$**), as will be shown below. Its optimized geometrical parameters are presented in Table 1 and Figure 1 (see also Figure A1 in Appendix for the T_1-global minimum geometries of **2** and **3**). The Pt–Pt distance is much shorter and the θ angle is much smaller in all the T_1-global minimum geometries (**$1T_{1a}$**–**$4T_{1a}$**) than in all the S_0-equilibrium ones (**$1S_0$**–**$4S_0$**). This result is explained in terms of the dσ–dσ bonding interaction, as follows: In **$1S_0$**, this bonding

interaction is not formed at all because the antibonding dσ*(Pt–Pt) orbital is doubly occupied, as shown in Figure 2. In **$1T_{1a}$**, on the other hand, one-electron excitation occurs from the dσ*(Pt–Pt) orbital to the π* orbital of dfppy. As a result, the dσ*(Pt–Pt) orbital becomes singly occupied, which leads to the formation of the Pt–Pt bonding interaction and the decrease of the Pt–Pt distance in **$1T_{1a}$**. The difference (0.086 Å) in the Pt–Pt distance between **$1T_{1a}$** and **$4T_{1a}$** is much smaller than that (0.456 Å) between **$1S_0$** and **$4S_0$**. This result indicates that the T_1-global minimum geometry depends less on the substituents on pz than does the S_0-equilibrium one. This is because the Pt–Pt bonding interaction in addition to the substituents on pz plays important roles to determine the Pt–Pt distance of the T_1-global minimum but only the substituents on pz play important roles to determine the Pt–Pt distance in the S_0 state. Thus, the Pt–Pt distance depends less on the substituent on pz in the T_1-global minimum than in the S_0 state.

The dσ*(Pt–Pt) orbital is at a much higher energy in the T_1-global minimum geometry than in the S_0-equilibrium one in all complexes, as shown in Table 1. This is because the Pt–Pt distance is much shorter in the T_1-global minimum geometry than in the S_0-equilibrium one; note that the dσ*(Pt–Pt) orbital energy becomes higher as the Pt–Pt distance becomes shorter (Figure 2) because this orbital involves the dσ–dσ antibonding overlap. It is noted that the orbital energy of **$4T_{1a}$** is the highest in all the T_1-global minima, as shown in Table 1 and Figure 3. This is because the Pt–Pt distance of **$4T_{1a}$** is the shortest in these T_1-global minima. On the other hand, the dσ*(Pt–Pt) orbital is at a much lower energy in **$1T_{1a}$** and **$2T_{1a}$** because the Pt–Pt distance is considerably longer in these geometries. It is also noted that the orbital energy of **$3T_{1a}$** is little different from those of **$1T_{1a}$** and **$2T_{1a}$** (see Figure 3) in spite of the shorter Pt–Pt distance of **$3T_{1a}$** than those of **$1T_{1a}$** and **$2T_{1a}$**, as clearly shown in Table 1. These results are interpreted in terms of the symmetries of these complexes. Because all substituents on pz are the same in **1**, **2**, and **4** (H atoms in **1**, methyl groups in **2**, and *tert*-butyl groups in **4**; see Schemes 1 and 2), both the

Scheme 2.[a]

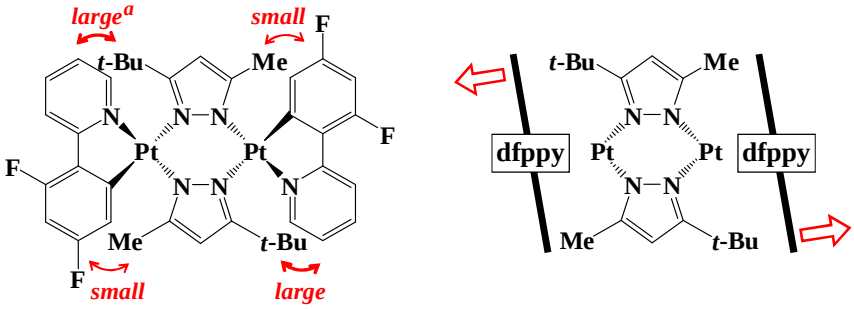

3 (C_2 symmetry)

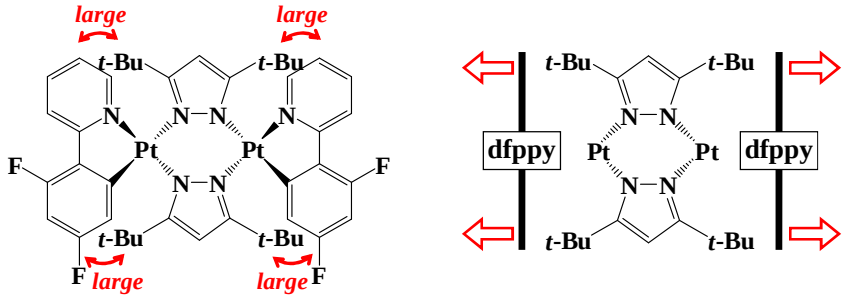

4 (C_S symmetry)

(a) Red arrows schematically represents the steric repulsion between dfppy and substituents on pz.

phenyl and the pyridine moieties of dfppy are pushed away to a similar extent by these substituents on pz. As a result, $\mathbf{1T_{1a}}$, $\mathbf{2T_{1a}}$, and $\mathbf{4T_{1a}}$ take the C_s-like geometry. Because the d_{z^2} orbital of Pt1 expands toward the Pt2 atom in this geometry, the dσ–dσ antibonding overlap is large, which considerably raises the dσ*(Pt–Pt) orbital energy. In **3**, two large *tert*-butyl groups and two small methyl groups are introduced to pz. Because the pyridine moiety of dfppy is strongly pushed away by the *tert*-butyl group but the phenyl moiety is moderately pushed away by the methyl group, as shown in Scheme 2, $\mathbf{3T_{1a}}$ takes not the C_s-like symmetry but the C_2-like one. In this geometry, the d_{z^2} orbital of Pt1 does not expand toward Pt2, and its direction deviates from the Pt–Pt line, which decreases the

dσ–dσ antibonding overlap. As a result, the dσ*(Pt–Pt) orbital energy of **3** is not destabilized very much but becomes similar to those of **1** and **2** in spite of its shorter Pt–Pt distance than those of **1** and **2**.

We tried to optimize the T_1-geometry with the π–π* excitation of dfppy and found a T_1-local minimum of **1** and **2** (**1T$_{1b}$** and **2T$_{1b}$**), as shown in Table 1 and Figure 1. We ascertained that these local minima have no imaginary frequency. These T_1-local minima are less stable than the T_1-global minima by 0.09 eV in **1** and 0.21 eV in **2**.[19] Their geometries are similar to the S_0-equilibrium geometries unlike **1T$_{1a}$** and **2T$_{1a}$**. This is easily understood in terms of the electronic structures of **1T$_{1b}$** and **2T$_{1b}$**. Because the dσ*(Pt–Pt) orbital is doubly occupied in **1T$_{1b}$** and **2T$_{1b}$** like **1S$_0$** and **2S$_0$**, as shown in Figure 2, the dσ–dσ bonding interaction is not formed at all in **1T$_{1b}$** and **2T$_{1b}$**, which is consistent with the long Pt–Pt distance of **1T$_{1b}$** (3.410 Å) and **2T$_{1b}$** (3.252 Å). Several interesting features are observed in **1T$_{1b}$** and **2T$_{1b}$**, as follows: (1) Though the π and π* orbitals of dfppy are delocalized on the whole molecule in **1S$_0$**, **2S$_0$**, **1T$_{1a}$**, and **2T$_{1a}$**, they are localized on one dfppy in **1T$_{1b}$** and **2T$_{1b}$**. (2) The dπ(Pt–Pt) orbital weakly interacts with the π orbital of dfppy in an antibonding way in **1S$_0$**, **2S$_0$**, **1T$_{1b}$**, and **2T$_{1b}$**, where the dπ(Pt–Pt) represents the dπ–dπ bonding orbital between two Pt atoms. (3) But, the dπ(Pt–Pt) orbital slightly participates with the π* orbital of dfppy in **1T$_{1b}$** and **2T$_{1b}$**. Thus, the electronic structures of **1T$_{1b}$** and **2T$_{1b}$** are not simple ligand-centered π–π* excited states but the mixture of ligand-centered π–π* excited states and metal-to-ligand charge transfer excited states (^{3}LC/MLCT). This feature is similar to the T_1 state of **5** (**5T$_1$**). Actually, the π(dfppy) and π*(dfppy) orbital energies are almost the same in **1T$_{1b}$**, **2T$_{1b}$**, and **5T$_1$**, as shown in Table 1. In other words, the electronic structures of **1T$_{1b}$** and **2T$_{1b}$** are similar to that of **5T$_1$**.

No local minima, which corresponds to **1T$_{1b}$** and **2T$_{1b}$**, however, could be optimized in the T_1 state of **3** and **4**. This is easily interpreted in terms of the large steric repulsion between the substituents on pz and dfppy. As shown in Figure 1, this large steric repulsion

significantly decreases the Pt–Pt distance even in the ground state; actually, the Pt–Pt distance of **4** is much shorter than that of **1**. The short Pt–Pt distance considerably destabilizes the dσ*(Pt–Pt) orbital energy, which leads to a considerably stable ^{3}MMLCT excited state relative to the ^{3}LC/MLCT excited state. As a result, the ^{3}LC/MLCT excited state cannot become local minima in **3** and **4**.

3.3.3. Phosphorescence Spectra of $[Pt_2(\mu\text{-}pz)_2(dfppy)_2]$ (1) and $[Pt_2(\mu\text{-}Me_2pz)_2(dfppy)_2]$ (2)

PECs of the S_0 and T_1 states of **1** and **2** are represented as a function of the Pt–Pt distance (Figures 4a and 4b), in which both S_0- and T_1-geometries were optimized at each Pt–Pt distance. A small but non-negligible activation barrier exists between the T_1-global (**$1T_{1a}$** and **$2T_{1a}$**) and the T_1-local minima (**$1T_{1b}$** and **$2T_{1b}$**). Because of the presence of this barrier, it is likely that the T_1-geometries of **1** and **2** stay at these T_1-local minima in frozen 2-MeTHF at 77 K and polystyrene at RT, where geometry changes do not easily occur. Thus, the energy of phosphorescence in these conditions corresponds to the energy difference between the T_1 and the S_0 states at the T_1-local minimum geometry (**$1T_{1b}$** and **$2T_{1b}$**). This energy difference is calculated to be 2.35 eV in both complexes, which agrees well with the experimental value,[5] as shown in Table 2. These phosphorescence spectra are assigned as the π*(dfppy) → π(dfppy) + d(Pt) transition because **$1T_{1b}$** and **$2T_{1b}$** are characterized as the ^{3}LC/MLCT excited state, as discussed above. This is theoretical support to the experimental assignment by Thompson et al.[5] Here, we wish to mention two split peaks experimentally observed in the phosphorescence spectra of **1** and **2**, when the measurement is carried out in frozen 2-MeTHF and polystyrene.[5] These split peaks were discussed in terms of the coupling with the breathing vibration of the aromatic ring of dfppy.[5,6] Because such vibrational coupling is not incorporated by the usual electronic structure calculation, we compare here the calculated energy of the phosphorescence with the averaged value of these two peaks.

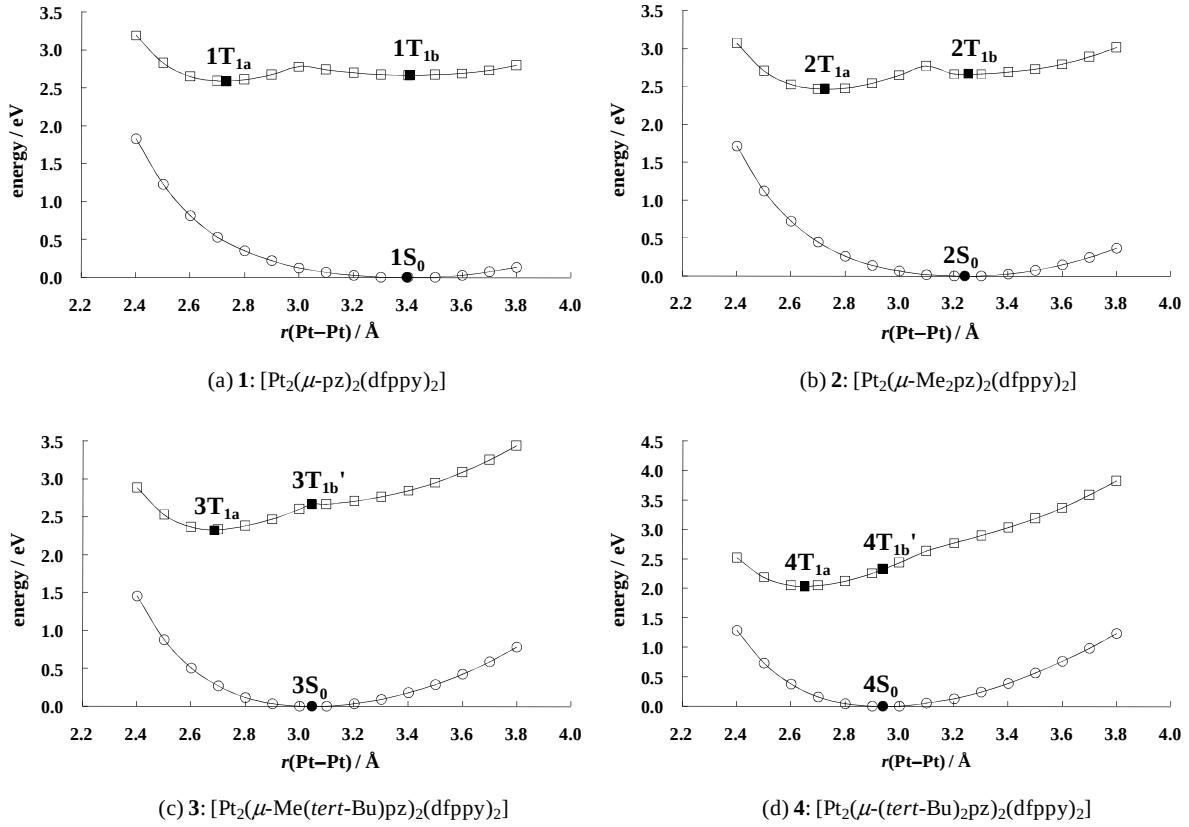

(a) **1**: $[Pt_2(\mu\text{-pz})_2(dfppy)_2]$ (b) **2**: $[Pt_2(\mu\text{-Me}_2pz)_2(dfppy)_2]$

(c) **3**: $[Pt_2(\mu\text{-Me}(tert\text{-Bu})pz)_2(dfppy)_2]$ (d) **4**: $[Pt_2(\mu\text{-}(tert\text{-Bu})_2pz)_2(dfppy)_2]$

Figure 4. PECs of the S_0 and T_1 states of dinuclear complexes **1**–**4** vs the Pt–Pt distance. The geometries of the S_0 and T_1 states were optimized with the DFT(B3PW91)/basis-I method at each Pt–Pt distance. It is noted that the energy difference between two curves does not correspond to the energy of phosphorescence because the T_1-curve represents the energy of the T_1-optimized geometry and the S_0-curve represents the energy of the S_0-optimized geometry.

In contrast to frozen 2-MeTHF at 77 K and polystyrene at RT, fluid 2-MeTHF at RT does not suppress the geometry change. Because the activation barrier between the local and the global minima is small in the T_1-potential energy curve (T_1-PEC), where the height of this activation barrier is 0.12 eV in **1** and 0.07 eV in **2**,[20] the geometries of **1** and **2** in the T_1 state easily change to their T_1-global minima (**1T$_{1a}$** and **2T$_{1a}$**) in fluid 2-MeTHF. In this case, the energy of phosphorescence corresponds to the energy difference between the T_1 and the S_0 states at the T_1-global minimum geometry. These are calculated to be 1.92 and 1.98

eV in $\mathbf{1T_{1a}}$ and $\mathbf{2T_{1a}}$, respectively, which agree well with the experimental energies,[5] as shown in Table 2. The calculated energy of phosphorescence is little different between vacuum and THF, as shown in Table 2, indicating that the solvent effect is small in the energy of phosphorescence. The phosphorescence in fluid 2-MeTHF is assigned as the π*(dfppy) → dσ*(Pt–Pt) transition because the T_1-global minima ($\mathbf{1T_{1a}}$ and $\mathbf{2T_{1a}}$) are characterized as the ^{3}MMLCT excited states, as experimentally reported by Thompson et al.[5]

It is noted that the energy of phosphorescence is much lower in fluid 2-MeTHF at RT than in frozen 2-MeTHF at 77 K and polystyrene at RT, as shown in Table 2. This is interpreted in terms of the PECs of the S_0 and T_1 states. The S_0 state becomes less stable in energy than does the S_0-equilibrium geometry as the Pt–Pt distance becomes shorter, as shown in Figures 4a and 4b. Because the Pt–Pt distance in the T_1-global minimum geometry is much shorter than in the T_1-local minimum, which is similar to that in the S_0-equilibrium one, the energy difference between the T_1 and the S_0 states is much smaller at the T_1-global minimum geometry than at the T_1-local minimum one. Thus, the Stokes shift is much larger in fluid 2-MeTHF than in frozen 2-MeTHF and polystyrene.

When the phosphorescence spectrum is measured in fluid 2-MeTHF at RT, **1** exhibits two small peaks at 2.52 and 2.71 eV in addition to one large peak at 1.93 eV.[5] On the other hand, **2** exhibits only one peak at 1.93 eV in fluid 2-MeTHF. This difference between **1** and **2** is easily interpreted in terms of the equilibrium between the T_1-global and T_1-local minima. In **1**, the Gibbs free energy difference ($\Delta\Delta G^0$) between $\mathbf{1T_{1a}}$ and $\mathbf{1T_{1b}}$ at 298 K is very small (0.019 eV),[21] which leads to the equilibrium constant (K) of 0.48 and the somewhat large population (about 30 %) of $\mathbf{1T_{1b}}$. As a result, the phosphorescence occurs not only at the T_1-global minimum but also at the T_1-local minimum even in fluid 2-MeTHF. The complex **1** in the global minimum presents one large peak at 1.93 eV, and the complex **1** in the local minimum presents two small peaks at 2.52 and 2.71 eV; remember that the vibration coupling was observed at the local minimum. In **2**, however, the population at the

local minimum **2T$_{1b}$** is negligibly small because the $\Delta\Delta G^0$ between **2T$_{1a}$** and **2T$_{1b}$** at 298 K is large (0.13 eV). As a result, only one large peak is observed at low energy in **2**.

Here, we wish to make a comparison of the phosphorescence spectra of **1** and **2** with that of the mononuclear complex **5**. The optimized geometry of the T_1 state (**5T$_1$**) is almost the same as the S_0-equilibrium one (**5S$_0$**), as shown in Table 1. Thus, the Stokes shift is expected to be small and little different between fluid 2-MeTHF and frozen 2-MeTHF. Actually, the experimentally reported phosphorescence spectrum in frozen 2-MeTHF at 77 K is almost the same as that in fluid 2-MeTHF at RT, as shown in Table 2. The energy differences between the S_0 and the T_1 states at **5T$_1$** are 2.35 and 2.36 eV in a vacuum and in 2-MeTHF, respectively, which agree well with the experimental phosphorescence spectrum,[5] as shown in Table 2. This phosphorescence spectrum is assigned as the π^*(dfppy) → π(dfppy) + d(Pt) transition like those of **1T$_{1b}$** and **2T$_{1b}$**. This is because **1T$_{1b}$**, **2T$_{1b}$**, and **5T$_1$** take the ^{3}LC/MLCT excited state, as shown in Figure 2. It is noted that the energies of phosphorescence of **1T$_{1b}$** and **2T$_{1b}$** are almost the same as that of **5T$_1$**, indicating that the phosphorescence occurs in **1T$_{1b}$** and **2T$_{1b}$** like that of the mononuclear complex **5**; in other words, any character of dinuclear complex does not participate in the phosphorescence of **1T$_{1b}$** and **2T$_{1b}$**.

3.3.4. Phosphorescence Spectra of [Pt$_2$(μ-Me^{t}Bupz)$_2$(dfppy)$_2$] (3) and [Pt$_2$(μ-^{t}Bu$_2$pz)$_2$(dfppy)$_2$] (4)

PECs of the S_0 and T_1 states of **3** and **4** are represented as a function of the Pt–Pt distance in Figures 4c and 4d. It is noted here that the T_1-local minimum is absent in these PECs. However, the electronic structure of the T_1 state depends on the Pt–Pt distance like **1** and **2**, as follows: The T_1 state of **3** and **4** is the ^{3}MMLCT excited state when the Pt–Pt distance is shorter than 3.10 Å but is the ^{3}LC/MLCT excited state when the Pt–Pt distance is longer than 3.10 Å. Actually, the PEC of the T_1 state is not smooth around 3.10 Å, suggesting that the electronic structure changes around here.

Table 2. Energies (in eV)[a] of phosphorescence spectra of **1** to **5** and their assignments

			energy of phosphorescence			
			calc		expt[b]	
comp	geom	assignment	vacuum	THF		
1	**$1T_{1b}$**	π*(dfppy) → π(dfppy) + d(Pt)	2.35	2.37	2.52, 2.71	(2-MeTHF at 77K)
					2.50, 2.66	(polystyrene at RT)
	$1T_{1a}$	π*(dfppy) → dσ*(Pt–Pt)	1.97	1.92	1.93	(2-MeTHF at RT)
2	**$2T_{1b}$**	π*(dfppy) → π(dfppy) +d(Pt)	2.35	2.37	2.49, 2.68	(2-MeTHF at 77K)
					2.46, 2.63	(polystyrene at RT)
	$2T_{1a}$	π*(dfppy) → dσ*(Pt–Pt)	1.92	1.98	1.98	(2-MeTHF at RT)
3	**$3T_{1b}$'**	π*(dfppy) → dσ*(Pt–Pt)	2.54	2.57	2.49	(2-MeTHF at 77K)
					2.27	(polystyrene at RT)
	$3T_{1a}$	π*(dfppy) → dσ*(Pt–Pt)	1.88	1.92	1.95	(2-MeTHF at RT)
4	**$4T_{1b}$'**	π*(dfppy) → dσ*(Pt–Pt)	2.17	2.20	2.18	(2-MeTHF at 77K)
					1.96	(polystyrene at RT)
	$4T_{1a}$	π*(dfppy) → dσ*(Pt–Pt)	1.59	1.63	1.80	(2-MeTHF at RT)
5	**$5T_1$**	π*(dfppy) → π(dfppy) + d(Pt)	2.35	2.36	2.51, 2.69	(2-MeTHF at 77K)
					2.49, 2.66	(2-MeTHF at RT)

(a) The energy of phosphorescence is defined as the energy difference between the T_1 and S_0 states at the same geometry (vertical transition energy). This energy difference was calculated by the DFT(B3PW91)/basis-II method. (b) See ref 5.

First, we assumed that the phosphorescence of **3** and **4** occurs at the S_0-equilibrium geometry in frozen 2-MeTHF at 77 K like **1** and **2** because the geometry changes little in these conditions. In this case, the energy of phosphorescence corresponds to the energy difference between the T_1 and the S_0 states at the S_0-equilibrium geometry (**$3S_0$** and **$4S_0$**); in other words, we assumed that no geometry change occurs in frozen 2-MeTHF. The

calculated energies are 2.67 eV in $\mathbf{3S_0}$ and 2.35 eV in $\mathbf{4S_0}$, which are somewhat larger than the experimental values (2.49 eV in **3** and 2.18 eV in **4**; Table 2).[5] These results suggest that the geometry is not completely fixed in frozen 2-MeTHF. It is likely that the solvent cage little changes in frozen 2-MeTHF but the geometry changes occur in this solvent cage. We assumed that the geometry change in the solvent cage occurs without change of the Pt–Pt distance because the change of the Pt–Pt distance would need the change of the solvation cage. Thus, the geometries of **3** and **4** in the T_1 state were optimized with the Pt–Pt distance fixed to be the same as that of the S_0-equilibrium geometry (3.044 Å in **3** and 2.939 Å in **4**). In such optimized geometries ($\mathbf{3T_{1b}'}$ and $\mathbf{4T_{1b}'}$), the energies of phosphorescence are evaluated to be 2.54 and 2.17 eV in **3** and **4**, respectively, which agree well with the experimental values in frozen 2-MeTHF,[5] as shown in Table 2. These results suggest that the geometry changes moderately occur in the solvent cage of frozen 2-MeTHF. The phosphorescence spectra are assigned as the π*(dfppy) → dσ*(Pt–Pt) transition because the T_1 state at these Pt–Pt distances is characterized as the ^{3}MMLCT state, as discussed above. The energy of this phosphorescence is considerably lower in $\mathbf{4T_{1b}'}$ than in $\mathbf{3T_{1b}'}$. This result is interpreted in terms of the Pt–Pt distance as follows: Because the Pt–Pt distance (2.939 Å) of $\mathbf{4T_{1b}'}$ is considerably shorter than that (3.044 Å) of $\mathbf{3T_{1b}'}$, the dσ–dσ antibonding overlap is considerably larger in $\mathbf{4T_{1b}'}$ than in $\mathbf{3T_{1b}'}$, which leads to the higher energy of the dσ*(Pt–Pt) orbital in $\mathbf{4T_{1b}'}$ (–5.02 eV) than in $\mathbf{3T_{1b}'}$ (–5.36 eV). On the other hand, the energy of the π*(dfppy) orbital is little different between $\mathbf{4T_{1b}'}$ (–2.16 eV) and $\mathbf{3T_{1b}'}$ (–2.11 eV). Thus, the energy of phosphorescence is lower in **4** than in **3**.

In fluid 2-MeTHF at RT, the phosphorescence occurs at the T_1-global minimum geometry ($\mathbf{3T_{1a}}$ and $\mathbf{4T_{1a}}$) like **1** and **2** because the geometry easily changes to the T_1-global minimum. The energy of phosphorescence is evaluated to be 1.92 and 1.63 eV in **3** and **4**, respectively, as shown in Table 2. The calculated energy of **3** agrees well with the experimental value,[5] while that of **4** is moderately lower than the experimental value.

These phosphorescence spectra are assigned as the π*(dfppy) → dσ*(Pt–Pt) transition because the T_1-global minimum is characterized as the ^{3}MMLCT excited state. This assignment agrees with the experimental proposal.[5] Interestingly, both experimental and theoretical results indicate that the energy of phosphorescence of **4** is much lower than those of **1**, **2**, and **3** in fluid 2-MeTHF. This result is interpreted in terms of the dσ–dσ antibonding overlap. Because the Pt–Pt distance of $\mathbf{4T_{1a}}$ is the shortest in all the T_1-global minimum geometries, the dσ*(Pt–Pt) orbital of $\mathbf{4T_{1a}}$ is at the highest energy in those of $\mathbf{1T_{1a}}$–$\mathbf{4T_{1a}}$. As a result, the π*(dfppy) → dσ*(Pt–Pt) phosphorescence occurs at the lowest energy in **4**.

It is noted here that the energy of phosphorescence of $\mathbf{3T_{1a}}$ is almost the same as those of $\mathbf{1T_{1a}}$ and $\mathbf{2T_{1a}}$, as shown in Table 2, in spite of the shorter Pt–Pt distance of $\mathbf{3T_{1a}}$ than those of $\mathbf{1T_{1a}}$ and $\mathbf{2T_{1a}}$ (see Table 1). This is because the dσ*(Pt–Pt) orbital of $\mathbf{3T_{1a}}$ is at an energy similar to those of $\mathbf{1T_{1a}}$ and $\mathbf{2T_{1a}}$ (Figure 3); remember that the dσ*(Pt–Pt) orbital energy of $\mathbf{3T_{1a}}$ is not destabilized very much in spite of the short Pt–Pt distance because the d_{z^2} orbital of one Pt atom does not extend toward the other Pt atom and its direction deviates from the Pt–Pt line in **3** because of the C_2 symmetry of $\mathbf{3T_{1a}}$ (see above and Scheme 2).

The energy of phosphorescence of **4** is moderately lower in fluid 2-MeTHF at RT than in frozen 2-MeTHF at 77 K, but that of **3** is considerably lower in fluid 2-MeTHF at RT than in frozen 2-MeTHF at 77 K. Because the phosphorescence occurs at the T_1-global minimum geometry ($\mathbf{3T_{1a}}$ and $\mathbf{4T_{1a}}$) in fluid 2-MeTHF but at the geometry ($\mathbf{3T_{1b}'}$ and $\mathbf{4T_{1b}'}$) that is similar to the S_0-equilibrium one in frozen 2-MeTHF, the above-mentioned difference between **3** and **4** arises from the difference in the geometry of the T_1 state between **3** and **4**, as follows: The geometry difference between $\mathbf{4T_{1a}}$ and $\mathbf{4S_0}$ is considerably smaller than that between $\mathbf{3T_{1a}}$ and $\mathbf{3S_0}$; for instance, the Pt–Pt distance of the T_1-global minimum is shorter than that of the S_0-equilibrium one by 0.290 Å in **4** and 0.358 Å in **3**, as shown in Table 1. Because the $\mathbf{3S_0}$ and $\mathbf{4S_0}$ geometries are similar to the $\mathbf{3T_{1b}'}$ and $\mathbf{4T_{1b}'}$ geometries,

respectively, as discussed above, the T_1 geometry considerably changes upon going from **$3T_{1b}$'** to **$3T_{1a}$** but moderately upon going from **$4T_{1b}$'** to **$4T_{1a}$**. This is the reason why the energy of phosphorescence of **4** is moderately lower in fluid 2-MeTHF than in frozen 2-MeTHF but that of **3** is considerably lower in the former solution than in the latter one.

The reason why the geometry difference between **$4T_{1a}$** and **$4S_0$** is smaller than that between **$3T_{1a}$** and **$3S_0$** is explained in terms of the steric repulsion between the substituents on pz and dfppy. As discussed in Section 3.3.2, the S_0-equilibrium geometry depends considerably on this steric repulsion; because **4** has four large *tert*-butyl substituents but **3** has two large *tert*-butyl and two small methyl substituents on pz, the steric repulsion is much larger in **4** than in **3**. As a result, the Pt–Pt distance is considerably shorter in the S_0-equilibrium geometry of **4** than of **3**. On the other hand, the T_1-global minimum geometry depends less on the steric repulsion than does the S_0-equilibrium one because the $d\sigma$(Pt–Pt) bonding interaction plays important roles to determine the geometry of the T_1-global minimum in addition to the steric repulsion (see above); actually, the Pt–Pt distance of **$4S_0$** is considerably shorter than that of **$3S_0$** by 0.105 Å, but the Pt–Pt distance of **$4T_{1a}$** is little different from that of **$3T_{1a}$** (see Table 1). In other words, the Pt–Pt distance of **$4S_0$** is already short relative to that of **$3S_0$**. Thus, the geometry changes take place less upon going to **$4T_{1a}$** from **$4S_0$** than upon going to **$3T_{1a}$** from **$3S_0$**.

The energies of phosphorescence in polystyrene at RT are experimentally reported to be 2.27 and 1.96 eV in **3** and **4**, respectively,[5] which are lower than those in frozen 2-MeTHF at 77 K but higher than those in fluid 2-MeTHF at RT, as shown in Table 2. These results are different from those of **1** and **2**, where the energy of phosphorescence in polystyrene is almost the same as that in frozen 2-MeTHF. The results of **1** and **2** were interpreted in terms that the T_1 state is in the local minimum geometry (**$1T_{1b}$** and **$2T_{1b}$**), which is similar to the S_0-equilibrium geometry in frozen 2-MeTHF and polystyrene, as discussed in Section 3.3.3. On the other hand, there are no local minima in the T_1-PECs of **3** and **4**, as shown in Figures

4c and 4d. In such cases, it is likely that the geometry does not completely change to the T_1-global minimum geometry (**$3T_{1a}$** and **$4T_{1a}$**) but moderately changes toward the T_1-global minimum in polystyrene. In other words, in polystyrene, the geometries of **3** and **4** are intermediate between the considerably distorted T_1-global minimum geometry and the slightly distorted T_1-geometry (**$3T_{1b}$'** and **$4T_{1b}$'**) taken in the frozen 2-MeTHF. This is the reason why the energies of phosphorescence of **3** and **4** are lower in polystyrene than in frozen 2-MeTHF but higher than those in fluid 2-MeTHF. In addition, these results suggest that the rigidity of polystyrene is lower than that of frozen 2-MeTHF. The phosphorescence spectra of **3** and **4** in polystyrene are assigned as the π^*(dfppy) → dσ^*(Pt–Pt) transition because the Pt–Pt distance is shorter than 3.1 Å (see above).

3.4. Conclusions

Four kinds of 3,5-dialkylpyrazolate(R_2pz)-bridged platinum(II) dinuclear complexes [$Pt_2(\mu$-$R_2pz)_2(dfppy)_2$] (dfppy = 2-(2,4-difluorophenyl)pyridine; R_2pz = pyrazolate in **1**, 3,5-dimethylpyrazolate in **2**, 3-methyl-5-*tert*-butylpyrazolate in **3**, and 3,5-bis(*tert*-butyl)pyrazolate in **4**) were theoretically investigated by the DFT(B3PW91) method to present detailed knowledge of their geometries and electronic structures in the T_1 state and to clarify the reason why the phosphorescence spectra significantly depend on the substituent on pz and the measurement conditions.

In **1** and **2** bearing H atoms and methyl groups on pz, respectively, the T_1-local minimum exists besides the T_1-global minimum. The Pt–Pt distance of the T_1-local minimum is similar to that of the S_0-equilibrium geometry, but the Pt–Pt distance of the T_1-global minimum is considerably shorter than that of the S_0-equilibrium one. The phosphorescence occurs at this local minimum in frozen 2-MeTHF at 77 K and polystyrene at RT because the geometry of the T_1 state is captured in this local minimum. This phosphorescence spectrum is assigned as the π^*(dfppy) → π(dfppy) + d(Pt) transition. In

fluid 2-MeTHF at RT, the geometry of the T_1 state easily changes to the T_1-global minimum geometry (**$1T_{1a}$** and **$2T_{1a}$**). Because geometries of **$1T_{1a}$** and **$2T_{1a}$** are much different from the S_0-equilibrium geometries, the energy of phosphorescence is much lower in fluid 2-MeTHF than in frozen 2-MeTHF and polystyrene. Because the T_1 state at the T_1-global minimum geometry is characterized as the ^{3}MMLCT excited state, the phosphorescence in fluid 2-MeTHF is assigned as the π^*(dfppy) → dσ^*(Pt–Pt) transition.

In **3** and **4** bearing methyl and/or *tert*-butyl substituents on pz, no local minimum is optimized in the T_1 state. The reason is easily understood as follows: Because the bulky *tert*-butyl substituents strongly push the dfppy plane away to decrease the Pt–Pt distance, the dσ^*(Pt–Pt) → π^*(dfppy) excited state becomes stable, and the π(dfppy) + d(Pt) → π^*(dfppy) excited state cannot become a local minimum. The geometry of the T_1 state changes slightly in frozen 2-MeTHF at 77 K except for the Pt–Pt distance, and it moderately changes in polystyrene at RT unlike in **1** and **2**. This is because the T_1-local minimum is absent in the T_1-PEC. Thus, the energy of phosphorescence is somewhat lower in polystyrene than in frozen 2-MeTHF. In fluid 2-MeTHF at RT, the geometry of the T_1 state completely changes to the T_1-global minimum geometry. This geometry change largely occurs in **3** but moderately in **4** because the Pt–Pt distance is already short in **$4S_0$** due to the presence of four *tert*-butyl groups on pz but still considerably long in **$3S_0$** due to the presence of two methyl groups. As a result, the energy of phosphorescence of **3** is much lower in fluid 2-MeTHF than in frozen 2-MeTHF, but that of **4** is moderately lower in fluid 2-MeTHF than in frozen 2-MeTHF. The phosphorescence spectra of **3** and **4** in these conditions are assigned as the π^*(dfppy) → dσ^*(Pt–Pt) transition.

In conclusion, interesting phosphorescence spectra of these pz-bridged dinuclear platinum(II) complexes are successfully understood in terms of their PECs of the T_1 state.

3.5. Appendix

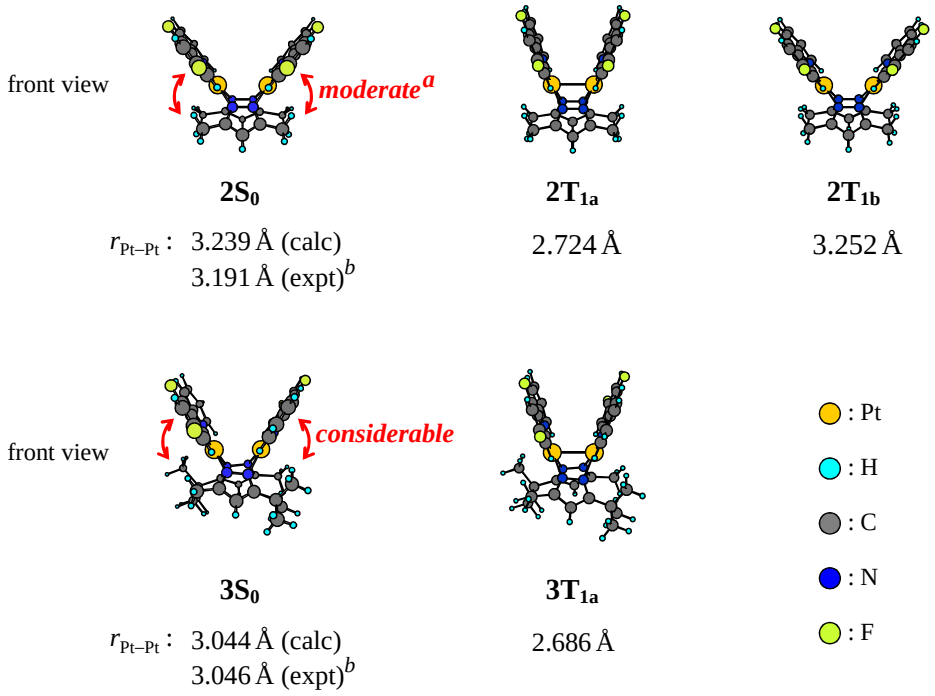

Figure A1. S_0- and T_1-optimized geometries of **2** and **3**. (a) A red arrow schematically represents the steric repulsion between dfppy and substituents (four methyl groups in **2** and two *tert*-butyl and two methyl groups in **3**) on pz. (b) Ref 5.

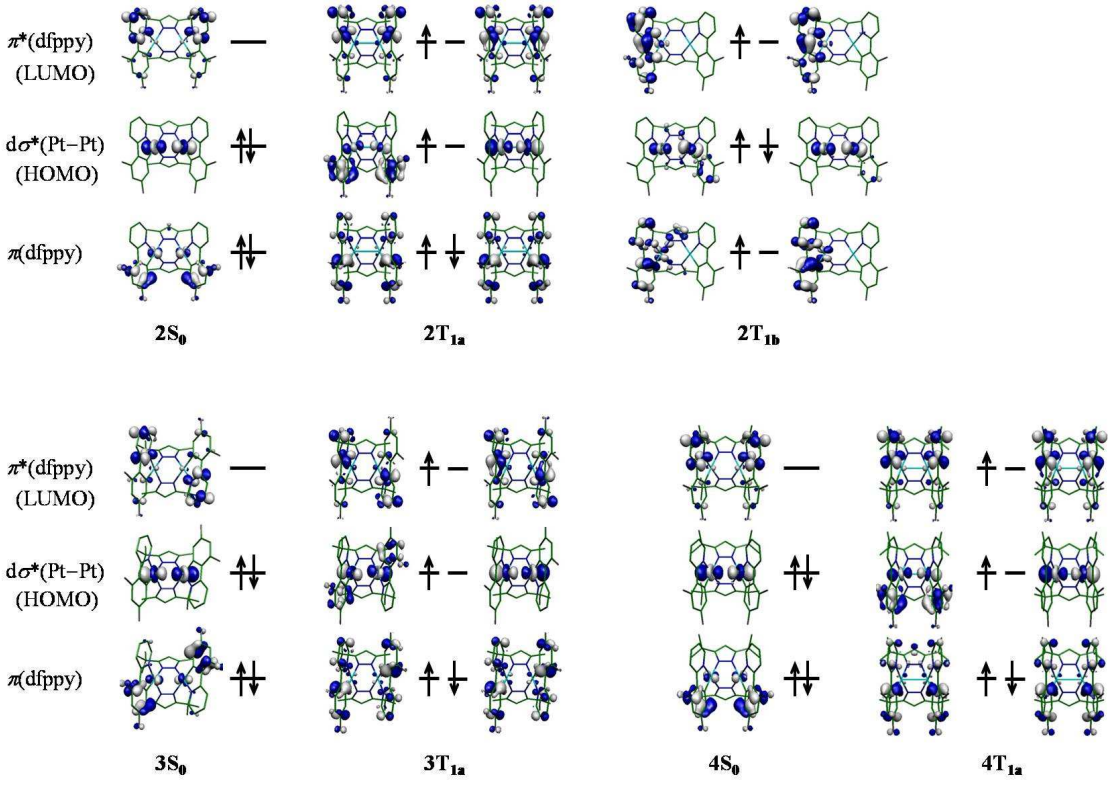

Figure A2. Several important molecular orbitals of **2**, **3**, and **4**. H atoms are omitted for brevity.

References and Notes

(1) Selected reviews for emissive complexes applied to optical meterials: (a) Amendola, V.; Fabbrizzi, L.; Foti, F.; Licchelli, M.; Mangano, C.; Pallavicini, P.; Poggi, A.; Sacchi, D.; Taglietti, A. *Coord. Chem. Rev.* **2006**, *250*, 273. (b) Rogers, C. W.; Wolf, M. O. *Coord. Chem. Rev.* 2002, *233–234*, 341. (c) Keefe, M. H.; Benkstein, K. D.; Hupp, J. T. *Coord. Chem. Rev.* **2000**, *205*, 201.

(2) Selected reviews for emissive iridium complexes applied to optical materials: (a) Evans, R. C.; Douglas, P.; Winscom, C. J. *Coord. Chem. Rev.* **2006**, *250*, 2093. (b) Marin, V.; Holder, E.; Hoogenboom, R.; Schubert, U. S. *Chem. Soc. Rev.* **2007**, *36*, 618. (c) Lo, K. K.-W.; Hui, W.-K.; Chung, C.-K.; Tsang, K. H.-K.; Lee, T. K.-M.; Li, C.-K.; Lau, J. S.-Y.; Ng, D. C.-M. *Coord. Chem. Rev.* **2006**, *250*, 1724. (d) Lo, K. K.-W.; Hui, W.-K.; Chung, C.-K.; Tsang, K. H.-K.; Ng, D. C.-M.; Zhu, N.; Cheung, K.-K. *Coord. Chem. Rev.* **2005**, *249*, 1434.

(3) Selected reviews for emissive platinum complexes applied to optical materials: (a) Yam, V. W.-W. *Acc. Chem. Res.* **2002**, *35*, 555. (b) Hissler, M.; McGarrah, J. E.; Connick, W. B.; Geiger, D. K.; Cummings, S. D.; Eisenberg, R. *Coord. Chem. Rev.* **2000**, *208*, 115. (c) Paw, W.; Cummings, S. D.; Mansour, M. A.; Connick, W. B.; Geiger, D. K.; Eisenberg, R. *Coord. Chem. Rev.* **1998**, *171*, 125.

(4) Selected review for fundamental study of emissive platinum complexes: Wong, K. M.-C.; Hui, C.-K.; Yu, K.-L.; Yam, V. W.-W. *Coord. Chem. Rev.* **2002**, *229*, 123.

(5) Ma, B.; Li, J.; Djurovich, P. I.; Yousufuddin, M.; Bau, R.; Thompson, M. E. *J. Am. Chem. Soc.* **2005**, *127*, 28.

(6) Brooks, J.; Babayan, Y.; Lamansky, S.; Djurovich, P. I.; Tsyba, I.; Bau, R.; Thompson, M. E. *Inorg. Chem.* **2002**, *41*, 3055.

(7) Hay, P. J.; Wadt, W. R. *J. Chem. Phys.* **1985**, *82*, 299.

(8) Couty, M.; Hall, M. B. *J. Comput. Chem.* **1996**, *17*, 1359.

(9) Ehlers, A. W.; Böhme, M.; Dapprich, S.; Gobbi, A.; Höllwarth, A.; Jonas, V.; Köhler, K. F.; Stegmann, R.; Veldkamp, A.; Frenking, G. *Chem. Phys. Lett.* **1993**, *208*, 111.

(10) (a) Hehre, W. J.; Ditchfield, R.; Pople, J. A. *J. Chem. Phys.* **1972**, *56*, 2257. (b) Hariharan, P. C.; Pople, J. A. *Theor. Chim. Acta* **1973**, *28*, 213.

(11) Dunning, T. H. *J. Chem. Phys.* **1989**, *90*, 1007.

(12) Becke, A. D. *J. Chem. Phys.* **1993**, *98*, 5648.

(13) Perdew, J. P.; Wang, Y. *Phys. Rev. B* **1992**, *45*, 13244.

(14) (a) Mennucci, B.; Tomasi, J. *J. Chem. Phys.* **1997**, *106*, 5151. (b) Cancès, M. T.; Mennucci, B.; Tomasi, J. *J. Chem. Phys.* **1997**, *107*, 3032. (c) Cossi, M.; Barone, V.; Mennucci, B.; Tomasi, J. *Chem. Phys. Lett.* **1998**, *286*, 253. (d) Tomasi, J.; Persico, M. *Chem. Rev.* **1994**, *94*, 2027.

(15) Jakowski, J; Simons, J. *J. Am. Chem. Soc.* **2003**, *125*, 16089.

(16) Frisch, M. J.; Trucks, G. W.; Schlegel, H. B.; Scuseria, G. E.; Robb, M. A.; Cheeseman, J. R.;

Montgomery, J. A., Jr.; Vreven, T.; Kudin, K. N.; Burant, J. C.; Millam, J. M.; Iyengar, S. S.; Tomasi, J.; Barone, V.; Mennucci, B.; Cossi, M.; Scalmani, G.; Rega, N.; Petersson, G. A.; Nakatsuji, H.; Hada, M.; Ehara, M.; Toyota, K.; Fukuda, R.; Hasegawa, J.; Ishida, M.; Nakajima, T.; Honda, Y.; Kitao, O.; Nakai, H.; Klene, M.; Li, X.; Knox, J. E.; Hratchian, H. P.; Cross, J. B.; Bakken, V.; Adamo, C.; Jaramillo, J.; Gomperts, R.; Stratmann, R. E.; Yazyev, O.; Austin, A. J.; Cammi, R.; Pomelli, C.; Ochterski, J. W.; Ayala, P. Y.; Morokuma, K.; Voth, G. A.; Salvador, P.; Dannenberg, J. J.; Zakrzewski, V. G.; Dapprich, S.; Daniels, A. D.; Strain, M. C.; Farkas, O.; Malick, D. K.; Rabuck, A. D.; Raghavachari, K.; Foresman, J. B.; Ortiz, J. V.; Cui, Q.; Baboul, A. G.; Clifford, S.; Cioslowski, J.; Stefanov, B. B.; Liu, G.; Liashenko, A.; Piskorz, P.; Komaromi, I.; Martin, R. L.; Fox, D. J.; Keith, T.; Al-Laham, M. A.; Peng, C. Y.; Nanayakkara, A.; Challacombe, M.; Gill, P. M. W.; Johnson, B.; Chen, W.; Wong, M. W.; Gonzalez, C.; Pople, J. A. *Gaussian 03*, revision C.02; Gaussian, Inc.: Wallingford, CT, 2004.

(17) (a) Flükiger, P.; Lüthi, H. P.; Portmann, S.; Weber, J. MOLEKEL, version 4.3; Scientific Computing: Manno, Switzerland, 2000. (b) Portmann, S.; Lüthi, H. P. *CHIMIA* **2000**, *54*, 766.

(18) Because the dihedral angle *d*(N1–N2–N3–N4) is 180.0° in **1S$_0$**, **2S$_0$**, and **4S$_0$**, the N1, N2, N3, and N4 are in one plane. In **3S$_0$**, the dihedral angle *d*(N1–N4–N3–N2) is 168.4°, indicating that these atoms are not on one plane, strictly speaking. However, the deviation from the plane is small.

(19) These energy differences were calculated with the DFT(B3PW91)/basis-II method, where the T_1-local (**1T$_{1b}$** and **2T$_{1b}$**) and T_1-global minimum geometries (**1T$_{1a}$** and **2T$_{1a}$**) were optimized with the DFT(B3PW91)/basis-I method.

(20) The activation barrier corresponds to the energy difference between the T_1-optimized geometry at *r*(Pt–Pt) = 3.000 Å and the T_1-local minimum geometry (**1T$_{1b}$**) in **1** and between the T_1-optimized geometry at *r*(Pt–Pt) = 3.100 Å and the T_1-local minimum geometry (**2T$_{1b}$**) in **2**, where the transition state is at *r*(Pt–Pt) = 3.000 Å in **1** and at *r*(Pt–Pt) = 3.100 Å in **2**. These energy differences were calculated with the DFT(B3PW91)/basis-II//DFT(B3PW91)/basis-I method, where the geometries were optimized at each Pt–Pt distance. These activation barriers are a little bit overestimated, as follows: Because the transition state here is a crossing point of two states, the transition state should be calculated with a multireference method. However, the values presented here are not very much different from the correct values because the PEC of the T_1 state is not steep but rather flat in the righthand side of the transition state (see Figure 4).

(21) The $\Delta\Delta G^0$ value is defined as the difference in the Gibbs free energy (ΔG^0) between **1T$_{1a}$** and **1T$_{1b}$**. Each ΔG^0 value was evaluated as follows: (1) The energies of **1T$_{1a}$** and **1T$_{1b}$** were calculated with the DFT(B3PW91)/basis-II method. (2) The zero-point energy was evaluated with the DFT(B3PW91)/basis-I method. (3) A thermal correction at 298 K was made with the partition function of the vibration movements, in which the partition function was evaluated by the DFT(B3PW91)/basis-I method.

Chapter 4

Theoretical Study of Excited States of Pyrazolate- and Pyridinethiolate-Bridged Dinuclear Platinum(II) Complexes: Relationship between Geometries of Excited States and Phosphorescence Spectra

4.1. Introduction

Emissive transition-metal complexes have drawn a lot of interest because they are potentially useful to optical materials such as light-emitting devices, photochemical sensors, and biological labeling probes.[1–3] In particular, 5d transition metal complexes such as iridium[2] and platinum[2a,3–8] complexes have been well-investigated because large phosphorescence spectra are often observed in these complexes.

Recently, multinuclear transition metal complexes have been investigated in many experimental works[1c,2a,3–8] because they exhibit a variety of phosphorescence spectra. For instance, the phosphorescence spectrum of pyrazolate-bridged dinuclear platinum(II) complex $[Pt_2(\mu\text{-pz})_2(bpym)_2]^{2+}$ (**1**; pz = pyrazolate and bpym = 2,2'-bipyrimidine; see Scheme 1)[5] is observed in the solid state but not in the acetonitrile (CH_3CN) solution. However, that of pyridinethiolate-bridged dinuclear platinum(II) complex $[Pt_2(\mu\text{-pyt})_2(ppy)_2]$ (**2**; pyt = pyridine-2-thiolate and Hppy = 2-phenylpyridine; Scheme 1)[6] is observed in both the solid state and theCH_3CNsolution. It is of considerable interest to clarify the reasons why these moderately different bridging and chelating ligands induce the above-mentioned differences in phosphorescence behavior between **1** and **2**. The phosphorescence spectrum of **2** was experimentally discussed in terms of the geometries and electronic structures of the singlet ground state (S_0) and the lowest-energy triplet excited state (T_1).[6] However, the reasons for the above-mentioned differences between **1** and **2** have not been discussed yet. It is worth investigating theoretically the ground and excited states of **1** and **2** to understand their phosphorescence spectra and elucidate the reasons why the phosphorescence behavior

is different between them.

Scheme 1.

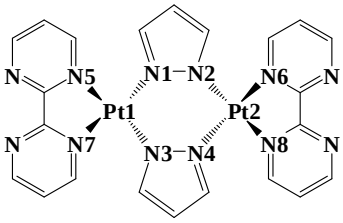

1

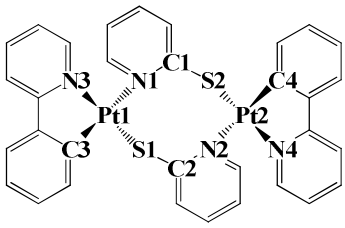

2

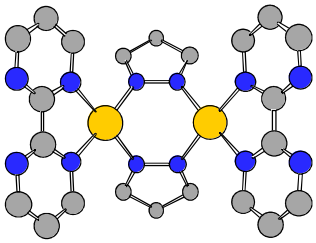

front view

top view of **1**

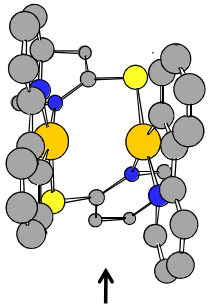

front view

top view of **2**

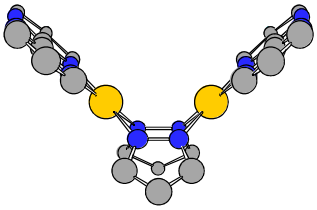

front view of **1**

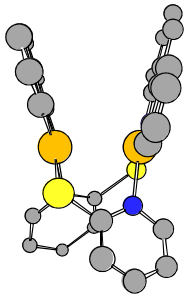

front view of **2**

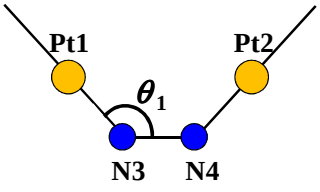

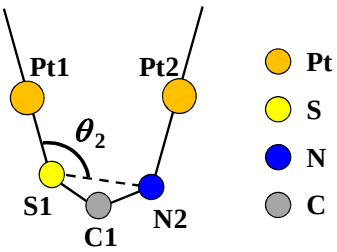

In this study, we theoretically investigated pz- and pyt-bridged dinuclear platinum(II) complexes **1** and **2** and discussed the geometries and electronic structures of the S_0 ground state and the lowest-energy singlet and triplet excited states (S_1 and T_1, respectively). We also discussed whether or not spin−orbit interaction between the S_1 and T_1 states operates, because this spin-orbit interaction plays an important role in the $S_1 \rightarrow T_1$ intersystem crossing. Our main purposes here are (i) to present a theoretical understanding of the geometries, electronic structures, and phosphorescence spectra of **1** and **2** and (ii) to clarify the reasons why the phosphorescence spectrum of **1** is absent but that of **2** is present in the CH_3CN solution and why those of **1** and **2** are observed in the solid state.

4.2. Computational Details

We employed two basis set systems (basis-I and II) in this study. In basis-I, core electrons (up to 4f) of platinum were replaced with the relativistic effective core potentials (ECPs) proposed by Hay and Wadt[9] and its valence electrons were represented by the (541/541/111/1) basis set.[9–11] The 6-31G* basis sets[12] were used for hydrogen, carbon, nitrogen, and sulfur. In basis-II, valence electrons of platinum were represented by the (5311/5311/111/1) basis set[9–11] with the same ECPs as those of basis-I. The cc-pVDZ basis sets[13] were used for hydrogen, carbon, nitrogen, and sulfur.

Geometries of **1** and **2** in the S_0 ground state were optimized by density functional theory (DFT) with basis I, where the B3PW91 functional[14,15] was employed. The geometries in the S_1 and T_1 excited states were optimized with the unrestricted (U)DFT method. Because the singly occupied molecular orbital (SOMO) bearing an α-spin electron is different from that bearing a β-spin electron in the S_1 state, the spin symmetry of the evaluated wave function is broken in the UDFT calculation.[16] In this meaning, the UDFT calculation of the S_1 state is called broken-symmetry (BS)DFT. It is also called permuted orbitals (PO)DFT in several cases.[17] We ascertained that all optimized geometries

exhibited no imaginary frequency. The potential energy curves (PECs) of **1** and **2** were evaluated as a function of the Pt–Pt distance in the S_0, S_1, and T_1 states, where all geometrical parameters were optimized at each Pt–Pt distance.

The energy of phosphorescence is calculated here as the energy difference between the S_0 and T_1 states at the T_1-optimized geometry. The total energies, orbital energies, and Mulliken charges were evaluated with the DFT(B3PW91)/basis-II//DFT(B3PW91)/basis-I method.[18] The solvent effect of the CH_3CN solution was taken into consideration by the polarizable continuum model (PCM).[19] The united-atom topological model of the universal force-field method (UA0)[19b,20] was employed to estimate the molecular volume and construct a molecular cavity in the PCM calculation.

The DFT calculations were performed by the Gaussian 03 (revision C.02) program package.[21] Molecular orbitals were drawn by the MOLEKEL (version 4.3) program.[22]

4.3. Results and Discussion

4.3.1. Equilibrium Geometries and Electronic Structures of $[Pt_2(\mu\text{-pz})_2(bpym)_2]^{2+}$ (1) in the S_0, S_1, and T_1 States

Important optimized geometrical parameters of the S_0 equilibrium geometry of **1** (**$1S_0$**) are shown in Table 1. This geometry is C_{2v}-symmetrical, which is clearly shown by the fact that the Pt1–N1, Pt1–N3, Pt2–N2, and Pt2–N4 bond lengths are the same (2.012 Å). The Pt1–Pt2 distance (3.451 Å) and thePt1–N1–N3–N4dihedral angle θ_1 (135.1°) are similar to those of $[Pt_2(\mu\text{-pz})_2(dfppy)_2]$ [**3**; dfppy=2-(2,4-difluorophenyl)pyridine] recently reported by Thompson et al.,[7] in which the Pt–Pt distance is 3.376 Å and the θ_1 dihedral angle is 132.6°; see Scheme 1 for the definition of θ_1. These results indicate that the geometry of **1** is mainly determined by the μ-pz ligand.

We optimized geometries of the S_1 and T_1 excited states against various Pt–Pt distances and found two equilibrium structures in these excited states: one bearing the

short Pt–Pt distance (**1S$_{1a}$** and **1T$_{1a}$** geometries) and the other bearing the long Pt–Pt distance (**1S$_{1b}$** and **1T$_{1b}$** geometries), as shown in Table 1; see the Pt–Pt distances of **1S$_{1a}$** (2.791 Å), **1T$_{1a}$** (2.777 Å), **1S$_{1b}$** (3.441 Å), and **1T$_{1b}$** (3.480 Å). All of these optimized geometries have no imaginary frequency. Interestingly, the **1S$_{1b}$** and **1T$_{1b}$** geometries are C_1-symmetrical; see the Pt1–N1, Pt1–N3, Pt2–N2, and Pt2–N4 bond lengths of 1.996, 2.020, 2.020, and 2.011 Å, respectively, in the **1S$_{1b}$** geometry and 2.009, 2.023, 2.014, and 2.009 Å, respectively, in the **1T$_{1b}$** geometry. On the other hand, the **1S$_{1a}$** and **1T$_{1a}$** geometries are C_{2v}-symmetrical; their Pt1–N1, Pt1–N3, Pt2–N2, and Pt2–N4 bond lengths are the same (2.024 Å). The **1S$_{1a}$** geometry bearing the short Pt–Pt distance is the global minimum of the S_1 state. However, the **1T$_{1b}$** geometry bearing the long Pt–Pt distance is the global minimum of the T_1 state, although the energy difference between the global and local minima is small; they are 0.16 and 0.04 eV in the S_1 and T_1 states, respectively. Previously, similar global and local minima were found in the T_1 state of **3**.[8]

In the **1S$_{1a}$** and **1T$_{1a}$** geometries, the dσ*(Pt–Pt) and π*(bpym) orbitals are singly occupied, where the dσ*(Pt–Pt) orbital mainly consists of the dσ–dσ antibonding orbital between two platinum nuclei and the π*(bpym) orbital represents the π* orbital of the bpym ligand, as shown in Figure 1. In other words, one-electron excitation occurs from the dσ*(Pt–Pt) orbital to the π*(bpym) orbital in these excited states. Thus, this electronic structure is assigned as the metal–metal-to-ligand charge-transfer (MMLCT) excited state. The same assignment was experimentally and theoretically reported for the T_1 excited state at the T_1 global minimum of **3**.[7,8] Because one-electron excitation occurs from the antibonding dσ*(Pt–Pt) orbital to the π*(bpym) orbital in these excited states, the bonding interaction between two platinum nuclei becomes stronger; note that the formal Pt-Pt bond order is 0.5 in the **1S$_{1a}$** and **1T$_{1a}$** geometries but 0.0 in the **1S$_0$** geometry. As a result, the Pt1–Pt2 distance becomes shorter and the θ_1 dihedral angle becomes smaller in the **1S$_{1a}$** and **1T$_{1a}$** geometries than in the **1S$_0$** geometry, as shown in Table 1. The other geometrical

parameters of the $\mathbf{1S_{1a}}$ and $\mathbf{1T_{1a}}$ geometries such as the Pt1−N1 distance, the N1−Pt1−N3 bond angle, and the bond distances in the bpym and pz moieties are not significantly different from those of the $\mathbf{1S_0}$ geometry; see Table 1 and Table A1 in the Appendix for these geometrical parameters.

Table 1. Several important optimized bond lengths (in Å), bond angles (in degree), dihedral angles (in degree),[a] π*(bpym), dσ*(Pt–Pt), and π(bpym) orbitals energies (in eV),[b,c] and molecular volumes (in Å^3) of **1**

	exptl valuse of a similar complex[d]	$\mathbf{1S_0}$	$\mathbf{1S_{1a}}$	$\mathbf{1S_{1b}}$	$\mathbf{1T_{1a}}$	$\mathbf{1T_{1b}}$
r(Pt1–Pt2)	3.376	3.451	2.791	3.441	2.777	3.480
r(Pt1–N1)	2.093	2.012	2.024	1.996	2.024	2.009
r(Pt1–N3)	2.071	2.012	2.024	2.020	2.024	2.023
r(Pt2–N2)	1.998	2.012	2.024	2.020	2.024	2.014
r(Pt2–N4)	2.019	2.012	2.024	2.011	2.024	2.009
r(Pt1–N5)	2.005	2.036	2.023	2.030	2.022	2.026
r(Pt1–N7)	2.021	2.036	2.023	1.996	2.022	1.976
r(Pt2–N6)	1.986	2.036	2.023	2.037	2.022	2.038
r(Pt2–N8)	2.005	2.036	2.023	2.027	2.022	2.034
a(N1–Pt1–N3)	86.1	85.3	85.4	85.9	85.3	86.3
a(N2–Pt2–N8)	84.8	85.3	85.4	85.1	85.3	85.1
a(N5–Pt1–N7)	81.6	80.1	80.6	80.9	80.5	81.5
a(N6–Pt2–N8)	81.4	80.1	80.6	80.1	80.5	80.1
d(Pt1–N1–N3–N4)[e]	132.6	135.1	118.9	137.2	118.7	136.9
d(Pt1–N3–N1–N2)	−132.3	−135.1	−118.9	−134.7	−118.7	−138.7
d(Pt2–N2–N4–N3)	−138.8	−135.1	−118.9	−132.6	−118.7	−135.1
d(Pt2–N4–N2–N1)	126.2	135.1	118.9	135.1	118.7	133.3
ε(π*(bpym))		−8.46	−8.97	−8.88	−8.99	−9.00
ε(dσ*(Pt–Pt))		−12.47	−11.73	−12.49	−11.79	−12.53
ε(π(bpym))		−13.77	−13.94	−13.76	−13.95	−13.76
molecular volume		585	606	586	604	585

(a) Geometries were optimized with the DFT(B3PW91)/basis-I method in vacuo. (b) These orbitals are shown in Figure 1. (c) Orbital energies were calculated in the S_0 state with the DFT(B3PW91)/basis-II //DFT(B3PW91)/basis-I method. (d) Experimental bond lengths, bond angles, and bond dihedral angles of **3** reported by Thompson et al. (ref 7). Note that **3** is not C_{2v} but C_s symmetrical. (e) This dihedral angle corresponds to θ_1 in Scheme 1.

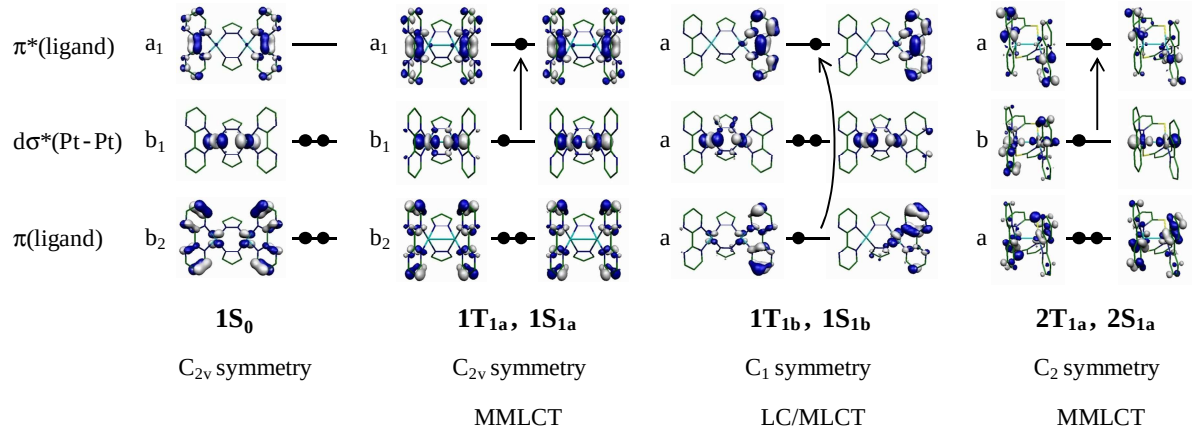

Figure 1. Several important molecular orbitals of the **1S$_0$**, **1T$_{1a}$**, **1S$_{1a}$**, **1T$_{1b}$**, **1S$_{1b}$**, **2T$_{1a}$**, and **2S$_{1a}$** geometries. Irreducible representations (a_1, b_1, b_2, a, and b) of these molecular orbitals are also represented. H atoms are omitted for brevity.

In the **1S$_{1b}$** and **1T$_{1b}$** geometries, the π(bpym) and π*(bpym) orbitals are singly occupied, as shown in Figure 1. The π(bpym) orbital somewhat interacts with the d orbital of platinum, while the π*(bpym) orbital little interacts. Thus, the electronic structures of the **1S$_{1b}$** and **1T$_{1b}$** geometries are assigned as a mixture of the ligand centered π–π* excited state and the metal-to-ligand charge transfer excited state (LC/MLCT). The same assignment was experimentally[7] and theoretically[8] reported for the local minimum geometry of the T1 excited state of **3**. As shown in Figure 1, the dσ*(Pt–Pt) orbital is doubly occupied in the **1S$_{1b}$** and **1T$_{1b}$** geometries, unlike in the **1S$_{1a}$** and **1T$_{1a}$** geometries. As a result, the dσ–dσ bonding interaction is absent in these **1S$_{1b}$** and **1T$_{1b}$** geometries, like in the **1S$_0$** geometry, leading to little changes in the Pt1–Pt2 distance and the θ_1 dihedral angle when going from the **1S$_0$** geometry to the **1S$_{1b}$** and **1T$_{1b}$** geometries, as shown in Table 1. Also, the other geometrical parameters are little different among the **1S$_{1b}$**, **1T$_{1b}$**, and **1S$_0$** geometries; see Table 1 and Table A1 in the Appendix. This means that the **1S$_{1b}$** and **1T$_{1b}$** geometries resemble well the **1S$_0$** geometry.

The differences in the electronic structure and geometry between the MMLCT (**$1S_{1a}$** and **$1T_{1a}$**) and LC/MLCT (**$1S_{1b}$** and **$1T_{1b}$**) excited states are explained in terms of dependences of the π*(bpym), dσ*(Pt–Pt), and π(bpym) orbital energies on the Pt–Pt distance. The dσ*(Pt–Pt) orbital energy becomes higher as the Pt–Pt distance becomes shorter because the antibonding overlap between the two dσ(Pt) orbitals increases with a decrease in the Pt–Pt distance; see Figure 1 for the dσ*(Pt–Pt) orbital. On the other hand, the π(bpym) and π*(bpym) orbital energies little depend on the Pt–Pt distance. Actually, the dσ*(Pt–Pt) orbital exists at much higher energy in the **$1S_{1a}$** and **$1T_{1a}$** geometries than in the **$1S_{1b}$** and **$1T_{1b}$** geometries, while the π(bpym) and π*(bpym) orbital energies are little different among the **$1S_{1a}$**, **$1S_{1b}$**, **$1T_{1a}$**, and **$1T_{1b}$** geometries; see Table 1 for the orbital energies. Thus, the energy difference between the π*(bpym) and dσ*(Pt–Pt) orbitals is much smaller in the **$1S_{1a}$** (2.76 eV) and **$1T_{1a}$** (2.80 eV) geometries than in the **$1S_{1b}$** (3.61 eV) and **$1T_{1b}$** (3.53 eV) geometries. These are the reasons why the **$1S_{1a}$** and **$1T_{1a}$** geometries bearing the short Pt–Pt

distance take the MMLCT [dσ*(Pt–Pt) → π*(bpym)] excited state but the **$1S_{1b}$** and **$1T_{1b}$** geometries bearing the long Pt–Pt distance take the LC/MLCT [π(bpym) + d(Pt) → π*(bpym)] excited state.

4.3.2. Equilibrium Geometries and Electronic Structures of [$Pt_2(\mu\text{-pyt})_2(ppy)_2$] (2) in the S_0, S_1, and T_1 States

The optimized geometry (**$2S_0$**) of **2** in the S_0 state agrees well with the experimental one,[6] as shown in Table 2, except that the Pt1–Pt2 distance (2.944 Å) is moderately longer and the Pt1–N1–S1–N2 dihedral angle θ_2 (108.3°) is moderately larger than their experimental values (2.849 Å and 105.4°); see Scheme 1 for Pt1, Pt2, N1, etc., and the definition of θ_2. It is noted that the Pt–Pt distance of **2** is much shorter than that of **1** and two Pt-ppy planes of **2** are almost parallel to each other, unlike two Pt-bpym planes of **1**; see

Scheme 1. These significant differences in the geometry between **1S$_0$** and **2S$_0$** arise from the direction of the lone-pair orbitals of the pyt and pz ligands. As shown in Figure 2, two nitrogen lone-pair orbitals of pz expand toward the outside but the nitrogen and sulfur lone-pair orbitals of pyt expand in nearly parallel fashion to each other or toward rather the inside. Optimized geometrical parameters of **2** in the S_1- and T_1-global minima (**2S$_{1a}$** and **2T$_{1a}$**) are also presented in Table 2. The Pt1–Pt2 distances of the **2S$_{1a}$** and **2T$_{1a}$** geometries are much shorter, and their θ_2 dihedral angles are much smaller than those of the **2S$_0$** geometry. These results are understood in terms of the electronic structures of the **2S$_{1a}$** and **2T$_{1a}$** geometries: SOMOs are the dσ*(Pt–Pt) and π*(ppy) orbitals in the **2S$_{1a}$** and **2T$_{1a}$** geometries, as shown in Figure 1. This means that one-electron excitation occurs from the dσ*(Pt–Pt) orbital to the π*(ppy) orbital in the **2S$_{1a}$** and **2T$_{1a}$** geometries, which leads to the presence of the Pt–Pt bonding interaction. Hence, the Pt1–Pt2 distance becomes shorter and the θ_2 dihedral angle becomes smaller in the **2S$_{1a}$** and **2T$_{1a}$** geometries than in the **2S$_0$** geometry. These S_1 and T_1 excited states of **2** are assigned as the MMLCT excited state.

The **2S$_{1a}$** and **2T$_{1a}$** geometries are similar to the **1S$_{1a}$** and **1T$_{1a}$** geometries, respectively, except that the **2S$_{1a}$** and **2T$_{1a}$** geometries are C_2-symmetrical, unlike the C_{2v}-symmetrical **1S$_{1a}$** and **1T$_{1a}$** geometries, as shown in Tables 1 and 2 and Figure 1. One important difference between **1** and **2** is that the local minimum geometry is absent in the S_1 and T_1 excited states of **2** but present in those of **1**, as discussed above. This is interpreted in terms of the lone-pair orbital of the bridging ligand. The sulfur and nitrogen lone-pair orbitals of pyt expand toward rather the inside (Figure 2), as discussed above, leading to the short Pt–Pt distance (2.944 Å) even in the S_0 ground state. Because the LC/MLCT excited state is possible when the Pt–Pt distance is long, the LC/MLCT excited state cannot be formed in **2**. A similar feature is observed in **3**; the T_1 local minimum of the LC/MLCT state bearing the long Pt–Pt distance cannot be formed in **3** when bulky substituents are introduced to the pz ligand, as reported previously,[7,8] because the bulky substituents decrease the Pt–Pt distance.

On the basis of these results, it is concluded that the pyt ligand plays a role to decrease the Pt–Pt distance, like the pz ligand bearing a bulky substituent in **3**.

Table 2. Several important optimized bond lengths (in Å), bond angles (in degree), dihedral angles (in degree),[a] π*(ppy), dσ*(Pt–Pt), and π(ppy) orbitals energies (in eV),[b,c] and molecular volumes (in Å^3) of **2**

	exptl[d]	**2S$_0$**	**2S$_{1a}$**	**2T$_{1a}$**
r(Pt1–Pt2)	2.849	2.994	2.680	2.675
r(Pt1–N1)	2.142	2.180	2.194	2.194
r(Pt2–N2)	2.142	2.180	2.194	2.194
r(Pt1–N3)	2.038	2.061	2.052	2.050
r(Pt2–N4)	2.036	2.061	2.052	2.050
r(Pt1–S1)	2.284	2.316	2.330	2.331
r(Pt2–S2)	2.284	2.316	2.330	2.331
r(Pt1–C3)	1.987	1.992	1.998	1.997
r(Pt2–C4)	1.983	1.992	1.998	1.997
a(N1–Pt1–S1)	90.4	88.4	88.1	88.0
a(N2–Pt2–S2)	90.3	88.4	88.1	88.0
a(N3–Pt1–C3)	81.1	80.7	81.0	81.0
a(N4–Pt2–C4)	81.3	80.7	81.0	81.0
d(Pt1–N1–S1–N2)[e]	105.4	108.3	103.8	103.7
d(Pt2–N2–S2–N1)	106.3	108.3	103.8	103.7
ε(π*(ppy))		–1.72	–1.84	–1.84
ε(dσ*(Pt–Pt))		–4.72	–4.37	–4.36
ε(π(ppy))		–6.52	–6.37	–6.37
molecular volume		712	698	697

(a) Geometries were optimized with the DFT(B3PW91)/basis-I method in vacuo. (b) These orbitals are shown in Figure 1. (c) Orbital energies were calculated in the S_0 state with the DFT(B3PW91)/basis-II //DFT(B3PW91)/basis-I method. (d) Reference 6. (e) This dihedral angle corresponds to θ_2 in Scheme 1.

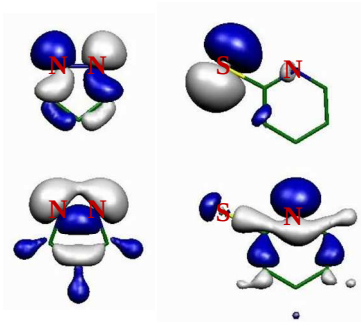

pz pyp

Figure 2. Lone-pair orbitals of pz and pyt. H atoms are omitted for brevity.

4.3.3. S_0, T_1, and S_1 PECs of 1 and 2

The PECs of the S_0, S_1, and T_1 states of **1** are evaluated as a function of the Pt–Pt distance in vacuo, as shown in Figure 3a, where the geometry was optimized at each Pt–Pt distance with the B3PW91/basis-I method. In the S_1 and T_1 PECs, a small but nonnegligible barrier exists around the Pt–Pt distance of 3 Å. The S_1 and T_1 states take the MMLCT excited state in the Pt–Pt distance shorter than 3 Å and the LC/MLCT excited state in the Pt–Pt distance longer than 3 Å.

The energy difference is very small (0.02 eV) between the $\mathbf{1S_{1a}}$ and $\mathbf{1T_{1a}}$ geometries but somewhat large (0.22 eV) between the $\mathbf{1S_{1b}}$ and $\mathbf{1T_{1b}}$ geometries. These results are interpreted in terms of the exchange integral, as follows: The energy difference between the S_1 and T_1 states is approximately represented by twice the exchange integral, when the molecular orbitals are not very different between these two states:[23]

$$E(S_1) - E(T_1) \approx 2(XY|YX) \qquad (1)$$

where $E(S_1)$ and $E(T_1)$ are the energies of the S_1 and T_1 states, respectively, X and Y are SOMOs of the S_1 and T_1 states, and (XY|YX) is an exchange integral. In general, the exchange integral becomes large when the SOMOs (X and Y) are localized in one moiety. In the $\mathbf{1S_{1b}}$ and $\mathbf{1T_{1b}}$ geometries, the SOMOs are localized on the right-hand side of the

molecule, as shown in Figure 1. In the **1S$_{1a}$** and **1T$_{1a}$** geometries, on the other hand, the SOMOs are delocalized on the whole molecule. As a result, the energy difference between the **1S$_{1a}$** and **1T$_{1a}$** geometries is smaller than that between the **1S$_{1b}$** and **1T$_{1b}$** geometries.

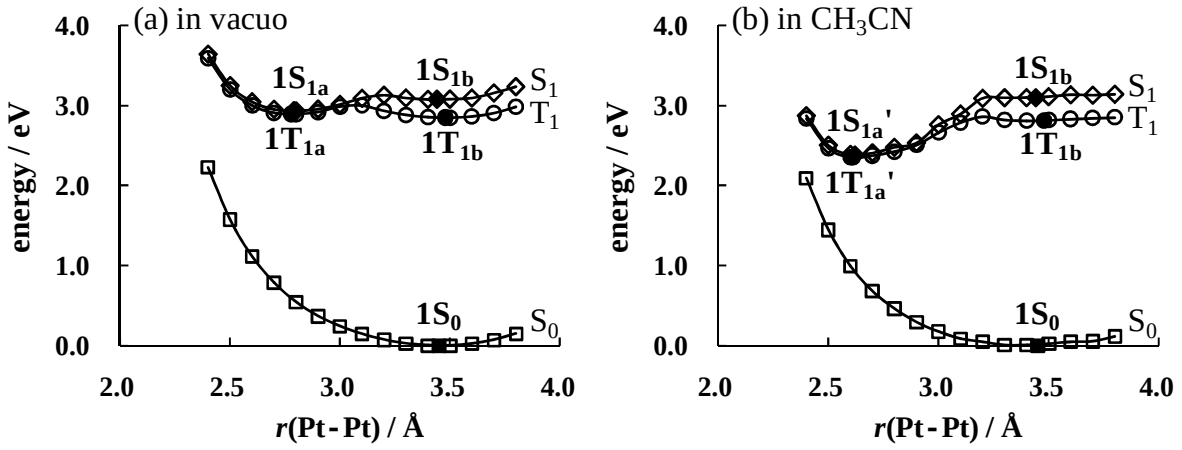

Figure 3. PECs of the S_0, T_1, and S_1 states of **1** vs the Pt–Pt distance. Geometries were optimized with the DFT(B3PW91)/basis-I method at each Pt–Pt distance. It is noted that the energy difference between the T_1- and S_0-curves does not correspond to the energy of phosphorescence because the T_1 curve represents the energy of the T_1-optimized geometry and the S_0-curve represents the energy of the S_0-optimized geometry. The energy of phosphorescence corresponds to the energy difference between the T_1 and S_0 states at the T_1-optimized geometry.

The S_0, T_1, and S_1 PECs of **1** were reevaluated in the CH_3CN solution by the PCM method at the B3PW91/basis-I level, where the optimized geometries in vacuo were employed. Although the ^{3}MMLCT-optimized geometry (**1T$_{1a}$**) is slightly more unstable than the ^{3}LC/MLCT-optimized geometry (**1T$_{1b}$**) in vacuo (Figure 3a), the former is considerably more stable than the latter in the CH_3CN solution, as shown in Figure 3b. To elucidate the reason of this solvent effect, we will examine here how much polarization occurs in the MMLCT and LC/MLCT excited states. The LC/MLCT state mainly consists of localized π–π* excitation in one bpym and moderate CT excitation from the Pt–pz moiety

to bpym in one pz–Pt–bpym moiety, as shown in Figure 1. On the other hand, the MMLCT state consists of CT excitation in two pz–Pt–bpym moieties. These features of the MMLCT and LC/MLCT states are consistent with the Mulliken charges of the $\mathbf{1T_{1a}}$, $\mathbf{1T_{1b}}$, and $\mathbf{1S_0}$ geometries. In the $\mathbf{1T_{1b}}$ geometry, the Pt1 atom is somewhat and the pz(N1^N2) is moderately more positively charged (+0.10 and +0.06, respectively) than those in the $\mathbf{1S_0}$ geometry, as shown in Table 3, where the pz(N1^N2) means the pz ligand including N1 and N2 atoms. Consistent with these Mulliken charges, the bpym(N6^N8) is much more negatively charged (–0.19) in the $\mathbf{1T_{1b}}$ geometry than in the $\mathbf{1S_0}$ geometry. On the other hand, the Mulliken charges of the Pt2 atom, pz(N3^N4), and bpym(N5^N7) are little different between the $\mathbf{1T_{1b}}$ and $\mathbf{1S_0}$ geometries. In the $\mathbf{1T_{1a}}$ geometry, two Pt atoms and two pz ligands are much more positively charged (+0.10 and +0.11) and two bpym ligands are much more negatively charged (–0.21) than those in the $\mathbf{1S_0}$ geometry. These results indicate that CT more likely occurs in the MMLCT state than in the LC/MLCT state, leading to the formation of a more polarized electron distribution in the MMLCT excited state than in the LC/MLCT state. As a result, the MMLCT state is more stabilized by the polar CH_3CN solvent than the LC/MLCT state. This is the main reason why the $\mathbf{1T_{1a}}$ geometry becomes a global minimum in the CH_3CN solution. In the S_1 excited state, the ^{1}MMLCT state is also much more stabilized by theCH_3CNsolution than the ^{1}LC/MLCT state, like in the T_1 states, as shown in Figure 3b.

It should be noted that the Mulliken charges change much more in the CH_3CN solution than in vacuo when going from the $\mathbf{1S_0}$ geometry to the $\mathbf{1S_{1a}}$ and $\mathbf{1T_{1a}}$ geometries, as shown in Table 3; for example, the Mulliken charge of Pt1 increases by +0.16 in the CH_3CN solution but by +0.10 in vacuo when going from the $\mathbf{1S_0}$ geometry to the $\mathbf{1S_{1a}}$ and $\mathbf{1T_{1a}}$ geometries. This means that the CH_3CN solvent accelerates CT from the Pt moiety to the π^* of bpym in the MMLCT excited state. As a result, MMLCT excitation decreases more the electron density of the $d\sigma^*$(Pt–Pt) orbital in the CH_3CN solution than in vacuo, which

decreases more the Pt–Pt distances of the ^{1}MMLCT and ^{3}MMLCT excited states to 2.620 and 2.610 Å, respectively, in the CH_3CNsolution than in vacuo, as shown in Figure 2b. These equilibrium geometries in the CH_3CN solution are named as **$1S_{1a}$'** and **$1T_{1a}$'** hereafter.

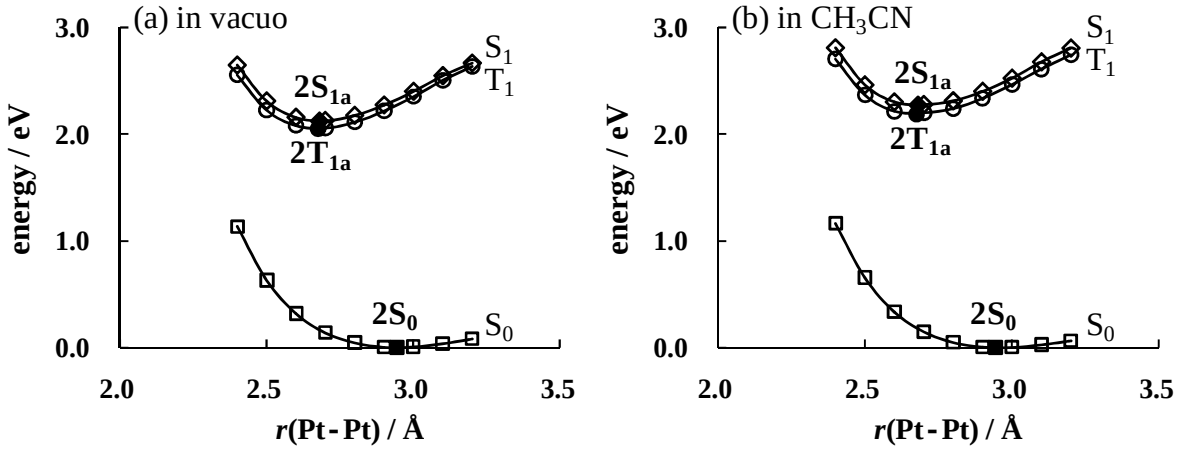

Figure 4. PECs of the S_0, T_1, and S_1 states of **2** vs the Pt–Pt distance. Geometries were optimized with the DFT(B3PW91)/basis-I method at each Pt–Pt distance. It is noted that the energy difference between the T_1- and S_0-curves does not correspond to the energy of phosphorescence because the T_1 curve represents the energy of the T_1-optimized geometry and the S_0 curve represents the energy of the S_0-optimized geometry. The energy of phosphorescence corresponds to the energy difference between the T_1 and S_0 states at the T_1-optimized geometry.

The S_0-, T_1-, and S_1-PECs of **2** are shown in Figures 4a and 4b. Only the global minimum exists in the S_1 and T_1 PECs of **2**, but no local minimum exists in these excited states, as mentioned above. The same names, **$2S_{1a}$** and **$2T_{1a}$**, are employed for these global minimum geometries in both vacuo and the CH_3CNsolution, because these geometries in the CH_3CN solution are almost the same as those in vacuo, unlike the **$1S_{1a}$** and **$1T_{1a}$** geometries; for instance, the Pt–Pt distance is 2.680 and 2.675 Å for the **$2S_{1a}$** and **$2T_{1a}$** geometries, respectively, in both vacuo and the CH_3CN solution; see Table 2 and Figure 4.[24]

Table 3. Changes of the Mulliken Charges when going from the S_0-optimized geometry to the S_1- or T_1-optimized geometries of **1** and **2**

	Pt1	Pt2	pz(N1^N2)	pz(N3^N4)	bpym(N5^N7)	bpym(N6^N8)
in vacuo						
$1S_{1a}$	+0.10	+0.10	+0.11	+0.11	–0.21	–0.21
$1T_{1a}$	+0.10	+0.10	+0.11	+0.11	–0.21	–0.21s
$1S_{1b}$	+0.10	+0.01	+0.07	+0.02	+0.02	–0.22
$1T_{1b}$	+0.01	+0.01	+0.06	+0.01	+0.01	–0.19
in CH_3CN						
$1S_{1a}$	+0.16	+0.16	+0.10	+0.10	–0.26	–0.26
$1T_{1a}$	+0.16	+0.16	+0.10	+0.10	–0.26	–0.26
$1S_{1a}'$	+0.17	+0.17	+0.10	+0.10	–0.27	–0.27
$1T_{1a}'$	+0.17	+0.17	+0.10	+0.10	–0.27	–0.27
$1S_{1b}$	+0.11	+0.02	+0.12	+0.04	+0.02	–0.31
$1T_{1b}$	+0.13	+0.01	+0.10	+0.02	+0.02	–0.28
	Pt1	Pt2	thp(N1^S2)	thp(N2^S1)	ppy(N3^C3)	ppy(N4^C4)
in vacuo						
$2S_{1a}$	+0.05	+0.05	+0.09	+0.09	–0.14	–0.14
$2T_{1a}$	+0.04	+0.04	+0.09	+0.09	–0.13	–0.13
in CH_3CN						
$2S_{1a}$	+0.10	+0.10	+0.10	+0.10	–0.20	–0.20
$2T_{1b}$	+0.09	+0.09	+0.10	+0.10	–0.19	–0.19

(a) pz(N1^N2) means the pz ligand including N1 and N2 atoms; see Scheme 1.

4.3.4. Reasons Why the Phosphorescence Spectrum of 1 Is Observed in the Solid State but Not in the CH_3CN Solution

In **1**, $S_0 \rightarrow S_1$ photoexcitation occurs at 3.50 eV (353 nm).[5] This excitation energy is evaluated to be 3.39 eV as the energy difference between the S_0 and S_1 states at the S_0 equilibrium geometry. This $S_0 \rightarrow S_1$ photoexcitation yields the S_1 state, with the S_0 equilibrium geometry (**$1S_0$**) due to the Franck–Condon principle. It is likely that the geometry of the S_1 state changes to the C_{2v}-symmetrical global minimum **$1S_{1a}'$** geometry in CH_3CN, because the CH_3CN solution is flexible enough not to suppress the geometry

change. The electronic structure of the S_1 state changes from the LC/MLCT state to the MMLCT one when going from the **1S$_0$** geometry to the **1S$_{1a}$'** one. In the **1S$_{1a}$'** geometry, spin–orbit interaction between the S_1 and T_1 excited states is absent because the direct product of irreducible representations of the SOMOs of these excited states and the orbital angular momentum operator (*l*) does not belong to the a_1 representation in the C_{2v}-symmetrical **1S$_{1a}$'** geometry; see the Appendix for details. Thus, the $S_1 \rightarrow T_1$ intersystem crossing hardly occurs in the **1S$_{1a}$'** geometry. As a result, the population of the T_1 state is absent and the phosphorescence of **1** cannot occur in the CH_3CN solution.

Although the $S_1 \rightarrow T_1$ intersystem crossing is considered to hardly occur, the fluorescence of **1** was not experimentally observed in the CH_3CN solution.[5] This means that the $S_1 \rightarrow S_0$ non-radiative decay occurs; if not, the $S_1 \rightarrow S_0$ fluorescence spectrum must be observed. We will briefly discuss here the reason why the $S_1 \rightarrow S_0$ non-radiative decay occurs around the S_1 global minimum geometry (**1S$_{1a}$'**) in the CH_3CN solution. The energy difference between the S_1 and S_0 states is evaluated to be small (1.33 eV) at the **1S$_{1a}$'** geometry with the PCM method. This energy difference becomes much smaller than 1.33 eV as the Pt–Pt distance becomes shorter than the equilibrium distance of **1S$_{1a}$'** (2.620 Å), as shown in Figure 3b. Because the Pt–Pt distance would become shorter by molecular vibration and/or geometry fluctuation around **1S$_{1a}$'**, it is likely that the $S_1 \rightarrow S_0$ non-radiative transition occurs in the CH_3CN solution at RT. We discuss the reason why the shortening of the Pt–Pt distance leads to a decrease in the energy difference between the S_1 and S_0 states. The dσ*(Pt–Pt) orbital energy becomes higher as the Pt–Pt distance becomes shorter, as discussed above. Because the dσ*(Pt–Pt) orbital is doubly occupied in the S_0 state but singly occupied in the S_1 state, the S_0 state becomes more unstable in energy than the S_1 state as the Pt–Pt distance becomes shorter. Hence, the energy difference between the S_1 and S_0 states becomes small with a decrease in the Pt–Pt distance.

Here, we discuss whether the $T_1 \rightarrow S_0$ emission is allowed or forbidden; this

discussion is necessary because forbidden phosphorescence is not observed at all even if the $S_1 \rightarrow T_1$ intersystem crossing occurs. The $T_1 \rightarrow S_0$ transition occurs when some of the singlet excited states mix into the T_1 state through spin-orbit interaction. As discussed above, spin–orbit interaction between the S_1 and T_1 states is absent at the **$1T_{1a}$'** geometry. Thus, the $S_1 \rightarrow S_0$ transition does not contribute to the oscillator strength of the $T_1 \rightarrow S_0$ emission. On the other hand, the S_2 state mixes into the T_1 state by spin–orbit interaction.[25a] The oscillator strength of the $S_2 \rightarrow S_0$ transition is moderate, which is evaluated to be 0.0170 by time-dependent (TD)-B3PW91 with the PCM method.[25b] Singlet excited states with higher energy than the S_2 state mix less into the T_1 state because the energy difference between the higher energy singlet excited state and the T_1 state is large. In conclusion, the $T_1 \rightarrow S_0$ emission is not forbidden mainly because of mixing of the S_2 state into the T_1 state, indicating that phosphorescence is observed in CH_3CN if the population of the T_1 state is present.

Another issue to be discussed here is whether or not the $S_1 \rightarrow T_1$ intersystem crossing occurs around the S_0 geometry (**$1S_0$**) before geometry relaxation to the global minimum. Actually, the rapid intersystem crossing is observed in some platinum(II) complexes.[26] The S_1 state is C_1-symmetrical around the **$1S_0$** geometry, as shown in Figure 1, in which spin–orbit interaction between the S_1 and T_1 excited states operates to induce the $S_1 \rightarrow T_1$ intersystem crossing; see the Appendix for details. After this intersystem crossing, the geometry changes to the T_1 global minimum (**$1T_{1a}$'**). The energy difference between the T_1 and S_0 states is small (1.24 eV) at the **$1T_{1a}$'** geometry, as discussed above about the **$1S_{1a}$'** geometry; see also Table 4. Thus, it is likely that the $T_1 \rightarrow S_0$ non-radiative decay occurs at the **1T1a'** geometry; in other words, **1** would not be emissive in the CH_3CN solution even though the $S_1 \rightarrow T_1$ intersystem crossing occurs before the geometry change to the **$1S_{1a}$'** geometry in the S_1 state.

Table 4. Energies (in eV)[a] and assignments of phosphorescence spectra of **1** and **2**

		energy of phosphorescence			
		calcd			
geometry	assignment	vacuo	CH_3CN	exptl[b]	
$\mathbf{1T_{1a}}'$	π*(bpym) → dσ*(Pt–Pt)	1.66	1.22	*c*	CH_3CN at RT
$\mathbf{1T_{1b}}$	π*(bpym) → dσ*(Pt–Pt)	2.33	2.28	2.41, 2.59, 2.73	solid state at RT
$\mathbf{2T_{1a}}$	π*(ppy) → dσ*(Pt–Pt)	1.75	1.87	1.89	CH_3CN at RT
				1.93	solid state at RT

(a) The energy of phosphorescence is defined as the energy difference between the T_1 and S_0 states at the T_1-optimized geometry. This energy difference was evaluated with the DFT(B3PW91)/basis-II //DFT(B3PW91)/basis-I method. (b) See refs 5 and 6 for complexes **1** and **2**, respectively. (c) Phosphorescene was not observed. (d) The peak of the phosphorescence spectrum was split. See ref 27.

In the solid state, the phosphorescence of **1** is experimentally observed at 2.41, 2.59, and 2.73 eV at RT.[5,27] The reason why **1** is emissive in the solid state is considerably interesting. The $S_0 \rightarrow S_1$ excitation occurs at the S_0-equilibrium geometry (**$1S_0$**), like in the CH_3CN solution. However, it is likely that the geometry of the S_1 state does not change to the S_1 global minimum (**$1S_{1a}$**) in the solid state, unlike in the CH_3CN solution. One reason is that the molecular volume considerably changes when going from the **$1S_0$** geometry to the **$1S_{1a}$**; note that the molecular volume is much different between the **$1S_{1a}$** (606 $Å^3$) and **$1S_0$** (585 $Å^3$) geometries, as shown in Table 1. Such a large volume change is difficult in the solid state. Another reason is that there is a small but non-negligible activation barrier between the **$1S_{1a}$** and **$1S_{1b}$** geometries in the S_1-PEC, as shown in Figure 3a. This activation barrier would suppress the geometry change from **$1S_{1b}$** to **$1S_{1a}$** in the solid state; hence, the geometry of the S_1 state would stay in the local minimum geometry (**$1S_{1b}$**) in the solid state. In the C_1-symmetrical **$1S_{1b}$** geometry, spin–orbit interaction between the T_1 and S_1 states operates to induce the $S_1 \rightarrow T_1$ intersystem crossing because the direct product of the irreducible representations of the SOMOs in these excited states and the *l* operator

belongs to the "a" representation; see the Appendix for details. The geometry of the T_1 excited state would change to the **$1T_{1b}$** geometry even in the solid state because the molecular volume little changes in this case; the molecular volumes of the **$1S_{1b}$** and **$1T_{1b}$** geometries are almost the same and are 586 and 585 $Å^3$, respectively, as shown in Table 1. Thus, the population of the T_1 state would be present, and $T_1 \rightarrow S_0$ phosphorescence occurs at the **$1T_{1b}$** geometry. This phosphorescence is allowed because the S_1 state mixes into the T_1 state by spin–orbit coupling, and the $S_0 \rightarrow S_1$ transition is symmetry-allowed. The energy of this phosphorescence corresponds to the energy difference between the T_1 and S_0 states at the **$1T_{1b}$** geometry, which is evaluated to be 2.33 eV, as shown in Table 4. This value agrees well with the experimental value (2.41, 2.59, and 2.73 eV).[5,27] The phosphorescence in the solid state is assigned as the π^*(bpym) $\rightarrow$ π(bpym) + d(Pt) transition.

At the end of this section, we mention the comparison between **1** and **3** because **3** is emissive in a 2-methyltetrahydrofuran (2-MeTHF) solution, unlike **1** in a CH_3CN solution. It is likely that the geometries of the S_1 and T_1 states of **3** are C_s-symmetrical in solution.[8] In this geometry, S_1–T_1 spin–orbit interaction operates to induce the $S_1 \rightarrow T_1$ intersystem crossing. Thus, the population of the T_1 state of **3** is not zero and the $T_1 \rightarrow S_0$ emission of **3** is observed in 2-MeTHF. This is the reason why **3** is emissive in solution, although its geometry and electronic structure are similar to those of **1**.

4.3.5. Reasons Why the Phosphorescence Spectrum of 2 Is Observed in Both the Solid State and theCH_3CN Solution

Photo-excitation occurs at 2.47 eV (500 nm) in the CH_3CN solution at RT.[6] The energy difference between the S_0 and S_1 states is evaluated to be 2.33 eV at the S_0 equilibrium geometry (**$2S_0$**). This value agrees well with the experimental excitation energy. The geometry of the S_1 state is the same as the **$2S_0$** geometry just after photo-excitation

according to the Franck–Condon principle. It is likely that the geometry changes to the S_1 global minimum (**2S$_{1a}$**) in the CH_3CN solution. The **2S$_{1a}$** geometry is C_2-symmetrical and its electronic structure is the MMLCT excited state, as shown in Figure 1. Because the direct product of the irreducible representations of the SOMOs and the *l* operator belongs to the "a" representation in the C_2 symmetry, spin–orbit interaction between the S_1 and T_1 excited states operates to induce the $S_1 \rightarrow T_1$ intersystem crossing; see the Appendix for details. Then, the geometry of **2** would change to the T_1 global minimum (**2T$_{1a}$**), in which phosphorescence would occur from the T_1 excited state to the S_0 ground state. The energy of this phosphorescence is evaluated to be 1.87 eV with the PCM method, as shown in Table 4. This value agrees well with the experimental one (1.89 eV).[6] This phosphorescence is assigned as the π^*(ppy) $\rightarrow$ dσ^*(Pt–Pt) transition.[28]

It is likely that even in the solid state geometry relaxation occurs from the **2S$_0$** geometry to the **2S$_{1a}$** one, like in the CH_3CNsolution, because no barrier exists between the **2S$_0$** and **2S$_{1a}$** geometries, as discussed above. Another reason is that the molecular volume changes less when going from the **2S$_0$** (712 Å^3) geometry to the **2S$_{1a}$** (698 Å^3) geometry than when going from the **1S$_0$** geometry to the **1S$_{1a}$** geometry, as shown in Table 2. In the C_2-symmetrical **2S$_{1a}$** geometry, the $S_1 \rightarrow T_1$ intersystem crossing occurs, followed by geometry relaxation to the **2T$_{1a}$** geometry on the T_1-PEC. Thus, the population of the T_1 state is present; hence, $T_1 \rightarrow S_0$ phosphorescence occurs at the **2T$_{1a}$** geometry in the solid state; note that this phosphorescence is allowed because the S_1 state mixes into the T_1 state through spin–orbit interaction and the $S_1 \rightarrow S_0$ transition is allowed. The energy of this phosphorescence is calculated to be 1.75 eV, as shown in Table 4. This energy agrees well with the experimental value (1.93 eV)[6] observed in tne solid state.

We discuss here the reason why the energy of phosphorescence of **2** is similar between in the solid state and the CH_3CN solution. The important result is that the local minimum is absent in the T_1-PEC of **2**. Another important factor is the moderate change in the

molecular volume when going from the **2S$_0$** geometry to the **2T$_{1a}$** geometry. Thus, the T_1 geometry of **2** reaches almost the same global minimum geometry (**2T$_{1a}$**) in both the solid state and the CH_3CN solution, leading to the similar energy of phosphorescence of **2** between the solid state and the CH_3CN solution. In **1**, on the other hand, the T_1 geometry still exists at the T_1-local minimum in the solid state but changes to the T_1-global minimum in a CH_3CN solution, as discussed above.

This difference between **1** and **2** arises from the different direction of the lone-pair orbitals between pz and pyt; as discussed above, the nitrogen and sulfur lone-pair orbitals of pyt expand toward rather the inside, as shown in Figure 2, while nitrogen lone-pair orbitals of pz expand toward the outside. As a result, the geometry bearing the long Pt–Pt distance can be formed in **1** but not in **2**. This is one of the important factors for the different features between **1** and **2**.

4.4. Conclusions

In the S_1-PEC of **1**, both global (**1S$_{1a}$**) and local (**1S$_{1b}$**) minimum geometries are present. The **1S$_{1b}$** geometry is similar to the S_0-equilibrium geometry (**1S$_0$**), but the **1S$_{1a}$** geometry is considerably different. The S_1 state of **1** takes the **1S$_{1b}$** geometry in the solid state because the geometry changes from the **1S$_0$** geometry to the **1S$_{1a}$** one with difficulty in the solid state. Spin–orbit interaction between the T_1 and S_1 states operates in this C_1-symmetrical **1S$_{1b}$** geometry to induce the $S_1 \rightarrow T_1$ intersystem crossing. Then, the geometry moderately changes to the ^{3}LC/MLCT-minimum geometry (**1T$_{1b}$**), in which π^*(bpym) $\rightarrow$ π(bpym) + d(Pt) phosphorescence occurs. In the CH_3CN solution, the S_1 geometry of **1** reaches the S_1 global minimum (**1S$_{1a}$'**) concomitantly with a change of the electronic structure from the ^{1}LC/MLCT state to the ^{1}MMLCT state. Because of the C_{2v}-symmetrical **1S$_{1a}$'** geometry, spin–orbit interaction between the T_1 and S_1 states is absent not to induce the $S_1 \rightarrow T_1$ intersystem crossing. Also, the S_1 excited state of **1**

non-radiatively decays to the S_0 ground state because of the small energy difference (1.33 eV) between the S_1 and S_0 states at the **1S$_{1a}$'** geometry. Thus, both phosphorescence and fluorescence of **1** are not observed in the CH_3CN solution at RT. There is a possibility that the $S_1 \rightarrow T_1$ intersystem crossing occurs before geometry relaxation to the **1S$_{1a}$'** geometry. Even in this case, $T_1 \rightarrow S_0$ phosphorescence is not observed in CH_3CN, too, because the $T_1 \rightarrow S_0$ non-radiative decay would easily occur because of the small energy difference between the T_1 and S_0 states at the T_1-global minimum geometry (**1T$_{1a}$'**) in CH_3CN.

In the S_1-PEC of **2**, the local minimum is absent and the molecular volume does not change very much when going from the S_0 equilibrium geometry (**2S$_0$**) to the S_1-global minimum geometry (**2S$_{1a}$**). Hence, the S_1 geometry of **2** changes to the **2S$_{1a}$** geometry in both the solid state and the CH_3CN solution. Because the **2S$_{1a}$** geometry is C_2-symmetrical, spin–orbit interaction operates to induce the $S_1 \rightarrow T_1$ intersystem crossing. Thus, the population of the T_1 state is present; hence, π^*(ppy) $\rightarrow$ dσ^*(Pt–Pt) phosphorescence occurs at the **2T$_{1a}$** geometry in both the solid state and the CH_3CN solution. The direction of lone-pair orbitals of the bridging ligand and the symmetry of the chelating ligand are responsible for these differences between **1** and **2**.

4.5. Appendix

Table A1. Several important optimized bond lengths (in Å)[a] in pz and bpym of **1**

		$\mathbf{1S_0}$	$\mathbf{1S_{1a}}$	$\mathbf{1S_{1b}}$	$\mathbf{1T_{1a}}$	$\mathbf{1T_{1b}}$
pz	*r*(N1–N2)[b]	1.354	1.351	1.356	1.350	1.356
	r(N1–C1)	1.348	1.345	1.349	1.345	1.348
	r(C1–C5)	1.391	1.394	1.392	1.394	1.391
bpym	*r*(N5–C7)	1.345	1.352	1.346	1.352	1.342
	r(C7–C11)	1.387	1.378	1.382	1.378	1.387
	r(C11–C15)	1.395	1.409	1.408	1.409	1.415
	r(C15–N9)	1.335	1.325	1.321	1.325	1.319
	r(N9–C19)	1.317	1.328	1.328	1.327	1.336
	r(C19–N5)	1.358	1.376	1.379	1.375	1.389
	r(C19–C21)	1.480	1.450	1.446	1.451	1.439

(a) Geometries were optimized with the DFT(B3PW91)/basis-I method. (b) Labels of atoms are represented in Scheme A1.

Scheme A1.

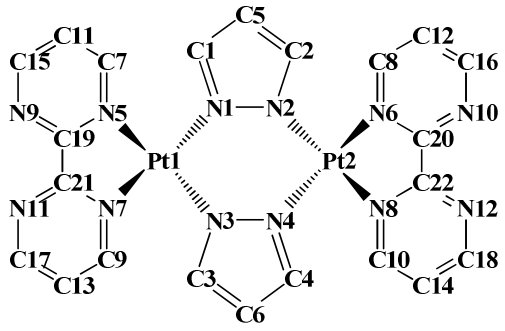

Table A2. Several important optimized bond lengths (in Å)[a] in thp and ppy of **1**

		exptl[b]	$\mathbf{2S_0}$	$\mathbf{2S_{1a}}$	$\mathbf{2T_{1a}}$
thp	*r*(N1–C1)[c]	1.335	1.356	1.353	1.352
	r(C1–S2)	1.747	1.745	1.743	1.742
	r(N1–C5)	1.360	1.351	1.349	1.349
	r(C5–N7)	1.367	1.351	1.349	1.349
	r(C7–C9)	1.411	1.400	1.401	1.401
	r(C9–C11)	1.361	1.381	1.381	1.381
	r(C11–C1)	1.398	1.414	1.412	1.412
ppy	*r*(N3–C13)	1.330	1.342	1.353	1.353
	r(C13–C15)	1.390	1.386	1.377	1.377
	r(C15–C17)	1.398	1.395	1.409	1.408
	r(C17–C19)	1.308	1.386	1.385	1.385
	r(C19–C21)	1.405	1.400	1.399	1.399
	r(C21–N3)	1.369	1.363	1.381	1.381
	r(C21–C23)	1.471	1.457	1.445	1.445
	r(C23–C25)	1.400	1.402	1.406	1.406
	r(C25–C27)	1.338	1.388	1.386	1.386
	r(C27–C29)	1.422	1.397	1.400	1.400
	r(C29–C31)	1.338	1.394	1.394	1.393
	r(C31–C3)	1.411	1.403	1.399	1.400
	r(C3–C23)	1.421	1.420	1.424	1.424

(a) Geometries were optimized with the DFT(B3PW91)/basis-I method. (b) Reference 6. (c) Labels of atoms are represented in Scheme A2.

Scheme A2.

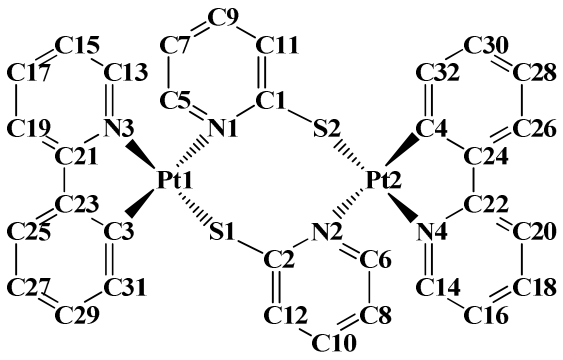

Table A3. Evaluated orbital energies (in eV)

	$\mathbf{1S_0}$	$\mathbf{1S_{1a}}$	$\mathbf{1S_{1b}}$	$\mathbf{1T_{1a}}$	$\mathbf{1T_{1b}}$
B3PW91/basis-I//B3PW91/basis-I					
$\varepsilon(\pi^*(\text{bpym}))$	–8.40	–8.90	–8.83	–8.92	–8.94
$\varepsilon(d\sigma^*(\text{Pt–Pt}))$	–12.14	–11.72	–12.22	–11.70	–12.13
$\varepsilon(\pi(\text{bpym}))$	–13.18	–13.19	–13.10	–13.19	–13.11
B3PW91/basis-II//B3PW91/basis-I					
$\varepsilon(\pi^*(\text{bpym}))$	–8.46	–8.97	–8.88	–8.99	–9.00
$\varepsilon(d\sigma^*(\text{Pt–Pt}))$	–12.47	–11.73	–12.49	–11.79	–12.53
$\varepsilon(\pi(\text{bpym}))$	–13.77	–13.94	–13.76	–13.95	–13.76
	$\mathbf{2S_0}$	$\mathbf{2S_{1a}}$	$\mathbf{2T_{1a}}$		
B3PW91/basis-I//B3PW91/basis-I					
$\varepsilon(\pi^*(\text{ppy}))$	–1.56	–1.68	–1.68		
$\varepsilon(d\sigma^*(\text{Pt–Pt}))$	–4.61	–4.27	–6.23		
$\varepsilon(\pi(\text{ppy}))$	–6.42	–6.22	–6.23		
B3PW91/basis-II//B3PW91/basis-I					
$\varepsilon(\pi^*(\text{ppy}))$	–1.72	–1.84	–1.84		
$\varepsilon(d\sigma^*(\text{Pt–Pt}))$	–4.71	–4.37	–4.36		
$\varepsilon(\pi^*(\text{ppy}))$	–6.52	–6.37	–6.37		

Table A4. Evaluated energies (in eV) and assignments of phosphorescence spectra of **1** and **2**

			energy of phosphirescence	
geometry	assignment		vacuo	CH_3CN
B3PW91//basis-I//B3PW91/basis-I				
$\mathbf{1T_{1a}'}$	π^*(bpym)	→ π(bpym) + d(Pt)	1.73	1.29
$\mathbf{1T_{1b}}$	π^*(bpym)	→ $d\sigma^*$(Pt–Pt)	2.35	2.30
$\mathbf{2T_{1a}}$	π^*(ppy)	→ $d\sigma^*$(Pt–Pt)	1.81	1.94
B3PW91/basis-II//B3PW91/basis-I				
$\mathbf{1T_{1a}'}$	π^*(bpym)	→ π(bpym) + d(Pt)	1.66	1.22
$\mathbf{1T_{1b}}$	π^*(bpym)	→ $d\sigma^*$(Pt–Pt)	2.33	2.28
$\mathbf{2T_{1a}}$	π^*(ppy)	→ $d\sigma^*$(Pt–Pt)	1.75	1.87

Discussion about the spin–orbit interaction between the T_1 and S_1 states based on the symmetry of the electronic structure

The spin–orbit interaction between the triplet and singlet excited states is one of the most important factors to induce the phosphorescence in transition metal complexes. If the spin–orbit interaction is very small, the intersystem crossing from the singlet excited state to the triplet excited state hardly occurs. In such case, the population of the triplet state is absent, and hence, the phosphorescence does not occur. Here, we will discuss the spin–orbit interactions between the T_1 and S_1 states of **1** and **2** and between the T_1 and S_2 states of **1**.

The spin–orbit interaction between the T_1 and S_1 states is approximately represented by the spin–orbit matrix elements.

$$\text{(spin–orbit matrix elements)} = \left\langle \Psi_{T_1,m} \middle| H_{SO} \middle| \Psi_{S_1,0} \right\rangle \tag{A1}$$

In eq A1, $\Psi_{T1,m}$ and $\Psi_{S1,0}$ are wavefunctions of the T_1 and S_1 states, respectively, and the subscript "*m*" represents the *z*-component of the spin angular momentum (m = +1, 0, –1). In this study, the spin–orbit Hamiltonian (H_{SO}) is represented by one-electron term of the Breit–Pauli Hamiltonian, which is defined below:

$$H_{SO} = \frac{\alpha^2}{2} \sum_{A}^{nuclear} \sum_{j}^{electron} \frac{Z_A}{r_{A\,j}^3} \, \boldsymbol{l}_{\mathbf{A}j} \cdot \boldsymbol{s}_j \tag{A2}$$

where α is the fine-structure constant, r is the distance between nucleus A and electron j, $\boldsymbol{l}$ and $\boldsymbol{s}$ are the orbital and spin angular momentum operators, respectively, and Z is the nuclear charge. Wavefunctions of the T_1 and S_1 states are approximately described by the Slater determinants, as follows:

$$\left| \Psi_{T_1,+1} \right\rangle = \left| X\bar{Y} \right\rangle \tag{A3}$$

$$\left| \Psi_{T_1,0} \right\rangle = \frac{1}{\sqrt{2}} \left\{ \left| X\bar{Y} \right\rangle + \left| \bar{X}Y \right\rangle \right\} \tag{A4}$$

$$\left| \Psi_{T_1,-1} \right\rangle = \left| \bar{X}\bar{Y} \right\rangle \tag{A5}$$

$$\left|\Psi_{S_1,0}\right\rangle = \frac{1}{\sqrt{2}}\left\{ \left|X\overline{Y}\right\rangle - \left|\overline{X}Y\right\rangle \right\} \tag{A6}$$

where X and Y are α-spin MOs of the T_1 and S_1 states and $\overline{X}$ and $\overline{Y}$ are their β-spin MOs. These Slater determinants are described by the Hartree products, as follows:

$$\left|\Psi_{T_1,+1}\right\rangle = \frac{1}{\sqrt{2}}\left\{ \left|XY\right| - \left|YX\right| \right\} \tag{A7}$$

$$\left|\Psi_{T_1,0}\right\rangle = \frac{1}{2}\left\{ \left|X\overline{Y}\right| - \left|\overline{Y}X\right| + \left|\overline{X}Y\right| - \left|Y\overline{X}\right| \right\} \tag{A8}$$

$$\left|\Psi_{T_1,-1}\right\rangle = \frac{1}{\sqrt{2}}\left\{ \left|\overline{X}\overline{Y}\right| - \left|\overline{Y}\overline{X}\right| \right\} \tag{A9}$$

$$\left|\Psi_{S_1,0}\right\rangle = \frac{1}{2}\left\{ \left|X\overline{Y}\right| - \left|\overline{Y}X\right| - \left|\overline{X}Y\right| + \left|Y\overline{X}\right| \right\} \tag{A10}$$

In two electron system, the one-electron term of the Breit–Pauli Hamiltonian is described, as below:

$$H_{SO} = \frac{\alpha^2}{2} \sum_{A}^{nuclear} \sum_{j}^{electron} \frac{Z_{eff,A}}{r_{Aj}^3} \; l_{Aj} \cdot s_j \tag{A11}$$

$$= \sum_{A}^{nuclear} \sum_{j=1}^{2} \lambda_{Aj} \; l_{Aj} \cdot s_j \tag{A12}$$

$$= \sum_{A}^{nuclear} \left\{ \lambda_{A1} \; l_{A1} \cdot s_1 + \lambda_{A2} \; l_{A2} \cdot s_2 \right\} \tag{A13}$$

$$= \sum_{A}^{nuclear} \left\{ \lambda_{A1} \left(l_{xA1} s_{x1} + l_{yA1} s_{y1} + l_{zA1} s_{z1} \right) + \lambda_{A2} \left(l_{xA2} s_{x2} + l_{yA2} s_{y2} + l_{zA2} s_{z2} \right) \right\} \tag{A14}$$

$$= \sum_{A}^{nuclear} \left\{ \lambda_{A1} \left(\frac{1}{2} (l_{A1}^{+} s_1^{-} + l_{A1}^{-} s_1^{+}) + l_{zA1} s_{z1} \right) \right.$$

$$+\lambda_{A2}\left(\frac{1}{2}(l_{A2}^{+}s_{2}^{-}+l_{A2}^{-}s_{2}^{+})+l_{zA2}s_{z2}\right)\Bigg\} \tag{A15}$$

where l_{Ax1}, l_{Ay1}, and l_{Az1} are *x*-, *y*-, and *z*-components of the orbital angular momentum operator for electron 1, respectively, around atom *A*. The s_{x1}, s_{y1}, and s_{z1} are *x*-, *y*-, and *z*-components of the spin angular momentum operator for electron 1, respectively. The $l^{+}{}_{A1}$ and $l^{-}{}_{A1}$ are the raising and lowering operators for the orbital angular momentum, respectively, and the $s^{+}{}_{1}$ and $s^{-}{}_{1}$ are the same operators for the spin angular momentum. The $\lambda_{A\,j}$ is equal to $(\alpha^2 Z_A)/(2r^3{}_{A\,j})$.

The wavefunction of the S_1 state (eq A10) is changed by operating of the spin–orbit Hamiltonian (eq S15):

$$H_{SO}\left|\Psi_{S_1,0}\right\rangle = \sum_{A}^{nuclear}\left\{\lambda_{A1}\left(\frac{1}{2}(l_{A1}^{+}s_{1}^{-}+l_{A1}^{-}s_{1}^{+})+l_{zA1}s_{z1}\right)\right.$$

$$\left.+\lambda_{A2}\left(\frac{1}{2}(l_{A2}^{+}s_{2}^{-}+l_{A2}^{-}s_{2}^{+})+l_{zA2}s_{z2}\right)\right\}\ \frac{1}{2}\left\{\ \left|X\overline{Y}\right|-\left|\overline{Y}X\right|-\left|\overline{X}Y\right|+\left|Y\overline{X}\right|\ \right\} \tag{A16}$$

$$=\frac{\hbar}{4}\sum_{A}^{nuclear}\left\{-\left(\lambda_{A1}l_{A1}^{-}-\lambda_{A2}l_{A2}^{-}\right)\left(\ \left|XY\right|+\left|YX\right|\ \right)\right.$$

$$+\left(\lambda_{A1}l_{zA1}-\lambda_{A2}l_{zA2}\right)\left(\ \left|X\overline{Y}\right|+\left|\overline{Y}X\right|+\left|\overline{X}Y\right|+\left|Y\overline{X}\right|\ \right)$$

$$\left.+\left(\lambda_{A1}l_{A1}^{+}-\lambda_{A2}l_{A2}^{+}\right)\left(\ \left|\overline{XY}\right|+\left|\overline{YX}\right|\right)\ \right\} \tag{A17}$$

where $\hbar$ is the reduced Planck constant.

Multiplying this equation by the T_1-wavefunctions (eqs A7–9) develops the spin–orbit matrix elements between the T_1 and S_1 states, as follows:

$$\left\langle\Psi_{T_1,+1}\left|H_{SO}\right|\Psi_{S_1,0}\right\rangle = \frac{1}{\sqrt{2}}\left\{\ \left|XY\right|-\left|YX\right|\ \right\}\frac{\hbar}{4}\sum_{A}^{nuclear}\left\{-\left(\lambda_{A1}l_{A1}^{-}-\lambda_{A2}l_{A2}^{-}\right)\left(\ \left|XY\right|+\left|YX\right|\ \right)\right.$$

$$+\left(\lambda_{A1}l_{zA1}-\lambda_{A2}l_{zA2}\right)\left(\ \left|X\overline{Y}\right|+\left|\overline{Y}X\right|+\left|\overline{X}Y\right|+\left|Y\overline{X}\right|\ \right)$$

$$\left.+\left(\lambda_{A1}l_{A1}^{+}-\lambda_{A2}l_{A2}^{+}\right)\left(\ \left|\overline{XY}\right|+\left|\overline{YX}\right|\ \right)\ \right\} \tag{A18}$$

$$=-\frac{\hbar}{4\sqrt{2}}\left\{\left\{\ \left|XY\right|-\left|YX\right|\ \right\}\sum_{A}^{nuclear}\left(\lambda_{A1}l_{A1}^{-}-\lambda_{A2}l_{A2}^{-}\right)\left(\ \left|XY\right|+\left|YX\right|\ \right)\right\} \tag{A19}$$

$$= -\frac{\hbar}{2\sqrt{2}}\left\{\langle X|\sum_{A}^{nuclear}\lambda_A l_A^-|X\rangle - \langle Y|\sum_{A}^{nuclear}\lambda_A l_A^-|Y\rangle\right\} \quad \text{(A20)}$$

$$\langle \Psi_{T_1,0}|H_{SO}|\Psi_{S_1,0}\rangle = \frac{1}{2}\left\{\,|X\overline{Y}| - |\overline{Y}X| + |\overline{X}Y| - |Y\overline{X}|\,\right\}$$

$$\times\ \frac{\hbar}{4}\sum_{A}^{nuclear}\left\{ -\left(\lambda_{A1}l_{A1}^- - \lambda_{A2}l_{A2}^-\right)\left(\,|XY| + |YX|\,\right)\right.$$

$$+\left(\lambda_{A1}l_{zA1} - \lambda_{A2}l_{zA2}\right)\left(\,|X\overline{Y}| + |\overline{Y}X| + |\overline{X}Y| + |Y\overline{X}|\,\right)$$

$$\left.+\left(\lambda_{A1}l_{A1}^+ - \lambda_{A2}l_{A2}^+\right)\left(\,|\overline{XY}| + |\overline{YX}|\,\right)\right\} \quad \text{(A21)}$$

$$= \frac{\hbar}{8}\left\{\,|X\overline{Y}| - |\overline{Y}X| + |\overline{X}Y| - |Y\overline{X}|\,\right\}$$

$$\times\ \sum_{A}^{nuclear}\left(\lambda_{A1}l_{zA1} - \lambda_{A2}l_{zA2}\right)\left(\,|X\overline{Y}| + |\overline{Y}X| + |\overline{X}Y| + |Y\overline{X}|\,\right) \quad \text{(A22)}$$

$$= \frac{\hbar}{2}\left\{\langle X|\sum_{A}^{nuclear}\lambda_A l_{zA}|X\rangle - \langle Y|\sum_{A}^{nuclear}\lambda_A l_{zA}|Y\rangle\right\} \quad \text{(A23)}$$

$$= \frac{\alpha^2\hbar}{4}\left\{\langle X|\sum_{A}^{nuclear}\frac{Z_{eff,A}}{r_A^3}l_{zA}|X\rangle - \langle Y|\sum_{A}^{nuclear}\lambda_A l_{zA}|Y\rangle\right\} \quad \text{(A24)}$$

$$\langle \Psi_{T_1,-1}|H_{SO}|\Psi_{S_1,0}\rangle = \frac{1}{\sqrt{2}}\left\{\,|\overline{XY}| - |\overline{YX}|\,\right\}\frac{\hbar}{4}\sum_{A}^{nuclear}\left\{ -\left(\lambda_{A1}l_{A1}^- - \lambda_{A2}l_{A2}^-\right)\left(\,|XY| + |YX|\,\right)\right.$$

$$+\left(\lambda_{A1}l_{zA1} - \lambda_{A2}l_{zA2}\right)\left(\,|X\overline{Y}| + |\overline{Y}X| + |\overline{X}Y| + |Y\overline{X}|\,\right)$$

$$\left.+\left(\lambda_{A1}l_{A1}^+ - \lambda_{A2}l_{A2}^+\right)\left(\,|\overline{XY}| + |\overline{YX}|\,\right)\right\} \quad \text{(A25)}$$

$$= \frac{\hbar}{4\sqrt{2}}\left\{\,|\overline{XY}| - |\overline{YX}|\,\right\}\sum_{A}^{nuclear}\left\{\left(\lambda_{A1}l_{A1}^+ - \lambda_{A2}l_{A2}^+\right)\left(\,|\overline{XY}| + |\overline{YX}|\,\right)\right. \quad \text{(A26)}$$

$$= \frac{\hbar}{2\sqrt{2}}\left\{\left\langle \overline{X}\right| \sum_{A}^{nuclear} \lambda_A l_A^+ \left|\overline{X}\right\rangle - \left\langle \overline{Y}\right| \sum_{A}^{nuclear} \lambda_A l_A^+ \left|\overline{Y}\right\rangle\right\} \quad \text{(A27)}$$

$$= \frac{\hbar}{2\sqrt{2}}\left\{\left\langle X\right| \sum_{A}^{nuclear} \lambda_A l_A^+ \left|X\right\rangle - \left\langle Y\right| \sum_{A}^{nuclear} \lambda_A l_A^+ \left|Y\right\rangle\right\} \quad \text{(A28)}$$

Eqs A25 and A28 are deformed with the relational expressions $l_A^+ = l_{xA} + i\, l_{yA}$ and $l_A^- = l_{xA} - i\, l_{yA}$, where i is the imaginary unit:

$$\left\langle \Psi_{T_1,+1}\right| H_{SO} \left|\Psi_{S_1,0}\right\rangle = -\frac{\hbar}{2\sqrt{2}}\left\{\left\langle X\right| \sum_{A}^{nuclear} \lambda_A l_{xA} \left|X\right\rangle - \left\langle Y\right| \sum_{A}^{nuclear} \lambda_A l_{xA} \left|Y\right\rangle\right\}$$

$$+ \; i\frac{\hbar}{2\sqrt{2}}\left\{\left\langle X\right| \sum_{A}^{nuclear} \lambda_A l_{yA} \left|X\right\rangle - \left\langle Y\right| \sum_{A}^{nuclear} \lambda_A l_{yA} \left|Y\right\rangle\right\} \quad \text{(A29)}$$

$$= -\frac{\alpha^2\hbar}{4\sqrt{2}}\left\{\left\langle X\right| \sum_{A}^{nuclear} \frac{Z_{eff,A}}{r_A^3} l_{xA} \left|X\right\rangle - \left\langle Y\right| \sum_{A}^{nuclear} \frac{Z_{eff,A}}{r_A^3} l_{xA} \left|Y\right\rangle\right\}$$

$$+ \; i\frac{\alpha^2\hbar}{4\sqrt{2}}\left\{\left\langle X\right| \sum_{A}^{nuclear} \frac{Z_{eff,A}}{r_A^3} l_{yA} \left|X\right\rangle - \left\langle Y\right| \sum_{A}^{nuclear} \frac{Z_{eff,A}}{r_A^3} l_{yA} \left|Y\right\rangle\right\} \quad \text{(A30)}$$

$$\left\langle \Psi_{T_1,-1}\right| H_{SO} \left|\Psi_{S_1,0}\right\rangle = \frac{\hbar}{2\sqrt{2}}\left\{\left\langle X\right| \sum_{A}^{nuclear} \lambda_A l_{xA} \left|X\right\rangle - \left\langle Y\right| \sum_{A}^{nuclear} \lambda_A l_{xA} \left|Y\right\rangle\right\}$$

$$+ \; i\frac{\hbar}{2\sqrt{2}}\left\{\left\langle X\right| \sum_{A}^{nuclear} \lambda_A l_{yA} \left|X\right\rangle - \left\langle Y\right| \sum_{A}^{nuclear} \lambda_A l_{yA} \left|Y\right\rangle\right\} \quad \text{(A31)}$$

$$= \frac{\alpha^2\hbar}{4\sqrt{2}}\left\{\left\langle X\right| \sum_{A}^{nuclear} \frac{Z_{eff,A}}{r_A^3} l_{xA} \left|X\right\rangle - \left\langle Y\right| \sum_{A}^{nuclear} \frac{Z_{eff,A}}{r_A^3} l_{xA} \left|Y\right\rangle\right\}$$

$$+ \; i\frac{\alpha^2\hbar}{4\sqrt{2}}\left\{\left\langle X\right| \sum_{A}^{nuclear} \frac{Z_{eff,A}}{r_A^3} l_{yA} \left|X\right\rangle - \left\langle Y\right| \sum_{A}^{nuclear} \frac{Z_{eff,A}}{r_A^3} l_{yA} \left|Y\right\rangle\right\} \quad \text{(A32)}$$

Eq A30 is combined with eq A32, as below:

$$\left\langle \Psi_{T_1,\pm1}\right| H_{SO} \left|\Psi_{S_1,0}\right\rangle = \mp\frac{\alpha^2\hbar}{4\sqrt{2}}\left\{\left\langle X\right| \sum_{A}^{nuclear} \frac{Z_{eff,A}}{r_A^3} l_{xA} \left|X\right\rangle - \left\langle Y\right| \sum_{A}^{nuclear} \frac{Z_{eff,A}}{r_A^3} l_{xA} \left|Y\right\rangle\right\}$$

$$+ \; i\frac{\alpha^2\hbar}{4\sqrt{2}}\left\{\left\langle X\left|\sum_A^{nuclear}\frac{Z_{eff,A}}{r_A^3}l_{yA}\right|X\right\rangle-\left\langle Y\left|\sum_A^{nuclear}\frac{Z_{eff,A}}{r_A^3}l_{yA}\right|Y\right\rangle\right\} \quad \text{(A33)}$$

It is likely that the intersystem crossing occurs at the S_1-equilibrium geometry because the geometry of the S_1 state easily changes to this geometry. Thus, we investigated the spin–orbit interaction between the T_1 and S_1 states at the S_1-equilibrium geometry from eqs A24 and A33.

In CH_3CN, the global minimum geometry **$1S_{1a}$'** is C_{2v} symmetrical. The SOMOs of **$1S_{1a}$'** are the dσ*(Pt–Pt) and π*(bpym) orbitals, as shown in Figure 1, where the former and the latter SOMOs correspond to *X* and *Y*, respectively, in above equations. The irreducible representation of the the dσ*(Pt–Pt) orbital is b_1 and that of the π*(bpym) orbital is a_1. The irreducible representation of the *x*-component of the angular momentum operator ($\Sigma(Z_{eff,A}/r_A^3)l_{xA}$) is b_2 because its representation is the same as the R_x operator, where the R_x means the rotation around the *x*-axis. Similarly, the irreducible representations of the $\Sigma(Z_{eff,A}/r_A^3)l_{yA}$ and $\Sigma(Z_{eff,A}/r_A^3)l_{zA}$ operators are b_1 and a_2, respectively. Thus, the direct product of these irreducible representations is b_1 (= $a_1 \times b_1 \times a_1$) for the $<\pi^*(\text{bpym})|\Sigma(Z_{eff,A}/r_A^3)l_{xA}|\text{d}\sigma^*(\text{Pt–Pt})>$. Because this is not a_1, the matrix element $<\pi^*(\text{bpym})|\Sigma(Z_{eff,A}/r_A^3)l_{xA}|\text{d}\sigma^*(\text{Pt–Pt})>$ becomes zero. The other matrix elements in eqs A24 and A33 are also zero because of the same reason (see Table A5), leading to the absence of the spin–orbit interaction between the T_1 and S_1 states. As a result, the $S_1 \rightarrow T_1$ intersystem crossing hardly occurs in the **$1S_{1a}$'** geometry.

The local minimum geometry **$1S_{1b}$** is C_1 symmetrical, in which the SOMOs are the π(bpym) and π*(bpym) orbitals, as shown in Figure 1, where the former and the latter SOMOs correspond to *X* and *Y*, respectively, in above equations. The irreducible representations of these orbitals are "a". Also, the irreducible representations of the $\Sigma(Z_{eff,A}/r_A^3)l_{xA}$, $\Sigma(Z_{eff,A}/r_A^3)l_{yA}$, and $\Sigma(Z_{eff,A}/r_A^3)l_{zA}$ operators are "a". Because the direct product of these irreducible representations is "a", as shown in Table A3, all matrix elements in eqs A24 and A33 are non-zero, leading to the presence of the spin–orbit interaction. Thus, the $S_1 \rightarrow T_1$ intersystem crossing occurs in the **$1S_{1b}$** geometry.

Table A5. Direct products of matrix elements in eqs A24 and A33 at the S_1-minimum geometries

	1S$_{1a}$' (C_{2v})	**1S$_{1b}$** (C_1)	**2S$_{1a}$** (C_2)
$\left\langle X \middle\| \sum_A^{nuclear} \frac{Z_{eff,A}}{r_A^3} l_{xA} \middle\| X \right\rangle$	$b_1 \times b_2 \times b_1 = b_2$	$a \times a \times a = a$	$b \times b \times b = b$
$\left\langle Y \middle\| \sum_A^{nuclear} \frac{Z_{eff,A}}{r_A^3} l_{xA} \middle\| Y \right\rangle$	$a_1 \times b_2 \times a_1 = b_2$	$a \times a \times a = a$	$a \times b \times a = b$
$\left\langle X \middle\| \sum_A^{nuclear} \frac{Z_{eff,A}}{r_A^3} l_{yA} \middle\| X \right\rangle$	$b_1 \times b_1 \times b_1 = b_1$	$a \times a \times a = a$	$b \times b \times b = b$
$\left\langle Y \middle\| \sum_A^{nuclear} \frac{Z_{eff,A}}{r_A^3} l_{yA} \middle\| Y \right\rangle$	$a_1 \times b_1 \times a_1 = b_1$	$a \times a \times a = a$	$a \times b \times a = b$
$\left\langle X \middle\| \sum_A^{nuclear} \frac{Z_{eff,A}}{r_A^3} l_{zA} \middle\| X \right\rangle$	$b_1 \times a_2 \times b_1 = a_2$	$a \times a \times a = a$	$b \times a \times b = a$
$\left\langle Y \middle\| \sum_A^{nuclear} \frac{Z_{eff,A}}{r_A^3} l_{zA} \middle\| Y \right\rangle$	$a_1 \times a_2 \times a_1 = a_2$	$a \times a \times a = a$	$a \times a \times a = a$

In **2**, the global minimum geometry **2S$_{1a}$** is C_2 symmetrical, in which the SOMOs are the dσ*(Pt–Pt) and π*(ppy) orbitals, as shown in Figure 1, where the former SOMO corresponds to *X* and the latter one corresponds to *Y* in above equations. Irreducible representations of these SOMOs are "b" and "a", respectively. The $\Sigma(Z_{eff,A}/r_A^3)l_{xA}$ and $\Sigma(Z_{eff,A}/r_A^3)l_{yA}$ operators belong to "b" irreducible representation and the $\Sigma(Z_{eff,A}/r_A^3)l_{zA}$ operator belongs to "a" irreducible representation. All direct products of these irreducible representations are not "a"; for example, the direct product of the irreducible representations is b (= a × b × a) in $<\pi^*(\text{ppy})|\Sigma(Z_{eff,A}/r_A^3)l_{xA}|\pi^*(\text{ppy})>$; see Table A3. Thus, all matrix elements in eq A33 becomes zero, and hence, the spin–orbit matrix element $<\Psi_{T1,\pm1}|H_{SO}|\Psi_{S1,0}>$ becomes zero. On the other hand, the $<X|\Sigma(Z_{eff,A}/r_A^3)l_{zA}|X>$ and $<Y|\Sigma(Z_{eff,A}/r_A^3)l_{zA}|Y>$ matrix elements in eq A24 are not zero, because the direct products of the irreducible representations are "a" in these matrix elements; for example, the direct product is a (= a × a × a) for the $<\pi^*(\text{ppy})|\Sigma(Z_{eff,A}/r_A^3)l_{zA}|\pi^*(\text{ppy})>$. Thus, the spin–orbit matrix

element $\langle \Psi_{T1,0} | H_{SO} | \Psi_{S1,0} \rangle$ is not zero. From these results, it is concluded that the $S_1 \rightarrow T_1$ intersystem crossing occurs at the **$2S_{1a}$** geometry.

Next, we will discuss the spin-orbit interaction between the T_1 and S_2 states of **1**. Wavefunction of the S_2 states is represented by the Slater determinants, as follows:

$$\left|\Psi_{S_2,0}\right\rangle = \frac{1}{\sqrt{2}}\left\{ \left|X\bar{Z}\right\rangle - \left|\bar{X}Z\right\rangle \right\} \qquad \text{(A34)}$$

where, X and Z are SOMOs of the S_2 state; the former is the same as the one SOMO of the T_1 state while the latter is different from that of the T_1 state, as shown in Scheme A3. The Slater determinants in eq A34 are described by the Hartree products, as follows:

$$\left|\Psi_{S_2,0}\right\rangle = \frac{1}{2}\left\{ \left|X\bar{Z}\right| - \left|\bar{Z}X\right| - \left|\bar{X}Z\right| + \left|Z\bar{X}\right| \right\} \qquad \text{(A35)}$$

Scheme A3.

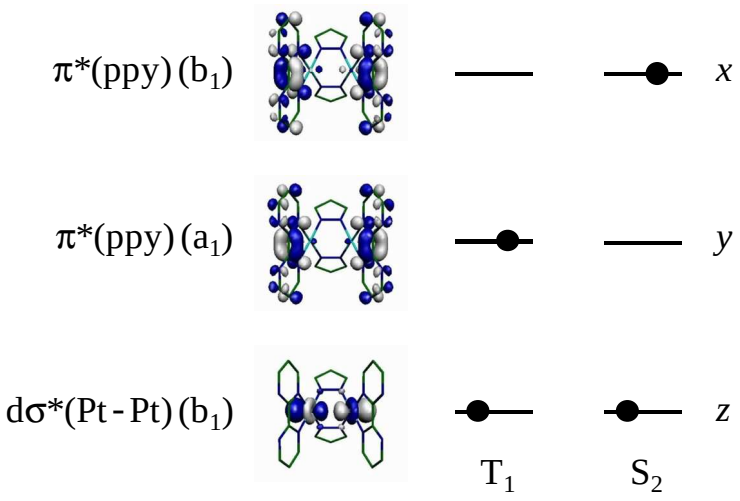

The wavefunction of the S_2 state is changed by operating of the spin–orbit Hamiltonian (eq A15):

$$H_{SO}\left|\Psi_{S_2,0}\right\rangle = \sum_A^{nuclear}\left\{\lambda_{A1}\left(\frac{1}{2}(l_{A1}^{+}s_1^{-}+l_{A1}^{-}s_1^{+})+l_{zA1}s_{z1}\right)\right.$$

$$\left.+\lambda_{A2}\left(\frac{1}{2}(l_{A2}^{+}s_2^{-}+l_{A2}^{-}s_2^{+})+l_{zA2}s_{z2}\right)\right\}\ \frac{1}{2}\left\{\ \left|X\overline{Z}\right|-\left|\overline{Z}X\right|-\left|\overline{X}Z\right|+\left|Z\overline{X}\right|\ \right\} \quad \text{(A36)}$$

$$= \frac{\hbar}{4}\sum_A^{nuclear}\left\{-\left(\lambda_{A1}l_{A1}^{-}-\lambda_{A2}l_{A2}^{-}\right)\left(\ \left|XZ\right|+\left|ZX\right|\ \right)\right.$$

$$+\left(\lambda_{A1}l_{zA1}-\lambda_{A2}l_{zA2}\right)\left(\ \left|X\overline{Z}\right|+\left|\overline{Z}X\right|+\left|\overline{X}Z\right|+\left|Z\overline{X}\right|\ \right)$$

$$\left.+\left(\lambda_{A1}l_{A1}^{+}-\lambda_{A2}l_{A2}^{+}\right)\left(\ \left|\overline{XZ}\right|+\left|\overline{ZX}\right|\right)\ \right\} \quad \text{(A37)}$$

Multiplying this equation by the T_1-wavefunctions (eqs A7–9) develops the spin–orbit matrix elements between the T_1 and S_2 states, as follows:

$$\left\langle\Psi_{T_1,+1}\left|H_{SO}\right|\Psi_{S_2,0}\right\rangle = \frac{1}{\sqrt{2}}\left\{\ \left|XY\right|-\left|YX\right|\ \right\}\frac{\hbar}{4}\sum_A^{nuclear}\left\{-\left(\lambda_{A1}l_{A1}^{-}-\lambda_{A2}l_{A2}^{-}\right)\left(\ \left|XZ\right|+\left|ZX\right|\ \right)\right.$$

$$+\left(\lambda_{A1}l_{zA1}-\lambda_{A2}l_{zA2}\right)\left(\ \left|X\overline{Z}\right|+\left|\overline{Z}X\right|+\left|\overline{X}Z\right|+\left|Z\overline{X}\right|\ \right)$$

$$\left.+\left(\lambda_{A1}l_{A1}^{+}-\lambda_{A2}l_{A2}^{+}\right)\left(\ \left|\overline{XZ}\right|+\left|\overline{ZX}\right|\ \right)\ \right\} \quad \text{(A38)}$$

$$= -\frac{\hbar}{4\sqrt{2}}\left\{\left\{\ \left|XY\right|-\left|YX\right|\ \right\}\sum_A^{nuclear}\left(\lambda_{A1}l_{A1}^{-}-\lambda_{A2}l_{A2}^{-}\right)\left(\ \left|XZ\right|+\left|ZX\right|\ \right)\right\}$$

(A39)

$$= \frac{\hbar}{2\sqrt{2}}\left\langle Y\right|\sum_A^{nuclear}\lambda_A l_A^{-}\left|Z\right\rangle \quad \text{(A40)}$$

$$\left\langle\Psi_{T_1,0}\left|H_{SO}\right|\Psi_{S_2,0}\right\rangle = \frac{1}{2}\left\{\ \left|X\overline{Y}\right|-\left|\overline{Y}X\right|+\left|\overline{X}Y\right|-\left|Y\overline{X}\right|\ \right\}$$

$$\times\ \frac{\hbar}{4}\sum_A^{nuclear}\left\{-\left(\lambda_{A1}l_{A1}^{-}-\lambda_{A2}l_{A2}^{-}\right)\left(\ \left|XZ\right|+\left|ZX\right|\ \right)\right.$$

$$\left.+\left(\lambda_{A1}l_{zA1}-\lambda_{A2}l_{zA2}\right)\left(\ \left|X\overline{Z}\right|+\left|\overline{Z}X\right|+\left|\overline{X}Z\right|+\left|Z\overline{X}\right|\ \right)\right.$$

$$+\left(\lambda_{A1} l_{A1}^{+} - \lambda_{A2} l_{A2}^{+}\right)\left(\left|\overline{XZ}\right| + \left|\overline{ZX}\right| \right) \Big\} \tag{A41}$$

$$= \frac{\hbar}{8}\Big\{ \left|X\overline{Y}\right| - \left|\overline{Y}X\right| + \left|\overline{X}Y\right| - \left|Y\overline{X}\right| \Big\}$$

$$\times \sum_{A}^{nuclear} \left(\lambda_{A1} l_{zA1} - \lambda_{A2} l_{zA2}\right)\left(\left|X\overline{Z}\right| + \left|\overline{Z}X\right| + \left|\overline{X}Z\right| + \left|Z\overline{X}\right| \right) \tag{A42}$$

$$= -\frac{\hbar}{2}\left\langle Y \right| \sum_{A}^{nuclear} \lambda_A l_{zA} \left| Z \right\rangle \tag{A43}$$

$$= -\frac{\alpha^2 \hbar}{4}\left\langle Y \right| \sum_{A}^{nuclear} \frac{Z_{eff,A}}{r_A^3} l_{zA} \left| Z \right\rangle \tag{A44}$$

$$\left\langle \Psi_{T_1,-1} \left| H_{SO} \right| \Psi_{S_2,0} \right\rangle = \frac{1}{\sqrt{2}}\Big\{ \left|\overline{XY}\right| - \left|\overline{YX}\right| \Big\} \frac{\hbar}{4} \sum_{A}^{nuclear} \Big\{ -\left(\lambda_{A1} l_{A1}^{-} - \lambda_{A2} l_{A2}^{-}\right)\left(\left|XZ\right| + \left|ZX\right| \right)$$

$$+\left(\lambda_{A1} l_{zA1} - \lambda_{A2} l_{zA2}\right)\left(\left|X\overline{Z}\right| + \left|\overline{Z}X\right| + \left|\overline{X}Z\right| + \left|Z\overline{X}\right| \right)$$

$$+\left(\lambda_{A1} l_{A1}^{+} - \lambda_{A2} l_{A2}^{+}\right)\left(\left|\overline{XZ}\right| + \left|\overline{ZX}\right| \right) \Big\} \tag{A45}$$

$$= \frac{\hbar}{4\sqrt{2}}\Big\{ \left|\overline{XY}\right| - \left|\overline{YX}\right| \Big\} \sum_{A}^{nuclear} \Big\{ \left(\lambda_{A1} l_{A1}^{+} - \lambda_{A2} l_{A2}^{+}\right)\left(\left|\overline{XZ}\right| + \left|\overline{ZX}\right| \right) \tag{A46}$$

$$= \frac{\hbar}{2\sqrt{2}}\left\langle \overline{Y} \right| \sum_{A}^{nuclear} \lambda_A l_A^{+} \left| \overline{Z} \right\rangle \tag{A47}$$

$$= \frac{\hbar}{2\sqrt{2}}\left\langle Y \right| \sum_{A}^{nuclear} \lambda_A l_A^{+} \left| Z \right\rangle \tag{A48}$$

Eqs A40 and A48 are deformed with the relational expressions $l_A^{+} = l_{xA} + i\, l_{yA}$ and $l_A^{-} = l_{xA} - i\, l_{yA}$, as follows:

$$\left\langle \Psi_{T_1,+1} \left| H_{SO} \right| \Psi_{S_2,0} \right\rangle = \frac{\hbar}{2\sqrt{2}}\left\langle Y \right| \sum_{A}^{nuclear} \lambda_A l_{xA} \left| Z \right\rangle \; - \; i\frac{\hbar}{2\sqrt{2}}\left\langle Y \right| \sum_{A}^{nuclear} \lambda_A l_{yA} \left| Z \right\rangle \tag{A49}$$

$$= \frac{\alpha^2\hbar}{4\sqrt{2}}\langle Y|\sum_A^{nuclear}\frac{Z_{eff,A}}{r_A^3}l_{xA}|Z\rangle - i\frac{\alpha^2\hbar}{4\sqrt{2}}\langle Y|\sum_A^{nuclear}\frac{Z_{eff,A}}{r_A^3}l_{yA}|Z\rangle \quad \text{(A50)}$$

$$\langle \Psi_{T_1,-1}|H_{SO}|\Psi_{S_2,0}\rangle = \frac{\hbar}{2\sqrt{2}}\langle Y|\sum_A^{nuclear}\lambda_A l_{xA}|Z\rangle + i\frac{\hbar}{2\sqrt{2}}\langle Y|\sum_A^{nuclear}\lambda_A l_{yA}|Z\rangle \quad \text{(A51)}$$

$$= \frac{\alpha^2\hbar}{4\sqrt{2}}\langle Y|\sum_A^{nuclear}\frac{Z_{eff,A}}{r_A^3}l_{xA}|Z\rangle + i\frac{\alpha^2\hbar}{4\sqrt{2}}\langle Y|\sum_A^{nuclear}\frac{Z_{eff,A}}{r_A^3}l_{yA}|Z\rangle \quad \text{(A52)}$$

Eq A50 is combined with eq A52, as below:

$$\langle \Psi_{T_1,\pm1}|H_{SO}|\Psi_{S_2,0}\rangle = \frac{\alpha^2\hbar}{4\sqrt{2}}\langle Y|\sum_A^{nuclear}\frac{Z_{eff,A}}{r_A^3}l_{xA}|Z\rangle \mp i\frac{\alpha^2\hbar}{4\sqrt{2}}\langle Y|\sum_A^{nuclear}\frac{Z_{eff,A}}{r_A^3}l_{yA}|Z\rangle \quad \text{(A53)}$$

Here, we will discuss the spin-orbit interaction between the T_1 and S_2 excited states at the **1T$_{1a}$'** geometry to investigate whether the S_2 state mixes to the T_1 state or not. In the **1T$_{1a}$'** geometry, the SOMOs of the T_1 state are the dσ*(Pt–Pt) (b_1) and π*(ppy) (a_1) orbitals and those of the S_2 state are the dσ*(Pt–Pt) (b_1) and antisymmetrical π*(ppy) (b_1) orbitals, as shown in Scheme A3, where the dσ*(Pt–Pt) (b_1), π*(ppy) (a_1), and π*(ppy) (b_1) orbitals correspond to *X*, *Y*, and *Z*, respectively; see Scheme A3 for *X*, *Y*, and *Z*. The irreducible representations of the $\Sigma(Z_{eff,A}/{r_A}^3)l_{xA}$, $\Sigma(Z_{eff,A}/{r_A}^3)l_{yA}$, and $\Sigma(Z_{eff,A}/{r_A}^3)l_{zA}$ operators are b_2, b_1 and a_2, respectively, as discussed above.

Table A6. Direct products of matrix elements in eqs A44 and A53 at the **1T$_{1a}$'** geometry

	1T$_{1a}$' (C_{2v})
$\langle Y\|\sum_A^{nuclear}\frac{Z_{eff,A}}{r_A^3}l_{xA}\|Z\rangle$	$a_1 \times b_2 \times b_1 = a_2$
$\langle Y\|\sum_A^{nuclear}\frac{Z_{eff,A}}{r_A^3}l_{yA}\|Z\rangle$	$a_1 \times b_1 \times b_1 = a_1$
$\langle Y\|\sum_A^{nuclear}\frac{Z_{eff,A}}{r_A^3}l_{zA}\|Z\rangle$	$a_1 \times a_2 \times b_1 = b_2$

References and Notes

(1) Selected reviews for emissive complexes applied to optical materials: (a) Amendola, V.; Fabbrizzi, L.; Foti, F.; Licchelli, M.; Mangano, C.; Pallavicini, P.; Poggi, A.; Sacchi, D.; Taglietti, A. *Coord. Chem. Rev.* **2006**, *250*, 273. (b) Rogers, C. W.; Wolf, M. O. *Coord. Chem. Rev.* **2002**, *233–234*, 341. (c) Keefe, M. H.; Benkstein, K. D.; Hupp, J. T. *Coord. Chem. Rev.* **2000**, *205*, 201.

(2) Selected reviews for emissive iridium complexes applied to optical materials: (a) Evans, R. C.; Douglas, P.; Winscom, C. J. *Coord. Chem. Rev.* **2006**, *250*, 2093. (b) Marin, V.; Holder, E.; Hoogenboom, R.; Schubert, U. S. *Chem. Soc. Rev.* **2007**, *36*, 618. (c) Lo, K. K.-W.; Hui, W.-K.; Chung, C.-K.; Tsang, K. H.-K.; Lee, T. K.-M.; Li, C.-K.; Lau, J. S.-Y.; Ng, D. C.-M. *Coord. Chem. Rev.* **2006**, *250*, 1724. (d) Lo, K. K.-W.; Hui,W.-K.; Chung, C.-K.; Tsang, K. H.-K.; Ng, D. C.-M.; Zhu, N.; Cheung, K.-K. *Coord. Chem. Rev.* **2005**, *249*, 1434.

(3) Selected reviews for emissive platinum complexes applied to optical materials: (a) Kato, M. *Bull. Chem. Soc. Jpn.* **2007**, *80*, 287. (b) Yam, V. W.-W. *Acc. Chem. Res.* **2002**, *35*, 555. (c) Hissler, M.; McGarrah, J. E.; Connick,W. B.; Geiger, D. K.; Cummings, S. D.; Eisenberg, R. *Coord. Chem. Rev.* **2000**, *208*, 115. (d) Paw, W.; Cummings, S. D.; Mansour, M. A.; Connick, W. B.; Geiger, D. K.; Eisenberg, R. *Coord. Chem. Rev.* **1998**, *171*, 125.

(4) Selected review for the fundamental study of emissive platinum complexes: Wong, K. M.-C.; Hui, C.-K.; Yu, K.-L.; Yam, V. W.-W. *Coord. Chem. Rev.* **2002**, *229*, 123.

(5) Umakoshi, K.; Kimura, K.; Kim, Y. H.; Tsukimoto, Y.; Arikawa, Y.; Onishi, M.; Ishizaka, S.; Kitamura, N. *Bull. Chem. Soc. Jpn.* **2010**, *83*, 1504.

(6) Koshiyama, T.; Omura, A.; Kato, M. *Chem. Lett.* **2004**, *33*, 1386.

(7) Ma, B.; Li, J.; Djurovich, P. I.; Yousufuddin, M.; Bau, R.; Thompson, M. E. *J. Am. Chem. Soc.* **2005**, *127*, 28.

(8) Saito, K.; Nakao, Y.; Sakaki, S. *Inorg. Chem.* **2008**, *47*, 4329.

(9) Hay, P. J.; Wadt, W. R. *J. Chem. Phys.* **1985**, *82*, 299.

(10) Couty, M.; Hall, M. B. *J. Comput. Chem.* **1996**, *17*, 1359.

(11) Ehlers, A. W.; Böhme, M.; Dapprich, S.; Gobbi, A.; Höllwarth, A.; Jonas, V.; Köhler, K. F.; Stegmann, R.; Veldkamp, A.; Frenking., G. *Chem. Phys. Lett.* **1993**, *208*, 111.

(12) (a) Hehre, W. J.; Ditchfield, R.; Pople, J. A. *J. Chem. Phys.* **1972**, *56*, 2257. (b) Hariharan, P. C.; Pople, J. A. *Theor. Chim. Acta* **1973**, *28*, 213. (c) Francl, M. M.; Pietro,W. J.; Hehre,W. J.; Binkley, J. S.; Gordon, M. S.; DeFrees, D. J.; Pople, J. A. *J. Chem. Phys.* **1982**, *77*, 3654.

(13) (a) Dunning, T. H., Jr. *J. Chem. Phys.* **1989**, *90*, 1007. (b)Woon, D. E.; Dunning, T. H., Jr. *J. Chem. Phys.* **1993**, *98*, 1358.

(14) (a) Becke, A. D. Phys. Rev. A 1988, 38, 3098. (b) Becke, A. D. *J. Chem. Phys.* **1993**, *98*, 5648.

(15) Perdew, J. P.; Wang, Y. *Phys. Rev. B* **1992**, *45*, 13244.

(16) The S^2 values were evaluated to be 1.01, 1.01, and 1.02 for the S_1-optimized geometries **$1S_{1a}$**, **$1S_{1b}$**, and **$2S_{1a}$**, respectively, where the *S* means the spin momentum operator. These evaluated values indicate that the spin symmetries of these evaluated S_1 wave functions are broken. On the contrary, the spin symmetry was not broken at all in the S_0 wave function and little broken in the T_1 wave function. The S^2 values were evaluated to be 0.00, 0.00, 2.01, 2.03, and 2.01 for the **$1S_0$**, **$2S_0$**, **$1T_{1a}$**, **$1T_{1b}$**, and **$2T_{1a}$** geometries, respectively.

(17) Gräfenstein, J.; Kraka, E.; Filatov, M.; Cremer, D. *Int. J. Mol. Sci.* **2002**, *3*, 360.

(18) Orbital energies and energies of phosphorescences are little different between basis-I and II, as shown in Tables A3 and A4 in the Appendix. This suggests that both basis sets are reliable.

(19) (a) Mennucci, B.; Tomasi, J. *J. Chem. Phys.* **1997**, *106*, 5151. (b) Cancès, M. T.; Mennucci, B.; Tomasi, J. *J. Chem. Phys.* **1997**, *107*, 3032. (c) Cossi, M.; Barone, V.; Mennucci, B.; Tomasi, J. *Chem. Phys. Lett.* **1998**, *286*, 253. (d) Tomasi, J.; Persico, M. *Chem. Rev.* **1994**, *94*, 2027.

(20) Rappè, A. K.; Casewit, C. J.; Colwell, K. S.; Goddard, W. A., III; Skiff, W. M. *J. Am. Chem. Soc.* **1992**, *114*, 10024.

(21) Frisch, M. J.; Trucks, G. W.; Schlegel, H. B.; Scuseria, G. E.; Robb, M. A.; Cheeseman, J. R.; Montgomery, Jr., J. A.; Vreven, T.; Kudin, K. N.; Burant, J. C.; Millam, J. M.; Iyengar, S. S.; Tomasi, J.; Barone, V.; Mennucci, B.; Cossi, M.; Scalmani, G.; Rega, N.; Petersson, G. A.; Nakatsuji, H.; Hada, M.; Ehara, M.; Toyota, K.; Fukuda, R.; Hasegawa, J.; Ishida, M.; Nakajima, T.; Honda, Y.; Kitao, O.; Nakai, H.; Klene, M.; Li, X.; Knox, J. E.; Hratchian, H. P.; Cross, J. B.; Bakken, V.; Adamo, C.; Jaramillo, J.; Gomperts, R.; Stratmann, R. E.; Yazyev, O.; Austin, A. J.; Cammi, R.; Pomelli, C.; Ochterski, J. W.; Ayala, P. Y.; Morokuma, K.; Voth, G. A.; Salvador, P.; Dannenberg, J. J.; Zakrzewski, V. G.; Dapprich, S.; Daniels, A. D.; Strain, M. C.; Farkas, O.; Malick, D. K.; Rabuck, A. D.; Raghavachari, K.; Foresman, J. B.; Ortiz, J. V.; Cui, Q.; Baboul, A. G.; Clifford, S.; Cioslowski, J.; Stefanov, B. B.; Liu, G.; Liashenko, A.; Piskorz, P.; Komaromi, I.; Martin, R. L.; Fox, D. J.; Keith, T.; Al-Laham, M. A.; Peng, C. Y.; Nanayakkara, A.; Challacombe, M.; Gill, P. M. W.; Johnson, B.; Chen, W.; Wong, M. W.; Gonzalez, C.; and Pople, J. A.; *Gaussian 03*, Revision C.02, Gaussian, Inc., Wallingford CT, 2004.

(22) (a) Flükiger, P.; Lüthi, H. P.; Portmann, S.; Weber, J. *MOLEKEL*, version 4.3; Scientific Computing: Manno, Switzerland, 2000–2002. (b) Portmann, S.; Lüthi, H. P. *Chimia* **2000**, *54*, 766.

(23) Szabo, A.; Ostlund, N. S. *Modern Quantum Chemistry: Introduction to Advanced Electronic Structure Theory*; Dover Publications, Inc.: New York, 1996.

(24) Although the MMLCT excitation decreases more the electron density of the dσ*(Pt–Pt) orbital in the CH_3CN solution than in vacuo in both **1** and **2**, the Pt–Pt distance of the MMLCT excited state is little different in **2** between the CH_3CN solution and in vacuo, unlike **1**. This is probably because the Pt–Pt distance of the MMLCT excited state is sufficiently short in **2** even in vacuo.

(25) (a) The direct product of two SOMOs of the S_2 state, two SOMOs of the T_1 state, and the *l* operator is

the a_1 representation; see the Appendix for details. (b) The oscillator strength of the $S_1 \rightarrow S_0$ transition at the **1T$_{1b}$** geometry is 0.0313 and that of the $S_2 \rightarrow S_0$ transition is 0.0022, indicating that the $S_2 \rightarrow S_0$ transition little contributes to the oscillator strength of the $T_1 \rightarrow S_0$ transition of **1**. Although the oscillator strength is moderately larger in the $S_1 \rightarrow S_0$ transition at the **1T$_{1b}$** geometry than in the $S_2 \rightarrow S_0$ transition at the **1T$_{1a}$** geometry, it should be concluded that the oscillator strength of the $T_1 \rightarrow S_0$ transition is not zero at the **1T$_{1a}$** geometry.

(26) Danilov, E. O.; Pomestchenko, I. E.; Kinayyigit, S.; Gentili, P. L.; Hissler, M.; Ziessel, R.; Castellano, F. N. *J. Phys. Chem. A* **2005**, *109*, 2465.

(27) (a) In the phosphorescence spectrum of **1** observed in the solid state at RT, three split peaks were observed at 2.41, 2.59, and 2.74 eV.[5] These split peaks were understood in terms of the coupling with the breathing vibration of the aromatic ring of bpym like the other pz-bridged dinuclear platinum(II) complex **3**.[7,8] Because such vibrational coupling is not incorporated by the usual electronic structure calculation, we compare here the calculated energy of phosphorescence with the average value of these three peaks. (b) Nonradiative decay hardly occurs in the **1T$_{1b}$** geometry, unlike in the **1T$_{1a}$'** geometry, because the energy difference between the T_1 and S_0 states is considerably larger in **1T$_{1b}$** than in **1T$_{1a}$'** ; see Table 4.

(28) It is noted that the energy difference between the T_1 and S_0 states in the CH_3CN solution is considerably larger at the **2T$_{1a}$** geometry (1.87 eV) than at the **1T$_{1a}$'** geometry (1.24 eV). Thus, the $T_1 \rightarrow S_0$ non-radiative decay hardly occurs in **2**, unlike in **1**, which agrees with the experimental results that phosphorescence of **2** is observed in the CH_3CN solution.

Chapter 5

Oscillator Strength of Symmetry-Forbidden d–d Absorption of Octahedral Transition Metal Complex: Theoretical Evaluation

5.1. Introduction

Absorption spectra of transition metal complexes can be easily investigated nowadays with electronic structure theory such as time-dependent density functional theory (TD-DFT)[1] and symmetry-adapted cluster expansion followed by configuration interaction (SAC/SAC−CI) method.[2] However, the oscillator strength of a symmetry-forbidden transition such as a d–d transition of a transition metal complex bearing inversion symmetry cannot be evaluated with the usual electronic structure theory, as is well-known.[3,4] In a real molecule, however, geometry is not frozen but thermally vibrating. Some of the molecular vibrations break the symmetry of geometry in which the transition dipole moment of the d–d transition becomes nonzero even in a metal complex with the inversion symmetry. In other words, the d–d absorption is induced by molecular vibration. This means that the oscillator strength of the symmetry-forbidden d–d transition can be theoretically evaluated by incorporating effects of molecular vibration into the electronic structure calculation. However, such theoretical evaluations have been limited, so far. One of the pioneering theoretical works was reported by Kato, Iuchi, and their collaborators.[5] They investigated the d–d absorption spectrum of octahedral $[Ni(H_2O)_6]^{2+}$ with a model Hamiltonian which was constructed by molecular dynamics simulation. Another example[6] was a theoretical study of the d–d absorption spectrum of square planar $[PtCl_4]^{2-}$ with the Hertzberg–Teller (HT) approximation.[7] In this study, the Taylor expansion of transition dipole M by normal coordinate Q_i is truncated at the second term and then the M value is calculated with the derivative of M by Q_i, $(\partial M/\partial Q_i)$, and the vibrational wave functions in the electronic ground

and excited states; see ref 8 for more details. Considering that the oscillator strength of symmetry-forbidden d–d transition has not been evaluated except for these studies, its theoretical evaluation is challenging even nowadays. Remember that the d–d absorption spectrum provides us with important knowledge of the d–d orbital energy gap. To present a correct assignment of the d–d absorption, the oscillator strength is indispensable. Thus, it is important to investigate theoretically the d–d absorption and its oscillator strength.

In this study, we wish to propose a new method to evaluate the oscillator strength of the symmetry-forbidden d–d transition. In our method, the geometry distribution around the equilibrium geometry is incorporated by considering the vibrational wave function, while the HT approximation was not employed. The Boltzmann distribution law was employed to evaluate the population of vibrationally excited state. This method was applied to octahedral transition metal complexes, $[Co(NH_3)_6]^{3+}$ and $[Rh(NH_3)_6]^{3+}$, as an example. Though these compounds are not of that much interest, we calculated the oscillator strength of these well-known compounds here because this is the first application of our method. Our purposes here are to examine whether or not our method is useful in evaluating the oscillator strengths of symmetry-forbidden d–d transitions, $^1A_{1g} \rightarrow {}^1T_{1g}$ and $^1A_{1g} \rightarrow {}^1T_{2g}$, of an octahedral transition metal complex,[9] to elucidate what kinds of molecular vibrations contribute to their oscillator strengths, to evaluate contribution of zero-point vibration, and to show how much temperature influences the oscillator strength.

5.2. Method and Computational Details

5.2.1. DFT Calculations

The core electrons of Co (up to 2p) and Rh (up to 3d) were replaced with the Stuttgart–Dresden–Bonn relativistic effective core potentials (SDB ECPs),[10,11] and their valence electrons were represented with (311111/22111/4111/11) basis sets.[10–12] The cc-pVDZ basis sets[13] were used for H and N.

Geometries of $[Co(NH_3)_6]^{3+}$ and $[Rh(NH_3)_6]^{3+}$ in the $^1A_{1g}$ ground state were optimized with the DFT method, where the B3PW91 functional[14,15] was employed. Their vibration frequencies were evaluated with the same method. Excitation energies of the $^1A_{1g} \rightarrow {}^1T_{1g}$ and $^1A_{1g} \rightarrow {}^1T_{2g}$ absorptions were evaluated with the TDDFT(B3PW91) method.[16,17]

All electronic structure calculations were performed by the Gaussian 03 and 09 program packages,[18] where the numerical integrals were calculated with the "UltraFine grid" (99 × 590) and the geometry optimizations were carried out in the "VeryTight" convergence criteria in the Gaussian programs. The evaluated frequencies and force constants were corrected with scaling factors, 0.9573 and 0.9164, respectively.[19] Molecular orbitals were drawn by the MOLEKEL program.[20]

5.2.2. Procedure to Evaluate Oscillator Strength of Symmetry-Forbidden d–d Transition

To calculate the oscillator strength explicitly, we need vibrational wave functions at the ground and excited states. However, it is not easy to calculate the potential energy surface and vibrational wave function in the excited states of $[Co(NH_3)_6]^{3+}$ and the Rh analogue because their excited states induce the Jahn–Teller distortion. Here, we wish to propose an approximate way to evaluate the oscillator strength of the symmetry-forbidden d–d transition. In our method, the oscillator strength is calculated with distorted geometry along the normal coordinate of fundamental vibration, as will be discussed below. This is the same as the usual calculation of symmetry-allowed transition in which the Franck–Condon factor is not considered explicity but assumed to be 1.0. However, the potential energy surface and the vibrational wave function of the excited state were not considered in our method.[21] Because of these approximations, our method is not perfect and its application is limited; for instance, it can not be applied to the evaluation of shape and vibrational structure of absorption spectrum which arises from vibronic coupling. Also,

the present method is not useful to make a comparison of absorption spectrum between two complexes when the potential energy surface in the excited state is considerably different between them. In addition, note that, in our method, the Jahn–Teller effect of the excited state is ignored,[21] which influences the absorption spectrum.[22] Despite of these defects, we believe that the present procedure has some practical merit.

As well-known, the probability $g_{i,n}(Q_i)$ of distorted geometry is determined by the square of the vibrational wave function $\chi_{i,n}(Q_i)$;[21]

$$g_{i,n}(Q_i) = \left|\chi_{i,n}(Q_i)\right|^2 \tag{1}$$

where n (= 0, 1, 2,...) is quantum number of the vibrational wave function and Q_i is normal mode coordinate associated with the fundamental vibration mode i. Equilibrium geometry corresponds to $Q_i = 0$. The probability of distorted geometry in zero-point vibration is schematically shown in Scheme 1a, as an example.

The inversion center of the octahedral complex disappears with some of molecular vibrations. In such distorted geometry, the oscillator strengths of the $^1A_{1g} \rightarrow {}^1T_{1g}$ and $^1A_{1g} \rightarrow {}^1T_{2g}$ transitions become nonzero.[9] The oscillator strength $f_{dist,i}(Q_i)$ at distorted geometry Q_i was calculated with the TD-DFT method,[23] where the distorted geometrical coordinate Q_i was determined along the normal mode i at an appropriate interval; note that the normal mode i is provided by the Gaussian program package, where the harmonic oscillator approximation is employed. All vibration modes were considered unless otherwise the contribution to the distorted geometry is negligibly small; See Appendix for details of evaluation of $f_{dist,i}(Q_i)$.

The oscillator strength $f_{i,n}$ induced by vibration mode i with quantum number n is represented by the integral of the product of $f_{dist,i}(Q_i)$ and $g_{i,n}(Q_i)$, as shown by eq 2;

$$f_{i,n} = \int_{-\infty}^{\infty} g_{i,n}(Q_i)\, f_{dist,i}(Q_i)\, dQ_i \tag{2}$$

For instance, the $f_{i,0}$ value corresponds to a dark area in Scheme 1c. This integral was calculated numerically; see also Appendix.

Scheme 1.

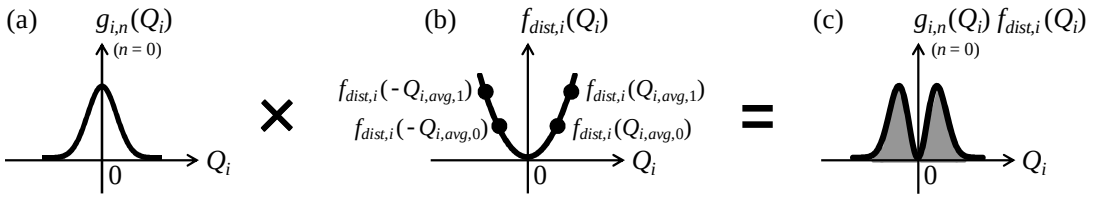

Probability of distorted geometry by zero-point vibration

Oscillator strength as a function of coordinate Q_i

Dark area indicates corresponds $f_{i,n=0}$ in eq 2.

The population $P_{i,n}$ of the n-th vibrationally excited state in the vibration mode i depends on temperature T, according to the Boltzmann distribution law. Because the harmonic oscillator approximation is employed here, the population $P_{i,n}$ is described by eq 3

$$P_{i,n}(T) = \frac{\exp[-(n+1/2)\hbar\omega_i/(k_B T)]}{\sum_{j=0}^{\infty}\exp[-(j+1/2)\hbar\omega_i/(k_B T)]} \tag{3}$$

where k_B is the Boltzmann constant, $\hbar$ is the reduced Planck constant, and ω_i is the frequency of vibration of mode i. The oscillator strength $f_i(T)$ induced by vibration mode i at temperature T is represented by the sum of the product of $f_{i,n}$ and $P_{i,n}(T)$;

$$f_i(T) = \sum_{n=0}^{\infty} P_{i,n}(T)\, f_{i,n} \tag{4}$$

The sum of the $f_i(T)$ values on all fundamental vibrations corresponds to the total oscillator strength $f(T)$ at temperature T

$$f(T) = \sum_{i}^{all} f_i(T) \tag{5}$$

Here, the mode coupling is not considered after checking that it is not large; see Appendix page S4. Two-photon excitation is not considered also, indicating that some of intensity is missed.

5.3. Results and Discussion

5.3.1. Optimized Geometries and d–d Absorption Spectra of $[Co(NH_3)_6]^{3+}$ and $[Rh(NH_3)_6]^{3+}$

Optimized M–N bond lengths of $[Co(NH_3)_6]^{3+}$ and $[Rh(NH_3)_6]^{3+}$ are 2.009 and 2.113 Å, respectively, as shown in Table 1, which agree well with the experimental values (1.967 and 2.071 Å).[24,25] The excitation energies of $[Co(NH_3)_6]^{3+}$ are evaluated to be 2.61 and 3.62 eV for the $^1A_{1g} \rightarrow {}^1T_{1g}$ and $^1A_{1g} \rightarrow {}^1T_{2g}$ transitions, respectively, which also agree well with the experimental values (2.62 and 3.67 eV).[26] Those of $[Rh(NH_3)_6]^{3+}$ are evaluated to be 3.92 and 4.54 eV for the $^1A_{1g} \rightarrow {}^1T_{1g}$ and $^1A_{1g} \rightarrow {}^1T_{2g}$ transitions, respectively. The former energy is almost the same as the experimental value (4.03 eV).[27] Though the latter one is moderately lower than the experimental value (4.86 eV),[27] the difference is not large (about 0.3 eV).

The oscillator strengths of $[Co(NH_3)_6]^{3+}$ at 293 K are evaluated to be 11.1×10^{-4} and 8.1×10^{-4} for the $^1A_{1g} \rightarrow {}^1T_{1g}$ and $^1A_{1g} \rightarrow {}^1T_{2g}$ transitions, respectively, as shown in Table 2. These results agree well with the experimental values (11×10^{-4} and 9×10^{-4}).[26]

Table 1. Optimized bond lengths (in Å) and absorption energies (in eV) of $[Co(NH_3)_6]^{3+}$ and $[Rh(NH_3)_6]^{3+}$

		calcd	exptl
$[Co(NH_3)_6]^{3+}$	r(Co–O)	2.009	1.967[a]
	$\Delta E(^1A_{1g} \rightarrow {}^1T_{1g})$	2.61	2.62[b]
	$\Delta E(^1A_{1g} \rightarrow {}^1T_{2g})$	3.62	3.67[b]
$[Rh(NH_3)_6]^{3+}$	r(Rh–O)	2.113	2.071[c]
	$\Delta E(^1A_{1g} \rightarrow {}^1T_{1g})$	3.92	4.03[d]
	$\Delta E(^1A_{1g} \rightarrow {}^1T_{1g})$	4.54	4.86[d]

(a) Ref 24. (b) Ref 26. These absorption energies were measured in 5.0 M ammonia–water at 293 K. (c) Ref 25. (d) Ref 27. These absorption energies were measured in aqueous solution at room temperature.

Table 2. Oscillator strengths (in $\times 10^{-4}$) of the $^1A_{1g} \rightarrow {}^1T_{1g}$ and $^1A_{1g} \rightarrow {}^1T_{2g}$ absorptions of $[Co(NH_3)_6]^{3+}$ and $[Rh(NH_3)_6]^{3+}$

	$[Co(NH_3)_6]^{3+}$				$[Rh(NH_3)_6]^{3+}$			
	0 K		293 K		0 K		293 K	
	$^1T_{1g}$	$^1T_{2g}$	$^1T_{1g}$	$^1T_{2g}$	$^1T_{1g}$	$^1T_{2g}$	$^1T_{1g}$	$^1T_{2g}$
experimental oscillator strength			11[a]	9[a]			36[b]	27[b]
calculated oscillator strength	4.6	4.1	11.1	8.1	11.7	7.6	22.7	13.0
details of the calculated oscillator strength								
$M–NH_3$ asym deg stretching (T_{1u}) (3)[c,d]	0.0	0.5	0.0	0.8	0.2	0.7	0.3	1.0
$H_3N–M–NH_3$ asym deg bending (T_{1u}) (3)[c,d]	1.2	0.8	1.9	1.4	3.0	2.0	5.4	3.6
$H_3N–M–NH_3$ asym deg bending (T_{2u}) (3)[c,d]	0.8	0.6	1.7	1.3	2.3	1.2	5.2	2.6
rotational vibration around $M–NH_3$ axis (3)[d]	0.5	0.3	5.2	2.8	0.6	0.3	6.0	2.3
$M–NH_3$ wagging (6)[d]	1.7	1.4	1.8	1.5	4.1	2.5	4.3	2.6
N–H stretching in NH_3 ligands (9)[d]	0.3	0.3	0.3	0.3	1.2	0.7	1.2	0.7
H–N–H bending in NH_3 ligand (9)[d]	0.2	0.2	0.2	0.2	0.4	0.3	0.4	0.3

(a) Ref 26. These absorption spectra were measured in 5.0 M ammonia–water at 293 K. (b) Ref 27. These absorption spectra were measured in aqueous solution at room temperature. (c) The term “asym deg” means “antisymmetric degenerate”. (d) Numbers in parentheses represent numbers of fundamental vibration modes bearing the ungerade symmetry. Calculated oscillator strengths are the sum of the oscillator strengths provided by each fundamental vibration. See footnote 29 for details.

In $[Rh(NH_3)_6]^{3+}$, the oscillator strengths are evaluated to be 22.7×10^{-4} and 13.0×10^{-4} for the $^1A_{1g} \rightarrow {}^1T_{1g}$ and $^1A_{1g} \rightarrow {}^1T_{2g}$ transitions, respectively. Though these values are somewhat smaller than the experimental values (36×10^{-4} and 27×10^{-4}),[27,28] the experimental trend of the oscillator strength is reproduced well, as follows: In both of experimental and theoretical results, the oscillator strengths of the $^1A_{1g} \rightarrow {}^1T_{1g}$ transitions of $[Co(NH_3)_6]^{3+}$ and $[Rh(NH_3)_6]^{3+}$ are somewhat larger than those of the $^1A_{1g} \rightarrow {}^1T_{2g}$ transitions and the oscillator strengths of $[Rh(NH_3)_6]^{3+}$ are considerably larger than those of $[Co(NH_3)_6]^{3+}$ in both of the $^1A_{1g} \rightarrow {}^1T_{1g}$ and $^1A_{1g} \rightarrow {}^1T_{2g}$ transitions. These results indicate that our method is useful in evaluating and discussing the oscillator strength of the symmetry-forbidden d–d absorption, at least semiquantitatively.

5.3.2. Oscillator Strength at 0 K and Contributions of Various Molecular Vibration Modes

It is of considerable interest to investigate whether or not the symmetry-forbidden d–d absorption can be observed at 0 K because vibration does not occur at 0 K in a classical sense. However, the oscillator strength of $[Co(NH_3)_6]^{3+}$ is evaluated to be 4.6×10^{-4} and 4.1×10^{-4} for the $^1A_{1g} \rightarrow {}^1T_{1g}$ and $^1A_{1g} \rightarrow {}^1T_{2g}$ transitions, respectively, at 0 K, as shown in Table 2, though they are considerably smaller than those at 293 K (11.1×10^{-4} and 8.1×10^{-4}), as expected. The oscillator strength of $[Rh(NH_3)_6]^{3+}$ at 0 K is evaluated to be 11.7×10^{-4} and 7.6×10^{-4} for the $^1T_{1g}$ and $^1T_{2g}$ transitions, respectively, which are also considerably smaller than the values at 293 K (22.7×10^{-4} and 13.0×10^{-4}). It is noted that though these oscillator strengths at 0 K are considerably smaller than at 298 K they are not negligibly small but instead are 40 to 60 % of the oscillator strengths at 298 K. This means that the symmetry-forbidden d–d absorption can be observed even at 0 K. This is because the zero-point vibration provides the distribution of distorted geometry around the equilibrium geometry even at 0 K, which corresponds to the uncertainty of geometry around the

equilibrium geometry at 0 K. Such distribution of distorted geometry contributes to the oscillator strength of the symmetry-forbidden d-δ transition. In other words, the zero-point vibration plays an important role in the symmetry-forbidden d–d transition.

It is of considerable interest to clarify what vibration mode contributes to the oscillator strength at 0 K. In the octahedral molecule, there are such six fundamental vibration modes as the symmetric stretching mode (A_{1g}), symmetric degenerate stretching mode (E_g), symmetric degenerate bending mode (T_{2g}), antisymmetric degenerate stretching mode (T_{1u}), and two kinds of antisymmetric degenerate bending modes (T_{1u} and T_{2u}),[29] as shown in Schemes 2a and 2b. Because the symmetry of the former three vibrational modes is gerade, the oscillator strength is not provided at all by these vibration modes. On the other hand, the latter three vibrational modes, whose symmetry is ungerade, contribute to the oscillator strengths of the symmetry-forbidden d–d transition. In $[Co(NH_3)_6]^{3+}$, two kinds of degenerate antisymmetric $H_3N–Co–NH_3$ bending vibrations of T_{1u} and T_{2u} considerably contribute to the oscillator strength of the d–d absorption at 0 K, as shown in Table 2, because the considerably large geometrical distortion is induced by these vibrations; the oscillator strength induced by the T_{1u} bending mode is 1.2×10^{-4} and 0.8×10^{-4} for the $^1A_{1g} \rightarrow {}^1T_{1g}$ and $^1A_{1g} \rightarrow {}^1T_{2g}$ transitions, respectively, and that induced by the T_{2u} bending mode is 0.8×10^{-4} and 0.6×10^{-4} for the $^1A_{1g} \rightarrow {}^1T_{1g}$ and $^1A_{1g} \rightarrow {}^1T_{2g}$ transitions.[29] On the other hand, the degenerate antisymmetric $Co–NH_3$ stretching vibration mode of T_{1u} contributes much less to the oscillator strength because the distortion is not large; for instance, the oscillator strength induced by this vibration mode is 0.0 and 0.5×10^{-4} for the $^1A_{1g} \rightarrow {}^1T_{1g}$ and $^1A_{1g} \rightarrow {}^1T_{2g}$ transitions, respectively.

There are several other vibration modes which induce little distortion from the octahedral geometry. One of such vibration modes is the $M–NH_3$ wagging mode; see Scheme 2c. Interestingly, this vibration mode contributes considerably to the oscillator strength of the d–d absorption, as follows; the oscillator strength induced by this vibration

mode is 1.7×10^{-4} and 1.4×10^{-4} for the $^1A_{1g} \rightarrow {}^1T_{1g}$ and $^1A_{1g} \rightarrow {}^1T_{2g}$ transitions, respectively, in $[Co(NH_3)_6]^{3+}$ at 0 K, as shown in Table 2. Also, the M–NH_3 rotational vibration around the M–NH_3 bond axis (Scheme 2c)[30] contributes somewhat to the oscillator strength at 0 K, though this vibration distorts the octahedral geometry much less than the M–NH_3 wagging mode; the oscillator strength induced by this vibration mode is evaluated to be 0.5×10^{-4} and 0.3×10^{-4} for the $^1A_{1g} \rightarrow {}^1T_{1g}$ and $^1A_{1g} \rightarrow {}^1T_{2g}$ transitions, respectively, as shown in Table 2.

Not only the M–NH_3 bonds but also the N−H bonds of the NH_3 ligands contribute to oscillator strength. Such vibrations are N–H stretching and H–N–H bending modes. As shown in Table 2, the oscillator strengths induced by the N–H stretching and H–N–H bending modes are evaluated to be 0.3×10^{-4} and 0.2×10^{-4} for the $^1A_{1g} \rightarrow {}^1T_{1g}$ and $^1A_{1g} \rightarrow {}^1T_{2g}$ transitions, respectively, at 0 K. In other words, both vibration modes contribute somewhat to the oscillator strength of the d–d transitions of $[Co(NH_3)_6]^{3+}$.

In $[Rh(NH_3)_6]^{3+}$, the molecular vibrations contribute similarly to the oscillator strength at 0 K like in the Co analogue, as follows: Two kinds of degenerate antisymmetric H_3N–Rh–NH_3 bending modes (T_{1u} and T_{2u}) contribute considerably to the oscillator strengths of the $^1A_{1g} \rightarrow {}^1T_{1g}$ and $^1A_{1g} \rightarrow {}^1T_{2g}$ transitions, as shown in Table 2.[31] On the other hand, the degenerate antisymmetric Rh–NH_3 stretching mode of T_{1u} contributes little to the oscillator strength. The Rh–NH_3 wagging vibration contributes considerably to the oscillator strength, though this vibration distorts little the octahedral geometry. The Rh–NH_3 rotational vibration around the Rh–NH_3 axis and the vibrations in the NH_3 ligand moieties contribute somewhat to the oscillator strength of the d–d transition at 0 K.

Scheme 2.

(a) Characteristic vibration modes of octahedral molecule with gerade symmetry

symmetric stretching (A_{1g})

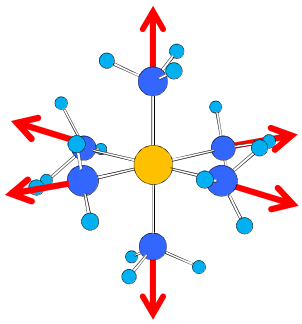

symmetric degenerate stretching (E_g)

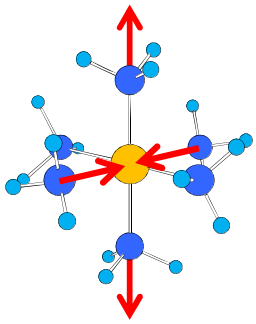

symmetric degenerate vending (T_{2g})

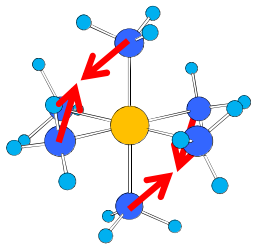

(b) Characteristic vibration modes of octahedral molecule with ungerade symmetry

antisymmetric degenerate stretching (T_{1u})

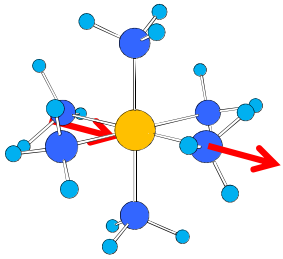

antisymmetric degenerate vending (T_{1u})

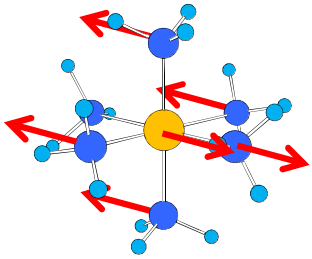

antisymmetric degenerate vending (T_{2u})

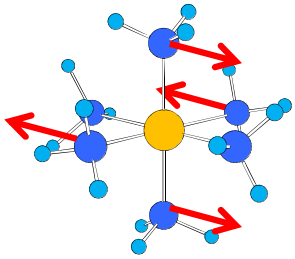

(c) Other vibration modes

rotational vibration around M-NH_3 axis

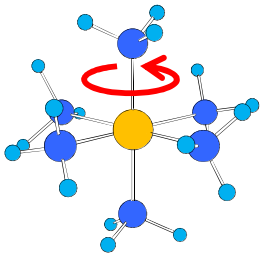

M-NH_3 wagging

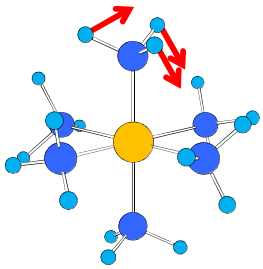

Though only one M-NH_3 ligand vibrates in left schemes for brevity, six M-NH_3 ligands vibrate in real molecule.

5.3.3. Temperature Dependence of Oscillator Strength

Here, we wish to discuss what vibration mode contributes to the increase in oscillator strength by temperature. The rotational vibrations around the M–NH_3 bond axis significantly increase the oscillator strength; for instance, these vibrations increase the oscillator strength from 0.5×10^{-4} and 0.3×10^{-4} to 5.2×10^{-4} and 2.8×10^{-4} for the $^1A_{1g} \rightarrow {}^1T_{1g}$ and $^1A_{1g} \rightarrow {}^1T_{2g}$ transitions, respectively, in $[Co(NH_3)_6]^{3+}$, when going from 0 to 293 K, as shown in Table 2. The significantly large increases by these vibrations arise from their very small wavenumbers of 42–128 and 47–107 cm^{-1} in $[Co(NH_3)_6]^{3+}$ and $[Rh(NH_3)^6]^{3+}$, respectively, as shown in Table 3.[29,30] Because of such small wavenumbers, the population of the vibrationally excited states considerably increases, when going from 0 to 293 K; for instance, these populations are 0.53–0.81 and 0.59–0.79 in $[Co(NH_3)_6]^{3+}$ and $[Rh(NH_3)_6]^{3+}$, respectively, at 293 K, which are much larger than their populations at the vibrational ground state, as shown in Table 3. Because the probability of the distorted geometry is much larger in the vibrationally excited state than in the ground state, the rotational vibration around the M–NH_3 bond axis contributes considerably to the oscillator strength at 293 K.

Besides the M–NH_3 rotational vibration, two kinds of H_3N–M–NH_3 antisymmetric bending vibrations of T_{1u} and T_{2u} moderately contribute to the increase in the oscillator strength, when going from 0 to 293 K, as shown in Table 2. The increase in the oscillator strength by these vibrations is somewhat smaller than that by the M–NH_3 rotational vibration. This is because the wavenumbers of these H_3N–M–NH_3 antisymmetric bending vibrations are much larger than that of the M–NH_3 rotational vibration, as shown in Table 3. As a result, the populations (0.24 in the T_{1u} mode and 0.36–0.38 in the T_{2u} mode) of the vibrationally excited states are much smaller in these antisymmetric bending vibrations than in the rotational vibration (0.53–0.81), and hence, the oscillator strength moderately increases by these bending vibrations when temperature goes up.

Table 3. Wavenumbers (in cm^{-1}) and populations of the ground and excited vibrational states at 293 K

	$[Co(NH_3)_6]^{3+}$			$[Rh(NH_3)_6]^{3+}$		
		population			population	
	wavenumber[a]	ground state	excited state[b]	wavenumber[a]	ground state	excited state[b]
$M–NH_3$ asym deg stretching (T_{1u}) (3)[c,d]	400–402	0.86	0.14	395–397	0.86	0.14
$H_3N–M–NH_3$ asym deg bending (T_{1u}) (3)[c,d]	288–289	0.76	0.24	254–255	0.71	0.29
$H_3N–M–NH_3$ asym deg bending (T_{2u}) (3)[c,d]	199–209	0.62–0.64	0.36–0.38	189–196	0.61–0.62	0.38–0.39
rotational vibration around $M–NH_3$ axis (3)[d]	42–128	0.19–0.47	0.53–0.81	47–107	0.21–0.41	0.69–0.79
$M–NH_3$ wagging (6)[d]	702–765	0.97–0.98	0.02–.03	732–774	0.97–0.98	0.02–0.03
N–H stretching in NH_3 ligands (9)[d]	3260–3345	1.00	0.00	3260–3344	1.00	0.00
H–N–H bending in NH_3 ligand (9)[d]	1340–1606	1.00	0.00	1344–1602	1.00	0.00

(a) See refs 30 and 31 for details. (b) This population corresponds to the sum of the populations of the all vibrational excited states (n = 1, 2, 3,...). (c) The term “asym deg” means “antisymmetric degenerate”. (d) Numbers in parentheses represent the numbers of fundamental vibration modes bearing the ungerade symmetry.

The wavenumber of the degenerate antisymmetric M–NH_3 stretching vibration is 400–402 cm^{-1} and 395–397 cm^{-1} in $[Co(NH_3)_6]^{3+}$ and $[Rh(NH_3)_6]^{3+}$, respectively,[31] which are considerably larger than those of the degenerate antisymmetric H_3N–M–NH_3 bending vibration and the M–NH_3 rotational vibration; see Table 3. The population of this vibrationally excited states is small (0.14) at 293 K in both complexes, as shown in Table 2. Thus, the degenerate antisymmetric M–NH_3 stretching vibration contributes much less to the increase in the oscillator strength than the degenerate antisymmetric H_3N–M–NH_3 bending and the M–NH_3 rotational vibrations, when going from 0 to 293 K; actually, this vibration increases the oscillator strength of the $^1A_{1g} \rightarrow {}^1T_{1g}$ transition by only 0.3×10^{-4} in $[Co(NH_3)_6]^{3+}$, as shown in Table 3. On the basis of these results, it is concluded that the degenerate antisymmetric M–NH_3 stretching mode contributes little to the oscillator strength of the d–d absorption at both 0 and 293 K, though the molecular distortion from the octahedral geometry is somewhat largely induced by this vibration mode.

The wavenumbers of the M–NH_3 wagging, N–H stretching, and N–H bending vibrations are significantly large, being more than 700 cm^{-1} in both of $[Co(NH_3)_6]^{3+}$ and $[Rh(NH_3)_6]^{3+}$, as shown in Table 3. Thus, the populations in their vibrationally excited states are nearly zero even at 293 K, and hence, these vibration modes contribute little to the increase in the oscillator strength, when going from 0 to 293 K.

5.3.4. MLCT Character in Symmetry-Forbidden d–d Transition

The t_{2g} and e_g Kohn–Sham orbitals of $[Co(NH_3)_6]^{3+}$ and $[Rh(NH_3)_6]^{3+}$ are presented in Figure 1. The e_g orbitals mainly consist of the d orbital of the metal center and moderately of the lone-pair orbitals of the NH_3 ligands, whereas the t_{2g} orbitals consist of the d orbital of the metal center only. This means that the $^1A_{1g} \rightarrow {}^1T_{1g}$ and $^1A_{1g} \rightarrow {}^1T_{2g}$ transitions moderately contain metal-to-ligand charge transfer (MLCT) character from the d_{xy}, d_{yz}, and d_{xz} orbitals of the metal center to the lone-pair orbital of NH_3 ligand.

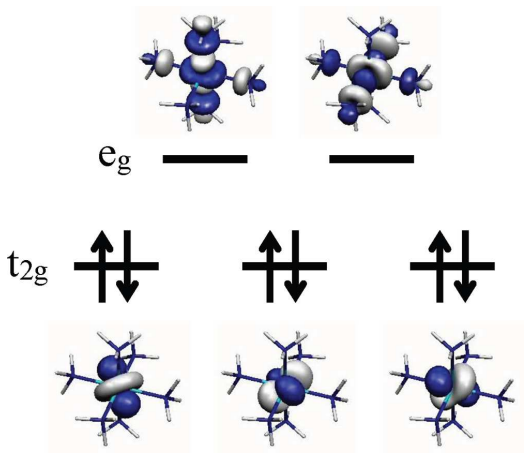

Figure 1. Kohn–Sham orbitals of $[Co(NH_3)_6]^{3+}$

Table 4. Mulliken populations of Co, Rh, N, and H atoms[a] in the $^1A_{1g}$, $^1T_{1g}$, and $^1T_{2g}$ states of $[Co(NH_3)_6]^{3+}$ and $[Rh(NH_3)_6]^{3+}$

		Mulliken population			change of Mulliken population	
		$^1A_{1g}$	$^1T_{1g}$	$^1T_{2g}$	$^1A_{1g} \rightarrow {}^1T_{1g}$	$^1A_{1g} \rightarrow {}^1T_{2g}$
$[Co(NH_3)_6]^{3+}$	Co	27.064	26.997	27.019	–0.067	–0.045
	N	7.059	7.073	7.069	+0.014	+0.010
	H	0.810	0.809	0.809	–0.001	–0.001
$[Rh(NH_3)_6]^{3+}$	Rh	44.980	44.826	44.848	–0.154	–0.132
	N	7.102	7.129	7.125	+0.027	+0.023
	H	0.801	0.800	0.800	–0.001	–0.001

(a) Averaged values of six N atoms and eighteen H atoms are presented here.

This MLCT character is larger in the $^1A_{1g} \rightarrow {}^1T_{1g}$ transition than in the $^1A_{1g} \rightarrow {}^1T_{2g}$ transition, as follows: In both of $[Co(NH_3)_6]^{3+}$ and the Rh analogue, the $^1A_{1g} \rightarrow {}^1T_{1g}$ transition decreases more the M atomic population and increases more the N atomic population than does the $^1A_{1g} \rightarrow {}^1T_{2g}$ transition, as shown in Table 4, where the Mulliken population analysis was employed; note that the change in the N atomic population directly relates to the extent of the CT to the lone pair orbital of NH_3.[32] Also, the $^1A_{1g} \rightarrow {}^1T_{1g}$ and $^1A_{1g} \rightarrow {}^1T_{2g}$ transitions decrease more the M atomic population and increase more the N atomic population in $[Rh(NH_3)_6]^{3+}$ than in $[Co(NH_3)_6]^{3+}$, as shown in Table 4. These results indicate that the MLCT character is larger in the $^1A_{1g} \rightarrow {}^1T_{1g}$ transition than in the $^1A_{1g} \rightarrow {}^1T_{2g}$ transition and larger in the d–d transitions of $[Rh(NH_3)_6]^{3+}$ than in those of $[Co(NH_3)_6]^{3+}$.

As the MLCT character increases, the oscillator strength increases in general. Actually, the extent of the MLCT character in the d–d transition is parallel to the oscillator strength of the d–d transition; remember that the oscillator strength of the $^1A_{1g} \rightarrow {}^1T_{1g}$ transition is larger than that of the $^1A_{1g} \rightarrow {}^1T_{2g}$ transition, and both of their oscillator strengths are larger in $[Rh(NH_3)_6]^{3+}$ than in $[Co(NH_3)_6]^{3+}$.

We wish to mention here the reason why the MLCT character is larger in the symmetry-forbidden d–d transition of $[Rh(NH_3)_6)]^{3+}$ than in that of $[Co(NH_3)_6)]^{3+}$. In general, the 4d transition metal forms stronger coordinate bond than the 3d transition metal because the 4d orbital expands more widely than the 3d orbital.[33] As a result, the 4d orbital of Rh overlaps with the lone pair orbital of NH_3 more than the 3d orbital of Co does, which leads to larger mixing of the NH_3 lone pair orbital into the d_{eg} orbital in the Rh complex than in the Co analogue. Thus, the MLCT character is larger in the Rh complex than in the Co complex, which is responsible for the larger oscillator strengths of $[Rh(NH_3)_6)]^{3+}$ than those of $[Co(NH_3)_6)]^{3+}$.

5.4. Conclusions

We proposed here a new method to evaluate the oscillator strength of the symmetry-forbidden d-d transition of the transition metal complex bearing the inversion symmetry. In this method, the probability of distorted geometry is evaluated with the vibrational wave function, and the Boltzmann distribution law is employed to evaluate the population of the vibrationally excited state. The Herzberg–Teller approximation is not necessary here. We applied this method to the symmetry-forbidden d–d absorptions of such octahedral complexes as $[Co(NH_3)_6]^{3+}$ and $[Rh(NH_3)_6]^{3+}$. The present calculations reproduce the experimental results,[26,27] as follows: (i) The oscillator strengths of the $^1A_{1g} \rightarrow {}^1T_{1g}$ and $^1A_{1g} \rightarrow {}^1T_{2g}$ transitions agree well with the experimental results in $[Co(NH_3)_6]^{3+}$, while those of the Rh analogue are somewhat smaller than the experimental results. (ii) The oscillator strength of the $^1A_{1g} \rightarrow {}^1T_{1g}$ transition is considerably larger than that of the $^1A_{1g} \rightarrow {}^1T_{2g}$ transition in both of $[Co(NH_3)_6]^{3+}$ and $[Rh(NH_3)_6]^{3+}$. And, (iii) the oscillator strengths of these transitions are considerably larger in the Rh complex than in the Co complex.

In these complexes, the $H_3N–M–NH_3$ antisymmetric bending vibration (M = Co or Rh) contributes considerably to the oscillator strength of the d–d transition because the geometrical distortion is largely induced by this vibration. It is also noted that the $M–NH_3$ wagging vibration contributes considerably to the oscillator strength despite of moderate lowering of symmetry by this vibration and that the $M–NH_3$ antisymmetric stretching vibration contributes little to the oscillator strength despite of considerable lowering of symmetry by this vibration.

Interestingly, the oscillator strengths of the $^1A_{1g} \rightarrow {}^1T_{1g}$ and $^1A_{1g} \rightarrow {}^1T_{2g}$ transitions are evaluated to be considerably large even at 0 K in these complexes. The distorted geometry (or the geometry uncertainty) by the zero-point vibration is responsible for the oscillator strength of the symmetry-forbidden d–d transition at 0 K. When temperature

goes up to 293 K, the oscillator strength increases. This increase in the oscillator strength is mainly induced by the $H_3N–M–NH_3$ antisymmetric degenerate bending vibrations of T_{1u} and T_{2u} symmetries, $M–NH_3$ wagging vibration, and $M–NH_3$ rotational vibration around the $M–NH_3$ bond axis. The MLCT character, which is involved in the symmetry-forbidden d–d transition, contributes to the oscillator strength of the d–d absorption. This character is larger in $[Rh(NH_3)_6]^{3+}$ than in $[Co(NH_3)_6]^{3+}$.

These results indicate that our method is useful in evaluating and understanding the oscillator strength of the symmetry-forbidden d–d transition. Our procedure is much simpler than the method with MD simulation and the Herzberg–Teller approximation. Though our procedure needs to calculate $f_{dist,i}(Q_i)$ value at many Q_i points, we can reduce this computation; see Appendix. At the end of this chapter, we wish to note again the presence of several weak-points in our method; see the section “Method and Computational Details”.

5.5. Appedix

Details of Computational Procedure of Oscillator Strength

The interval of Q_i was determined as follows:

A small interval leads to correct value but we need large computational cost for too small interval. We calculated square of vibrational wavefunction at appropriate interval of the coordinate Q_i and evaluated its root mean square value, where we employed vibrationally ground state wavefunction (quantum number of vibration, n = 0) at the electronic ground state. This is because the vibrationally ground state is the most important to determine the distorted geometry distribution. The Q_i^{rms} value which provides this root mean square value was evaluated for n = 0. The interval was taken to be one twentieth of Q_i^{rms}; we checked that the computation result little changed when the interval was decreased.

The integration of eq 2

The integration was performed with enough range; we expanded integration range until the integral value does not increase by expanding the integration range.

The neglect of vibration mode whose frequency is large

We consider all vibration modes including soft modes. However, we neglected the vibration mode when its frequency is large and it little contributes to the distorted geometry after checking if the oscillator strength by this mode is negligibly small.

The neglect of mode coupling

The anharmonicity of mode coupling is neglected, here. However, we checked the potential energy surface (PES) along the coordinate of typical fundamental mode but the PES is almost parabolic. This result suggests that the vibration occurs in a harmonic manner and the mode-coupling is not large.

Evaluation of Oscillator Strength $f_{dist,i}(Q_i)$ with Relation $f_{dist,i}(Q_i) = a_i Q_i^2$

In our procedure, the $f_{dist,i}(Q_i)$ value must be calculated at many normal mode coordiante Q_i. This is troublesome and time-consuming. However, this weakpoint can be solved as follows:

In the Hertzberg–Teller approximation, the transition dipole moment of the symmetry-forbidden d–d transition is represented as a linear function of a normal mode coordinate Q_i.[7] Because the oscillator strength is proportional to the square of the transition dipole moment, the oscillator strength $f_{dist,i}(Q_i)$ is presented by a quadratic function of the normal mode coordinate Q_i under the Hertzberg–Teller approximation; in other words, the oscillator strength is represented by eq A1;

$$f_{dist,i} = a_i Q_i^2 \tag{A1}$$

where a_i is a coefficient. To evaluate the $f_{dist,i}(Q_i)$ value with eq A1, we need to determine the coefficient a_i value. Because it is likely that the use of small $f_{dist,i}(Q_i)$ value for the evaluation of a_i gives rise to large numerical error, we must employ an appropriate Q_i value for the evaluation of the a_i value. To determine such Q_i value, eq A2 was employed here;

$$Q_{i,avg,n} = \left(\int_{-\infty}^{\infty} \chi_{i,n}^{*}(Q_i) Q_i^2 \chi_{i,n}(Q_i) dQ_i \right)^{\frac{1}{2}} \tag{A2}$$

This eq 7 presents a mean value of Q_i in a fundamental vibration i. Here, we employed the vibration wavefunctions of the ground (n = 0) and the first-excited (n = 1) states because the population of thermally excited state steeply decreases as the vibration quantum number increases. Next step is to calculate oscillator strength by the TD-DFT(B3PW91) method at $Q_i = \pm Q_{i,avg,0}$ and $\pm Q_{i,avg,1}$. From these calculated $f_{dist,i}(\pm Q_{i,avg,0})$ and $f_{dist,i}$ $(\pm Q_{i,avg,1})$ values,[20] the a_i value was determined with the least square fitting, as shown in Scheme 1b. With thus-obtained a_i value, the $f_{dist,i}$ (Q_i) value was estimated by eq A1.

This procedure presents almost the same oscillator strength shown in Table 2, indicating that we can reduce computational time by using this procedure.

References and Notes

(1) Grimme, S. *Rev. Comput. Chem.* **2004**, *20*, 153.

(2) Ehara, M.; Hasegawa, J.; Nakatsuji, H. *SAC-CI method applied to molecular spectroscopy*. In *Theory and Applications of Computatinal Chemistry: The First Forty Years*; Dyksrtra, C. E., Frenking, F., Kim, K. S., Scuseria, G. E., Eds.; Elsevier: Oxford, U.K., 2005; p 1099.

(3) Figgs, B. N.; Hitchman, M. A. *Ligand-Field Theory and its Applications*; Wiley: New York, 2000.

(4) Sugano, S.; Tanabe, Y.; Kamimura, H. *Multiplets of Transition-metal Ions in Crystals*; Academic Press Inc.: New York, 1970.

(5) (a) Iuchi, S.; Morita, A.; Kato, S. *J. Chem. Phys.* **2004**, *121*, 8446. (b) Iuchi, S.; Sakaki, S. *Chem. Phys. Lett.* **2010**, *485*, 114.

(6) Bridgeman, A. *J. Inorg. Chem.* **2008**, *47*, 4817.

(7) Hertzberg, G.; Teller, E. *Z. Phys. Chem., Abt. B* **1933**, *21*, 410.

(8) According to the Herzberg□Teller (HT) approximation, the transition dipole M is represented, as follows; $M = M(0) + \Sigma_i (\partial M/\partial Q_i)_0 Q_i$, where the Q_i is the normal coordinate of fundamental vibration mode i and the subscript "0" represents the equilibrium geometry. The transition dipole M is calculated, as follows: $M = \Sigma_i (\partial M/\partial Qi)_0 <\chi_{0,i}(Q_i)|Q_i|\chi_{e,i}(Q_i)>$, where $\chi_{0,i}$ and $\chi_{e,i}$ represent fundamental vibrational functions at the electronic ground and the excited states, respectivey.

(9) $[Co(NH_3)_6]^{3+}$ and $[Rh(NH_3)_6]^{3+}$ are not O_h symmetrical strictly speaking but C_i symmetrical in the equilibrium geometry. However, the C_i symmetry arises from the presence of the H atoms of NH_3 ligands, and the main flame is O_h symmetrical. Hence, the terms of $^1A_{1g}$, $^1T_{1g}$, and $^1T_{2g}$ were used here; in other words, the ground state was named as $^1A_{1g}$ and the excited states were named as $^1T_{1g}$ and $^1T_{2g}$ in both of $[Co(NH_3)_6]^{3+}$ and $[Rh(NH_3)_6]^{3+}$.

(10) Dolg, M.; Wedig, U.; Stoll, H. *J. Chem. Phys.* **1987**, *86*, 866.

(11) Andrae, D.; Haeussermann, U.; Dolg, M.; Stoll, H.; Preuss, H. *Theor. Chim. Acta* **1990**, *77*, 123.

(12) Martin, J. M. L.; Sundermann, A. *J. Chem. Phys.* **2001**, *114*, 3408.

(13) Dunning, T. H. Jr. *J. Chem. Phys.* **1989**, *90*, 1007.

(14) (a) Becke, A. D. *Phys. Rev. A* **1988**, *38*, 3098. (b) Becke, A. D. *J. Chem. Phys.* **1993**, *98*, 5648.

(15) Perdew, J. P.; Wang, Y. *Phys. Rev. B* **1992**, *45*, 13244.

(16) Casida, M. E. *Recent Advances in Density Functional Methods, Part I*; Chong, D. P., Ed.; World Scientific: Singapore, 1995.

(17) Gross, E. U. K.; Dobson, J. F.; Petersilka, M. *Density Functional Theory II*; Nalewajski, R. F., Ed.; Springer: Heideberg, Germany, 1996.

(18) (a) Frisch, M. J.; Trucks, G. W.; Schlegel, H. B.; Scuseria, G. E.; Robb, M. A.; Cheeseman, J. R.; Montgomery, Jr., J. A.; Vreven, T.; Kudin, K. N.; Burant, J. C.; Millam, J. M.; Iyengar, S. S.; Tomasi, J.; Barone, V.; Mennucci, B.; Cossi, M.; Scalmani, G.; Rega, N.; Petersson, G. A.; Nakatsuji, H.; Hada, M.;

Ehara, M.; Toyota, K.; Fukuda, R.; Hasegawa, J.; Ishida, M.; Nakajima, T.; Honda, Y.; Kitao, O.; Nakai, H.; Klene, M.; Li, X.; Knox, J. E.; Hratchian, H. P.; Cross, J. B.; Bakken, V.; Adamo, C.; Jaramillo, J.; Gomperts, R.; Stratmann, R. E.; Yazyev, O.; Austin, A. J.; Cammi, R.; Pomelli, C.; Ochterski, J. W.; Ayala, P. Y.; Morokuma, K.; Voth, G. A.; Salvador, P.; Dannenberg, J. J.; Zakrzewski, V. G.; Dapprich, S.; Daniels, A. D.; Strain, M. C.; Farkas, O.; Malick, D. K.; Rabuck, A. D.; Raghavachari, K.; Foresman, J. B.; Ortiz, J. V.; Cui, Q.; Baboul, A. G.; Clifford, S.; Cioslowski, J.; Stefanov, B. B.; Liu, G.; Liashenko, A.; Piskorz, P.; Komaromi, I.; Martin, R. L.; Fox, D. J.; Keith, T.; Al-Laham, M. A.; Peng, C. Y.; Nanayakkara, A.; Challacombe, M.; Gill, P. M. W.; Johnson, B.; Chen, W.; Wong, M. W.; Gonzalez, C.; and Pople, J. A.; *Gaussian 03*, Revision C.02, Gaussian, Inc., Wallingford CT, 2004. (b) Frisch, M. J.; Trucks, G. W.; Schlegel, H. B.; Scuseria, G. E.; Robb, M. A.; Cheeseman, J. R.; Scalmani, G.; Barone, V.; Mennucci, B.; Petersson, G. A.; Nakatsuji, H.; Caricato, M.; Li, X.; Hratchian, H. P.; Izmaylov, A. F.; Bloino, J.; Zheng, G.; Sonnenberg, J. L.; Hada, M.; Ehara, M.; Toyota, K.; Fukuda, R.; Hasegawa, J.; Ishida, M.; Nakajima, T.; Honda, Y.; Kitao, O.; Nakai, H.; Vreven, T.; Montgomery, Jr., J. A.; Peralta, J. E.; Ogliaro, F.; Bearpark, M.; Heyd, J. J.; Brothers, E.; Kudin, K. N.;Staroverov, V. N.; Kobayashi, R.; Normand, J.; Raghavachari, K.; Rendell, A.; Burant, J. C.; Iyengar, S. S.; Tomasi, J.; Cossi, M.; Rega, N.; Millam, N. J.; Klene, M.; Knox, J. E.; Cross, J. B.; Bakken, V.; Adamo, C.; Jaramillo, J.; Gomperts, R.; Stratmann, R. E.; Yazyev, O.; Austin, A. J.; Cammi, R.; Pomelli, C.; Ochterski, J. W.; Martin, R. L.; Morokuma, K.; Zakrzewski, V. G.; Voth, G. A.; Salvador, P.; Dannenberg, J. J.; Dapprich, S.; Daniels, A. D.; Farkas, Ö.; Foresman, J. B.; Ortiz, J. V.; Cioslowski, J.; Fox, D. J. *Gaussian 09*, revision A.02; Gaussian, Inc.: Wallingford, CT, 2009.

(19) Scott, A. P.; Radom, L. *J. Phys. Chem.* **1996**, *100*, 16502.

(20) (a) Flükiger, P.; Lüthi, H. P.; Portmann, S.; Weber, J. *MOLEKEL*, version 4.3; Scientific Computing: Manno, Switzerland, 2000−2002. (b) Portmann, S.; Lüthi, H. P. *CHIMIA* 2000, 54, 766.

(21) We must consider the potential energy surface and vibrational wave function in the excited state, strictly speaking. For instance, a probability of distorted geometry in the excited state, which is given by the $g(Q)$-type function of eq 1, must be considered, because the d−d transition may become allowed due to odd vibrations not only in the ground state but also in the excited state. However, it is not easy to present correctly the potential energy surface of the excited states of $[Co(NH_3)_6]^{3+}$ and the Rh analogue, because we must use the Multi-State-CASPT2 method to evaluate such potential energy surface including the Jahn−Teller distortion; note that the use of Multi-State-CASPT2 calculation of the excited state is not easy. Because of these weak-points discussed here and in the text, we need to further develop the method to incorporate these factors in the future.

(22) (a) Bersuker, I. B.; Polinger, V. Z. *Vibronic Interactions in Molecules and Crystals*; Springer: New York, 1989. (b) Bersuker, I. B. *The Jahn-Teller Effect*; Cambridge University Press: Cambridge, England, 2006. (c) Solomon, E. I.; Hanson, M. A. *Bioinorganic Spectroscopy* In *Inorganic Electronic*

Structure and Spectroscopy, Vol. II: Applications and Case Studies; Solomon, E. I., Lever, A. B. P., Eds.; Wiley: NJ, 2006.

(23) Because the oscillator strengths $f_{dist,i}(\pm Q_{i,avg,0})$ and $f_{dist,i}(\pm Q_{i,avg,1})$ are much small (less than 10^{-4}), these values cannnot be presented by the TD-DFT calculations under the default conditions of Gaussian 03 and 09 programs; for example, the calculated oscillator strength less than 0.00005 is displayed as "0.0000" in the output file of the default Gaussian 03 and 09. To present such small oscillator strengths, we modified the setting of Gaussian 03 and 09.

(24) Meek, D. W.; Ibers, J. A. *Inorg. Chem.* **1970**, *9*, 465.

(25) Kimura, T.; Sakurai, T. *J. Solid. State. Chem.* **1980**, *34*, 369.

(26) (a) Kofod, P. *Inorg. Chem.* **1995**, *34*, 2768. (b) The oscillator strength was evaluated from the spectrum reported here.

(27) (a) Peterson, J. D.; Ford, P. C. *J. Phys. Chem.* **1974**, *78*, 1144. (b) The oscillator strength was evaluated from the spectrum reported here.

(28) (a) One of the plausible origins of the smaller calculated oscillator strength than the experimental value in the Rh complex is the neglect of the spin–orbit interaction, because the spin-forbidden symmetry-allowed state can mix into the spin-allowed symmetry-forbidden d–d excitation state through spin–orbit interaction. The other plausible origin is the weak point of the TD-DFT method.[28b] In general the TD-DFT method tends to present a small transition dipole.[28c] Moreover, in the Rh complex, the d–d transition contains larger CT character than in the Co complex because the orbital overlap between the d orbital and NH_3 lone pair orbital is larger than in the Co complex. The TD-DFT calculation tends to present a poor result for a CT transition[28d] without the range-corrected exchange functional.[28e] (b) Recent review: Cramer, C. J.; Truhlar, D. G. *Phys. Chem. Chem. Phys.* **2009**, *11*, 10757. (c) Appel, F.; Gross, E. K. U.; Burke, K. *Phys. Rev. Lett.* **2003**, *90*, 043005. (d) Dreuw, A.; Weisman, J. L.; Head-Gordon, M. *J. Chem.. Phys.* **2003**, *119*, 2943. (e) Tawada, Y.; Tsuneda, T.; Yanagisawa, S.; Yanai, T.; Hirao, K. *J. Chem. Phys.* **2004**, *120*, 8425.

(29) $[Co(NH_3)_6]^{3+}$ and $[Rh(NH_3)_6]^{3+}$ have three fundamental vibration modes of the T_{1u} $H_3N–M–NH_3$ antisymmetric degenerate bending vibration. Their oscillator strengths presented in Table 2 are the sum of the oscillator strengths provided by three fundamental bending vibrations in the T_{1u} mode; for example, the oscillator strength of the $^1A_{1g} \rightarrow {}^1T_{1g}$ transition of $[Co(NH_3)_6]^{3+}$ by this vibration is 1.2×10^{-4} which is the sum of three oscillator strengths (0.4×10^{-4}) induced by three T_{1u} vibrations.

(30) $[Co(NH_3)_6]^{3+}$ and $[Rh(NH_3)_6]^{3+}$ have three fundamental rotational vibrations around the $M–NH_3$ axis with ungerade symmetry. Wavenumbers of these fundamental vibrations are 42, 44, and 128 cm^{-1} in $[Co(NH_3)_6]^{3+}$ and 47, 48, and 107 cm^{-1} in $[Rh(NH_3)_6]^{3+}$. We reported here their wavenumbers as 42–128 cm^{-1} and 47–107 cm^{-1}, respectively, for brevity. The wavenumbers of the other molecular vibrations are also provided in the similar way.

(31) Because $[Co(NH_3)_6]^{3+}$ and $[Rh(NH_3)_6]^{3+}$ are not completely O_h symmetrical strictly speaking, the $H_3N–M–NH_3$ antisymmetric bending (T_{1u} and T_{2u}) and $M–NH_3$ antisymmetric streching (T_{1u}) vibrations are not completely degenerate. However, these fundamental vibrations exhibit similar frequency values to each other; for example, the wavenumbers of the T_{2u} bending mode are 199, 209, and 209 cm^{-1} in $[Co(NH_3)_6]^{3+}$ and 189, 196, and 196 cm^{-1} in $[Rh(NH_3)_6]^{3+}$, indicating that the discussion can be presented based on the O_h symmetry; see also ref 9.

(32) Because the lone pair orbital of NH_3 participates in the bonding interaction with the d_{eg} orbital of the metal center, the Mulliken population of the H atom hardly changes in both transitions. Thus, the change in N atomic population corresponds to the CT from the NH_3 lone pair to the metal center.

(33) Frenking, G.; Frohlich, N. *Chem. Rev.* **2000**, *100*, 717.

General Conclusion

In this thesis, the author theoretically studied nature and properties of electronic excited states of transition metal complexes. Achievements of this thesis are summarized, as follows.

In chapter 1, the author investigated metal–metal multiple bonds in transition metal complexes. Accomplishments of this investigation become fundamental knowledge of photochemical reactions of multinuclear transition metal complexes because partial formation or dissociation of the metal–metal multiple bonds often occurs in these reactions. Summary of this investigation is as below: Four dinuclear rhenium complexes, $[Re_2Cl_8]^{2-}$, $[Re_2(\mu\text{-}Cl)_3Cl_6]^{2-}$, $[Re_2(\mu\text{-}Cl)_3Cl_6]^{-}$, and $[Re_2(\mu\text{-}Cl)_2Cl_8]^{2-}$ were theoretically investigated by complete active space self-consistent-field (CASSCF), multireference Møller–Plesset second-order perturbation theory (MRMP2), state averaged (SA) CASSCF, and multiconfigurational quasi-degenerate perturbation theory (MCQDPT). Interesting differences in the electronic structure and Re–Re bonding nature among these complexes are clearly reported, as follows: In $[Re_2Cl_8]^{2-}$, which takes non-bridged geometry, the ground state possesses $^1A_{1g}$ symmetry. Electron configuration of Re–Re molecular orbitals in this ground state is evaluated as $\sigma^{1.92}\pi^{3.74}\delta^{1.52}\delta^{*0.48}\pi^{*0.26}\sigma^{*0.08}$ by the CASSCF wavefunction. This electron configuration is much different from the formal electron configuration as $\sigma^2\pi^4\delta^2\delta^{*0}\pi^{*0}\sigma^{*0}$. This difference means that the bonding interaction of the δ orbital in $[Re_2Cl_8]^{2-}$ is much weak, which was also reported by the previous theoretical study (Gagliardi, L.; Roos, B. O. *Inorg. Chem.* **2003**, *42*, 1599). Approximate stabilization energies by the σ, π, and δ bonding interactions are evaluated to be 4.36, 2.89, and 0.52 eV, respectively, by the MRMP2 method. In $[Re_2(\mu\text{-}Cl)_3Cl_6]^{2-}$, which takes face-sharing bioctahedral bridged geometry, the ground state possesses $^2E''$ symmetry. The electron configuration of the Re–Re molecular orbitals is estimated as $\sigma^{1.87}\delta^{3.47}\delta^{*1.53}\sigma^{*0.13}$ by the SA-CASSCF wavefunction, which is much different from the formal electron configuration as $\sigma^2\delta^4\delta^{*1}\sigma^{*0}$. This difference means that the bonding interactions of two δ orbitals are

also much weak like that of the δ orbital in $[Re_2Cl_8]^{2-}$. The approximate stabilization energy by two degenerated δ bonding interactions is estimated to be 0.36 eV by the MCQDPT method. In $[Re_2(\mu\text{-}Cl)_3Cl_6]^-$, which also takes face-sharing bioctahedral bridged geometry, the ground state is $^1A_1'$ state. The Re–Re electron configuration evaluated with the CASSCF wavefunctiom is $\sigma^{1.62}\delta^{2.18}\delta^{*1.82}\sigma^{*0.38}$. Populations of σ (1.62) and σ* (0.38) orbitals are respectively smaller and larger than those of σ (1.87) and σ* (0.13) orbitals in $[Re_2(\mu\text{-}Cl)_3Cl_6]^{2-}$. This means that the σ bonding interaction is much weaker in $[Re_2(\mu\text{-}Cl)_3Cl_6]^-$ than in $[Re_2(\mu\text{-}Cl)_3Cl_6]^{2-}$ though both complexes take similar face-sharing geometry. In $[Re_2(\mu\text{-}Cl)_2Cl_8]^{2-}$, which takes edge-sharing bioctahedral bridged geometry, the σ, π, and δ bonding interactions are not effectively formed between two Re centers. The electron configuration of the Re–Re orbitals is estimated as $\sigma^{1.00}\pi^{0.99}\delta^{0.97}\delta^{*1.03}\pi^{*1.01}\sigma^{*1.00}$ by the CASSCF wavefunction.

In chapter 2, the author investigated the metal–mtel multiple bonds in transition metal complexes like in chapter 1. Though the metal–metal molecular orbitals discussed in the previous chapter are formed only by atomic orabitals of transition metals, the metal–metal orbitrals in this chapter include atomic orbitals of both transition metals and typical elements. Summary of this chapter is as below: The ground state and some low-lying excited states of $[Re_2(\mu\text{-}O)_2(NH_3)_8]^{3+}$ (Re(III)–Re(IV) complex) and $[Re_2(\mu\text{-}O)_2(NH_3)_8]^{4+}$ (Re(IV)–Re(IV) complex) were theoretically investigated by the MRMP2 method and density functional theory (DFT) with B3LYP functional. These complexes are model of $[Re_2(\mu\text{-}O)_2(Metpa)_2]^{3+}$, $[Re_2(\mu\text{-}O)_2(Metpa)_2]^{4+}$, and $[Re_2(\mu\text{-}O)_2(Me_2tpa)_2]^{4+}$ {Metpa = ((6-methyl-2-pyridyl)-methyl)bis(2-pyridylmethyl)amine and Me_2tpa = bis((6-methyl-2-pyridyl)methyl)(2-pyridylmethyl)amine}. The ground states of $[Re_2(\mu\text{-}O)_2(NH_3)_8]^{4+}$ and $[Re_2(\mu\text{-}O)_2(NH_3)_8]^{3+}$ are respectively assigned to be ^{7}B and ^{6}B states by the DFT(B3LYP) method, but to be ^{1}A and ^{2}B states by the MRMP2 method. In $[Re_2(\mu\text{-}O)_2(NH_3)_8]^{4+}$, the DFT-optimized Re–Re distance of the ^{7}B state is different from the experimental values of similar complexes such as $[Re_2(\mu\text{-}O)_2(Metpa)_2]^{4+}$ and $[Re_2(\mu\text{-}O)_2(Me_2tpa)_2]^{4+}$. However, the Re–Re distance of the ^{1}A state is in good agreement with the experimental ones. Also, in $[Re_2(\mu\text{-}O)_2(NH_3)_8]^{3+}$, the DFT-optimized Re–Re distance of the ^{6}B state much differs from

the experimental value of the similar complex, $[Re_2(\mu\text{-}O)_2(Metpa)_2]^{3+}$, but that of the ^2B state agrees well with the experimental value. These results indicate that the ground state of $[Re_2(\mu\text{-}O)_2(NH_3)_8]^{4+}$ and $[Re_2(\mu\text{-}O)_2(NH_3)_8]^{3+}$ respectively are the ^1A and ^2B states, as assigned by the MRMP2 method. In the DFT(B3LYP) calculations of the ^1A state of $[Re_2(\mu\text{-}O)_2(NH_3)_8]^{4+}$, the Re–Re molecular orbitals rise in energy in order $\sigma < \delta^* < \pi < \pi^* < \delta < \sigma^*$, which is different from general order $\sigma < \pi < \delta < \delta^* < \pi^* < \sigma^*$. This interesting result is explained, as follows: The π and δ bonding orbitals of $[Re_2(\mu\text{-}O)_2(NH_3)_8]^{4+}$ include d(Re)–p(O) antibonding interaction but the δ^* antibonding counterpart does not. As a result, the π and δ orbitals become higher in energy than the δ^* orbital.

In chapter 3, the author researched phosphorescence energies of transition metal complexes which are shifted by experimental conditions such as temperature and solvent. This research focused on not only assignment of the electronic structure but also geometry change in the excited state, where discussion based on the latter factor rarely presented in the previous studies. Summary of this research is as below: Four kinds of 3,5-dialkylpyrazolate-bridged dinuclear platinum(II) complexes $[Pt_2(\mu\text{-}R_2pz)_2(dfppy)_2]$ (dfppy = 2-(2,4-difluorophenyl)pyridine and R_2pz = pyrazolate (H_2pz), 3,5-dimethylpyrazolate (Me_2pz), 3-methyl-5-*tert*-butylpyrazolate (Me^tBupz), or 3,5-bis(*tert*-butyl)pyrazolate ($^tBu_2pz$)) were theoretically investigated by the DFT method with B3PW91 functional. Phosphorescence properties of these platinum complexes were discussed on the basis of potential energy curve (PEC) of the lowest energy triplet excited state (T_1). This PEC significantly depends on bulkiness of substituents on pz. In the μ-H_2pz and μ-Me_2pz complexes, bearing small substituents on pz, one local minimum appears in the T_1 state besides the global minimum. This local minimum geometry is similar to the S_0-equilibrium one. The T_1 state at this local minimum is characterized as π–π^* excited state in dfppy, where dπ orbital of Pt participates in this excited state through antibonding interaction with π orbital of dfppy; in other words, this triplet excited state is assigned as mixture of ligand-centered π–π^* and metal-to-ligand charge transfer excited state (^{3}LC/MLCT). Geometry of the T_1-global minimum is considerably different from the S_0-equilibrium one. The T_1 state at the global minimum is characterized as

metal–metal-to-ligand charge transfer (^{3}MMLCT) excited state, which is formed by one-electron excitation from dσ–dσ antibonding orbital to π* orbital of dfppy. Because of presence of the local minimum, the geometry hardly changes in polystyrene at room temperature (RT) and frozen 2-methyltetrahydrofuran (2-MeTHF) at 77 K. As a result, the phosphorescence energy is almost the same in these conditions. In fluid 2-MeTHF at RT, on the other hand, geometry of the T_1 state easily reaches the T_1-global minimum. Because the T_1-global minimum geometry is considerably different from the S_0-equilibrium one, the phosphorescence occurs at considerably low energy. These are reasons why the Stokes shift is very large in fluid 2-MeTHF but small in polystyrene and frozen 2-MeTHF. In the μ-Me^{t}Bupz and μ-^{t}Bu$_2$pz complexes, bearing bulky *tert*-butyl substituents on pz, only T_1-global minimum is present but local minimum is not. Electronic structure of this T_1-global minimum is assigned to the ^{3}MMLCT excited state like the μ-H$_2$pz and μ-Me$_2$pz complexes. Though frozen 2-MeTHF suppresses the geometry change of the μ-Me^{t}Bupz and μ-^{t}Bu$_2$pz complexes in the T_1 state, their geometries moderately change in polystyrene because of the absence of the T_1-local minimum. As a result, the phosphorescence energy is moderately lower in polystyrene than in frozen 2-MeTHF. The T_1-global minimum geometry is much different from the S_0-equilibrium one in the μ-Me^{t}Bupz complex but moderately different in the μ-^{t}Bu$_2$pz one, which is interpreted in terms of symmetries of these complexes and steric repulsion between *tert*-butyl group on pz and dfppy. As a result, the phosphorescence energy of the μ-Me^{t}Bupz complex is much lower in fluid 2-MeTHF than in frozen 2-MeTHF like the μ-H$_2$pz and μ-Me$_2$pz complexes, while that of the μ-^{t}Bu$_2$pz complex is moderately lower.

In chapter 4, the author studied the spin–orbit interaction between S_1 and T_1 states of transition metal complex, which is one of the determinant factors whether the complex exhibits phosphorescence or not. Discussion of this study was performed based on the relationship between symmetry of electronic structure and the spin–orbit interaction like the previous study by El-Sayed. Thus, this study corresponds to one of the works to evolve the El-Sayed's rule, which predicts the rate of intersystem crossing and the intensity of phosphorescence in organic molecules. The discussion is summarized as below:

Dinuclear platinum(II) complexes $[Pt_2(\mu\text{-pz})_2(bpym)_2]^{2+}$ (pz = pyrazolate and bpym = 2,2'-bipyrimidine) and $[Pt_2(\mu\text{-pyt})_2(ppy)_2]$ (pyt = pyridine-2-thiolate and ppy = 2-phenylpyridine) were theoretically investigated with the DFT(B3PW91) method to clarify the reasons why the phosphorescence of $[Pt_2(\mu\text{-pz})_2(bpym)_2]^{2+}$ is not observed in acetonitrile (CH_3CN) solution at RT but observed in solid state at RT, and why the phosphorescence of $[Pt_2(\mu\text{-pyt})_2(ppy)_2]$ is observed in both CH_3CN solution and solid state at RT. The S_1 and T_1 states of $[Pt_2(\mu\text{-pz})_2(bpym)_2]^{2+}$ in CH_3CN solution are assigned as the MMLCT excited state. Their geometries are C_{2v} symmetry, in which the spin–orbit interaction between S_1 and T_1 states is absent. This is because direct product of irreducible representations of the singly occupied molecular orbitals (SOMOs) of these excited states and the orbital angular momentum (l) operator does not belong to a_1 representation, where the l is included in the spin–orbit Hamiltonian. As a result, $S_1 \rightarrow T_1$ intersystem crossing hardly occurs, leading to the absence of $T_1 \rightarrow S_0$ phosphorescence in CH_3CN solution at RT. In solid state, geometry of the S_1 state does not reach the global minimum but stays in C_1-symmetrical local minimum. This S_1 excited state is assigned as the LC/MLCT state. The spin–orbit interaction between S_1 and T_1 states operates to induce the $S_1 \rightarrow T_1$ intersystem crossing because the direct product of irreducible representations of the SOMOs and the l operator belongs to “a” representation. As a result, the $T_1 \rightarrow S_0$ phosphorescence occurs in solid state at RT. In $[Pt_2(\mu\text{-pyt})_2(ppy)_2]$, the S_1 and T_1 states are assigned as the MMLCT excited state. Their geometries are C_2-symmetries in both CH_3CN solution and solid state, in which the spin–orbit interaction between S_1 and T_1 states operates to induce the $S_1 \rightarrow T_1$ intersystem crossing. This is because direct product of irreducible representations of the SOMOs and the l operator belongs to “a” representation. Thus, the $T_1 \rightarrow S_0$ phosphorescence occurs in both CH_3CN solution and solid state, unlike $[Pt_2(\mu\text{-pz})_2(bpym)_2]^{2+}$.

In chapter 5, the author proposed a new method to calculate oscillator strength of the Laporte-forbidden d–d absorption. This new method incorporates effects of distortions of molecular orbitals induced by molecular vibrations. The study by this method is summarized as below: The oscillator strengths of $[Co(NH_3)_6]^{3+}$ and $[Rh(NH_3)_6]^{3+}$ were

theoretically evaluated. Calculated oscillator strengths of $[Co(NH_3)_6]^{3+}$ agree well with the experimental values in both $^1A_{1g} \rightarrow {}^1T_{1g}$ and $^1A_{1g} \rightarrow {}^1T_{2g}$ absorptions. In $[Rh(NH_3)_6]^{3+}$, although the calculated oscillator strengths are somewhat smaller than the experimental values, computational results reproduce well the experimental trends; one trend is that the oscillator strengths of $[Rh(NH_3)_6]^{3+}$ are much larger than those of $[Co(NH_3)_6]^{3+}$ and another trend is that the oscillator strength is larger in the $^1A_{1g} \rightarrow {}^1T_{1g}$ absorption than in the $^1A_{1g} \rightarrow {}^1T_{2g}$ one. The difference of the oscillator strengths between two complexes are explained, as below: Mixture of the sp^3 orbitals of NH_3 ligands to the d orbitals of metal center is larger in $[Rh(NH_3)_6]^{3+}$ than in $[Co(NH_3)_6]^{3+}$. Thus, the distortions of the d orbitals are larger in the former complex than in the latter one, which induces the stronger oscillator strength in the former complex. The calculation clearly shows that the oscillator strength is not negligibly small even at 0 K. This means that the d–d absorptions of $[Co(NH_3)_6]^{3+}$ and $[Rh(NH_3)_6]^{3+}$ are strongly induced not only by the excited molecular vibrations but also by the zero-point molecular vibration.

As described above, the author presented explanation and understanding of nature and properties of electronic excited transition metal complexes, overcoming theoretical difficulties of the electronic structure calculations. Because these achievements were based on fundamental properties of the chemistry such as the molecular geometry and the electronic structure, the author believes that this thesis will certainly evolve the chemistry of excited transition metal complexes.

List of Publications

Chapter 1

Theoretical Study of Rhenium Dinuclear Complexes: Re–Re Bonding Nature and Electronic Structure

Ken Saito, Yoshihide Nakao, Hirofumi Sato, Shigeyoshi Sakaki

J. Phys. Chem. A **2006**, *110*, 9710–9717.

Chapter 2

Theoretical Investigation of μ-O-Bridged Dinuclear Re Complexes: Electronic Structure, Bonding Nature, and Absorption Spectra

Yoshihide Nakao, Ken Saito, Shigeyoshi Sakaki

Int. J. Quantum Chem. **2009**, *109*, 2319–2327.

Chapter 3

Theoretical Study of Pyrazolate-Bridged Dinuclear Platinum(II) Complexes: Interesting Potential Energy Curve of the Lowest Energy Triplet Excited State and Phosphorescence Spectra

Ken Saito, Yoshihide Nakao, Shigeyoshi Sakaki

Inorg. Chem. **2008**, *47*, 4329–4337.

Chapter 4

Theoretical Study of Excited States of Pyrazolate- and Pyridinethiolate-Bridged Dinuclear Platinum(II) Complexes: Relationship between Geometries of Excited States and Phosphorescence Spectra

Ken Saito, Yoshihide Nakao, Keisuke Umakoshi, Shigeyoshi Sakaki

Inorg. Chem. **2010**, *49*, 8977–8985.

Chapter 5

Oscillator Strength of Symmetry-Forbidden d–d Absorption of Octahedral Transition Metal Complex: Theoretical Evaluation

Ken Saito, Yoshinori Eishiro, Yoshihide Nakao, Hirofumi Sato, Shigeyoshi Sakaki

Inorg. Chem. **2012**, *51*, 2785–2792.